Title

Advanced Methodology for Drug Delivery

Author

Owen, Matthew James

Publication Date

2021

Advanced Methodology for Drug Delivery

By

Matthew James Owen

DISSERTATION

Submitted in partial satisfaction of the requirements for the degree of

DOCTOR OF PHILOSOPHY

in

Chemistry

in the

OFFICE OF GRADUATE STUDIES

of the

UNIVERSITY OF CALIFORNIA

DAVIS

Approved

Prof. Gang-yu Liu, Chair

Prof. Dominik R. Haudenschild

Prof. Atul N. Parikh

Committee in Charge

2021

Acknowledgement

In my academic journey, the road has been both difficult and rewarding. My academic journey began at Sacramento City College, where I would like to acknowledge Professor William (Bill) Miller for the guidance in learning and applying chemistry in research. At University of California, Berkeley, I would like to acknowledge Prof. T. Don Tilley and Dr. Andy I. Nguyen in introducing me to the world of Inorganic Chemistry and developing a synthetic chemistry toolbox. At University of California, Davis, I would like to acknowledge my Principal Investigator, Prof. Gang-yu Liu. I want to thank you for your guidance, support, and encouragement throughout my academic career. You have been fundamental to my success as an independent scientist, which includes experimentation as well as scientific writing. You have just been an overall have been a positive influence on me both in and out of the lab, and you are family.

In the Liu lab, I am grateful for both current and past group members who helped me transition into an independent scientist throughout my time in graduate school. I would like to personally thank my mentor, Dr. Yang Liu for his wisdom, guidance, and scientific insight in my work. I would like to acknowledge, Dr. Weifeng Lin, Dr. Shailise S. Ross, Dr. Arpad Karsai, Dr. Marshall van Zijll, Dr. Qingbo Yang, Dr. Joao Francisco Ventrici de Souza, Dr. Shuo Wang, Dr. Jiali Zhang, Dr. Logan A. Swartz, Dr. Victoria Tran, Dr. Audrey Sulkanen, Dr. Cody Chalker, Dr. Umit Celik, Bradley Harris, Evgeny Ogorodnik, Michael Corpus Tamsi, William Deng, Brianca Netto, Yunbo Zheng, Minyuan Wang, Terell Keel, Yuqi Hwang, Sara Ismet, Andres Morales Maldonado, Noah Haughn, Subash Chaudhary, Brianca Netto, and finally Susan Stagner.

I would like to thank my collaborators from UC Davis-Medical Center, Dr. Jasper H.N. Yik and Professor Dominik R. Haudenschild and many thanks to Dr. Congwang Ye and Dr. Ted A. Lawrence at Lawrence Livermore National Laboratory. I would like to thank my collaborators

in industry, Dr. John Patton, Dr. Mei-chang Kuo, and Dr. Christopher Rhodes.

Many thanks to my dissertation committee: Prof. Dominik R. Haudenschild and Prof. Atul Parikh.

I am indebted to my parents, Dawn and Mark Liang, and my grandparents as well as the rest of my supportive family.

Finally, a huge thanks to my wife, Alexis and our beautiful children, Isabella, Leo and very soon Gabe. Without your love, support, and patience none of this work would have been feasible.

Matthew J. Owen

December 2021

This dissertation is dedicated to my late grandfather, Austin Leo John, who passed on February 5th, 2019.

ABSTRACT

The focus of this dissertation research is on the advanced methodology for drug delivery, which includes the synthesis and characterization of drug loaded delivery vehicles. Drug delivery is a rapidly advancing field, ranging from local injections for vaccine delivery to treatment of asthma via pulmonary delivery. There are many illnesses that are left untreated, because of the lack of means to deliver drugs effectively and safely, such as local sustained release to treat post-traumatic osteoarthritis (PTOA) or pulmonary delivery of anti-inflammatory therapeutics for treatment of coronavirus disease 2019 (COVID-19). In this dissertation, I will fill this void, including formulation, characterization, toxicity, and all the way to efficacy.

There are three main components in this dissertation investigation. The first, is the development of a greener approach to producing polymer microparticles for local sustained release of flavopiridol. PLGA microparticles represent an important class of materials used for drug delivery. Current synthesis frequently uses conventional emulsion, where dichloromethane(DCM) is used as the organic phase solvent. Due to the health and environmental toxicity of DCM and its slow degradation, this work replaces DCM with a greener solvent, dimethyl carbonate(DMC). To attain narrow distribution of PLGA particle size, microfluidic flow focusing was chosen over conventional emulsion. This new approach successfully produced PLGA microparticles encapsulated with flavopiridol, a kinase inhibitor. These particles exhibit sustained release profile more desirable than the conventional counterparts. The cytotoxicity and activity tests have demonstrated high biocompatibility and efficacy of these PLGA particles. The high sustainability is also evaluated using simple *E*-Factor(sEF) and complete *E*-Factor(cEF). The lower health and environmental toxicities of DMC than DCM are evidenced by approximately one order of magnitude higher in lethal dose, i.e., 50%(LD50) values in rat, 5-fold faster degradation rate, and

30% higher GlaxoSmithKline(GSK) combined greenness value. The approach reported in this work shall provide a new and green means for drug delivery in general. The products enable local sustained delivery of flavopiridol for prevention of post-traumatic osteoarthritis, and anti-cancer therapy.

The second development is focused on a new approach to quantify drug release kinetics from PLGA microparticles. Current approaches for quantifying drug release profiles from PLGA vehicles involve non-linear fitting using burst, degradation, and diffusion terms. The non-linear fitting is typically performed across the entire time spectrum, assuming that the contribution from each term is constant across the entire release profile. It is known for instance that burst release only occurs during the initial time of release, therefore prior assumption gives poor representation of physical meaning. To improve upon the current approach, a new model was developed by piecewise splitting the fitting terms over two-time regions during release of flavopiridol from PLGA microparticles. The time regions were identified via time dependent SEM imaging, through the analysis of particle morphological evolution during release. The application of our approach to these particles greatly improved and matched the current understanding of release mechanisms. Our approach was validated in larger particles, where new insight was revealed in the evolution of the fitting parameters across time regions. Particles were fabricated with a porous intra-particulate structure, as verified by AFM imaging, to test the genericness of our approach. The intra-particulate structure of these particles was revealed to cause the geometrical changes during release. Our approach further revealed the impact of particle shape change during release in contrast to particle fragmentation, especially through degradation and diffusion mechanisms. This new approach reported in this work, can be applied to drug release from polymer vehicles in general, which allows tunability of release profile to a higher degree.

The third development is focused on the production of flavopiridol loaded inhalable ultra-small particles for pulmonary delivery. Treatment of inflammation causing diseases, like COVID-19, generally used an intravenous delivery, however it has been shown that the best course of delivery to the lungs is via inhalation. Production of inhalable particles containing therapeutics are well suited for treatment of lung inflammation and has been demonstrated as the best delivery pathway for pulmonary based diseases. In this work, we showed the development of inhalable particles containing flavopiridol, a CDK-9 inhibitor with demonstrated anti-inflammatory properties, for the first time reported. Formulations of DPPC, L-isoleucine, and flavopiridol were generated into ultra-small particles that presented a desired geometry and size, well suited for pulmonary delivery. The drug loading of the particles was investigated by utilizing UV-Visible spectroscopy, showing 99% efficiency in loading. The presence of DPPC and L-isoleucine were verified by comparing against known standards in ATR-FTIR spectroscopy. The produced particles were demonstrated to be dispersible using a newly developed sampling method for high resolution SEM imaging. The in vitro release of the particles matched the required release kinetics for pulmonary delivery Flavopiridol was found to be biologically active in the produced particles. This work enables the flavopiridol to be delivered to the lungs for treatment of inflammation caused by diseases like pulmonary fibrosis or COVID-19.

This dissertation demonstrates the methodology for drug delivery, through the production and characterization of flavopiridol loaded delivery vehicles for treatment of inflammation in the knee joint capsule via local sustained release or in the lungs via pulmonary delivery, which drives momentum even further into filling the void.

TABLE OF CONTENTS

CHAPTER IV 44

New Insight into Drug Release Profiles of Flavopiridol Loaded Poly(lactic-co-glycolic acid) Microparticles 44

LIST OF FIGURES

was compared to that of the released FLAP (FLAP-PLGA) and blank PLGA (PLGA). Experiments were performed in triplicate measurements on one batch of particles (N=3) and results were reported as mean +/- SD.

Figure 4.1. Drug release profile of PLGA-1 (blue dots). At each time point of measurement, the result was expressed as mean ± SD from *n* = 3 independent sets of microparticles. Nonlinear least-squares fitting of the release profile using eq. (1) was shown as a solid black line.

Figure 4.2. SEM image of PLGA-1 microparticles, taken at designated time (atop of the images) during in vitro release measurements. Scale bar = 20 µm.

Figure 4.3. Drug release profile of PLGA-1 (blue dots). In each time point of measurement, the result is expressed as mean ± SD from *n* = 3 independent batches of PLGA microparticles. Nonlinear least-square fitting of the release profile using eq. (6) is shown as the solid black line for 0-8 days and dashed black line for 8-30 days.

Figure 4.4. SEM imaging of the PLGA-2 particles, taken at designated time points (see on top of the images) during in vitro release measurements. Scale bar = 20 μm, for all images.

Figure 4.5. Drug release profile of PLGA-2 (blue dots). In each time point of measurement, the result is expressed as mean ± SD from *n* = 3 independent batches of PLGA microparticles. Nonlinear least-square fitting of the release profile using eq. (6) is shown as the solid black line for 0-6 days and dashed black line for 6-30 days.

Figure 4.6. SEM imaging of PLGA-3 and PLGA-4particles taken at designated time points (see atop of images) during in vitro release measurements. Scale bar = 20 μm, for all images.

Figure 4.7. Topographic AFM imaging of the cross-sectioned PLGA-2 (A) and PLGA-4 (B) microparticles. For all images, scale bar = 10 µm.

Figure 4.8. Drug release profile of PLGA-3 (blue dots, A) and PLGA-4 (blue dots, B). In each

37°C. The UV-Vis spectrum of the ILDF particles in 70% Ethanol (solid black line) after 4 weeks under the three storage conditions are plotted with the freshly produced ILDF particles in 70% Ethanol (dashed black line). The absorption at λ = 230 nm for each spectrum was normalized throughout all profile.

Figure 5.8. Bioactivity of Flavopiridol in ILDF particles measured by luciferase assay. Released flavopiridol (FLAP) from ILDF particles and blank ILD particles were assessed of their bioactivity through suppression of luciferase activity in HEK-Luc reporter cells stimulated with TNF-α (0.6 nM). Experiments were performed in triplicate(N=3) from one batch of particles, and results were reported as mean±SD.

Figure 7.1. PDMS based Flow-Focusing Microfluidic Device with flow path schematic

Figure 7.2. Home-built Flow Focusing Microfluidic Device for Uniform PLGA droplet formation

Figure 7.3. Inlet and outlet locations on PDMS-based Flow Focusing Microfluidic Device

Figure 7.4. 76 μm PLGA droplet formation in Flow Focusing Microfluidic device, imaged in situ using high speed camera

Figure 7.5. Mounting Sample Vial on the Buchi R300 for removal of dichloromethane from PLGA droplets

Figure 7.6. 15.1 μm PLGA microparticles synthesized using flow focusing microfluidics

Figure 7.7. 3D visualization of AutoCAD created microfluidic flow focusing device used in Chapter III

Figure 7.8. 2D schematic of the orifice region of the microfluidic flow focusing device

LIST OF TABLES

CHAPTER I

Introduction

1.1 Advanced methodology for drug delivery

The delivery of therapeutics is a central facet of the treatment of illness, where key features, such as the region of delivery[1-3], dose[4-5], activity[6-7], toxicity[8-9], stability[10-11], longevity of treatment[12-13] are all contingent on its successful design and testing. Many drug delivery routes has been established, which includes transdermal[14], oral[15], ocular[16], nasal[17], parenteral[18], and pulmonary[19], leading to many successful therapies. Although, the drug delivery field is quite established, there are still many illnesses that are unable to be treated, due to limitations in the production and understanding of adequate and targeted delivery vehicles. This includes local sustained delivery for treatment of inflammation caused by post-traumatic osteoarthritis[20-21] (PTOA) or pulmonary delivery for treatment of lung inflammation caused by diseases like COVID-19.[22-25] In order to address these limitations in targeted treatments of these illnesses, advanced synthetic and characterization methodologies were developed to meet the production and delivery specifications.

1.2 Voids to be addressed by thesis research

1.2.1 Conventional production of drug loaded PLGA microparticles uses a known carcinogen

Local delivery of drugs[26], have been utilized with a wide variety of sustained release materials such as hydrogels[27], silk[28], poly(lactic acid)[29], poly(lactic-co-glycolic acid) (PLGA)[30-31] , and even tri-block polymers, like PLGA-PEG-PLGA.[32] For clinical applications, PLGA has been widely used by researchers as the sustained delivery vehicle, due to its biocompatibility, biodegradation, and FDA approval.[30, 33-34] PLGA is a biodegradable polymer, as shown in figure 1, where in the presence of water, a hydrolysis reaction occurs at the labile esters bonds, producing soluble byproducts present in the body, lactic and glycolic acid.

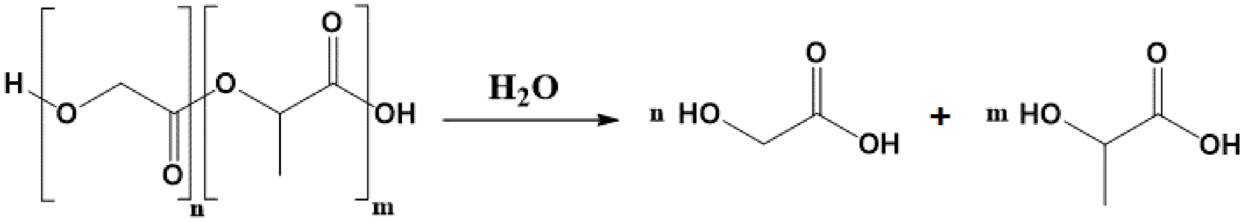

Figure 1.1 Hydrolysis of PLGA

The co-monomer ratio (n,m) is tunable based on desired longevity of sustained release. It has been demonstrated that the higher lactide contribution as compared to glycolide, produces a longer time period of sustained release. For example, when PLGA(85:15) is used in place of PLGA(50:50), 6 months of release of therapeutics is revealed as compared to 1 month.[30] Microparticles of poly(lactic-co-glycolic acid) (PLGA) have shown great promise in local sustained delivery of medicine as well as improving osteoinductivity and bone healing, owning to their biodegradable property and high biocompatibility.[30, 35-39] These particles were typically produced via conventional emulsion, which frequently utilized toxic organic solvents, such as dichloromethane (DCM).[40-41] Conventional emulsion has advantages of simplicity, but frequently exhibits limitations such as batch-to-batch irreproducibility in drug release kinetics, primarily attributed to large variation in particle size and intra-particulate structure.[42] Microfluidic flow-focusing device (MFFD) was introduced to address these limitations and are capable of producing monodispersed particles such as quantum dots, photonic particles, textiles, and polymer microparticles.[34, 42-47] MFFD typically produce particles with near monodispersion, and high reproducibility in size, load, and drug release profiles. The process also had less waste due to lower working volume.[48] Despite these new advances, DCM has remained as the organic phase solvent in most MFFD syntheses.[42, 49-50] DCM is a volatile organic compound (VOC) and a known carcinogen,[51] referred to as a Class

2 solvent as per International Council for Harmonization (ICH), whose residual amounts in medicinal products is limited to no more than 600 ppm.[51-52] DCM was recently banned for consumer use, to protect health and environment regulated by the United States government and environmental protection agency (EPA).[53] Green chemistry principles are strongly encouraged in chemical synthesis[54], thus it is essential to seek an alternative and green solvent to replace DCM in production of drug delivery polymer particles. Therefore, in this work, we utilized dimethyl carbonate (DMC) to encapsulate flavopiridol in PLGA microparticles for the first time reported using a green solvent. It is shown that using the greener method, the in vitro release kinetics, degradation profile, biological activity and cytotoxicity, points towards a successful drug product for treatment of post traumatic osteoarthritis (PTOA).

1.2.2 Current quantification of drug release from PLGA microparticles

The quantification of drug release profiles is of importance for not only understanding the mechanisms of drug release, but it reveals considerations in the tunability of its kinetics.[55] For biodegradable particles like PLGA microparticles, various quantification models are used to describe drug release, such as zero order, first order, Higuchi, Hixson-Crowell, and Ritger-Peppas-Korsmeyer.[55-57] However, these models generally describe one to two mechanisms of drug release, and are applied throughout the release duration. Drug release from PLGA microparticles is widely seen as a tri-phasic mechanism, involving an initial burst, degradation-relaxation of PLGA, and Fickian diffusion processes.[30, 58-59] It has been demonstrated that addition of 2-3 mechanisms, better describes the drug release process and fits the experimental data mathematically good.[60-61] Conventionally, these models are fitted throughout the release process, generating constant fitting parameters, which doesn’t align with processes that are known to occur in certain regions of the release profile, for instance, burst release is short time mechanism that occurs generally up to 5 days release.[42, 62] In this work, the quantification of the drug release profile, involved the identification of time regions where each term is known to be present, using high-resolution time dependent scanning electron microscopy. From the identified regions, a new approach using existing models were generated which agree with known understanding drug release profiles.

1.2.3 Production of flavopiridol loaded inhalable ultra-small particles for pulmonary delivery

Flavopiridol is a well-known small molecule cyclin dependent kinase inhibitor (CDK) originally designated by the Food and Drug Administration (FDA) as an orphan drug for treatment of rare leukemia.[63]. The activity of flavopiridol has been known to prevent activation of primary response genes, thus inhibiting down-stream inflammation of cells and tissues. [40, 64-68] Therefore, Flavopiridol has been used to treat inflammation caused by illnesses ranging from cancer[63, 69-70], viral[71-73] and post-traumatic-osteoarthritis (PTOA)[40, 65-66], Given its high efficacy, Flavopiridol has been identified as a very promising candidate to treat illness such as lung cancer[74] or coronavirus disease 2019 (COVID-19) pertaining to lung inflammation.[75-76] In past attempts to treat lung injury, the delivery means included intraperitoneal (i.p.) injection into the lower quadrant of the abdomen or via gavage, which involved forcible oral delivery.[77] To improve efficacy and patient-friendliness, pulmonary delivery of inhalable particles using a device such as a dry powder inhaler (DPI) is becoming an urgent need, as inhalation delivery has intrinsic advantage of being non-invasive and rapid. [78-80] While inhalable delivery of drugs has been reported[81-83], none of the current vehicles have been used to carry flavopiridol. Therefore, this work reports our effort in the production and characterization of flavopiridol-loaded inhalable ultra-small particles for pulmonary delivery.

1.3 Thesis objective

The overall goal of this dissertation is demonstrated by the advanced synthesis and characterization of flavopiridol loaded drug delivery vehicles. This is goal was divided into three specific aims. The first specific aim is to develop a greener methodology for the production of flavopiridol loaded PLGA microparticles for local sustained release applications. The second aim is to develop a new approach in the quantification of drug release profile of flavopiridol loaded PLGA microparticles. The third aim is the development and characterization of flavopiridol loaded inhalable particles for treatment of inflammation in the lungs.

1.5 Thesis organization

Following the introductory chapter, chapter II describes the synthetic methods involving PLGA and inhalable particles, and the characterization methods include, microfluidic device cleaning, dispersity of inhalable particles, UV-Vis spectroscopy, ATR-FTIR, SEM, and AFM. Chapter III describes a greener methodology for the production of flavopiridol loaded PLGA microparticles for local sustained release. Chapter IV describes new insight into drug release profiles of flavopiridol loaded PLGA microparticles. Chapter V describes the production of flavopiridol loaded ultra-small inhalable particles for pulmonary delivery. Chapter VI discusses conclusions and future work. Finally, Chapter VII describes the appendix, containing an SOP and MATLAB codes for nonlinear fitting.

CHAPTER II

Experimental Approaches

2.1 Home-built Flow-Focusing Microfluidic Device for PLGA Microparticle Synthesis

Microfluidics is the study or manipulation of fluids on the micrometer scale, with height and width of channels between 100 nm to 100 μm.[84] For the past 20 years, microfluidics has been adapted into many applications ranging from cellular sorting to particle synthesis.[85-87] Microfluidic synthesis of polymers, like PLGA microparticles has been widely demonstrated throughout literature with the encapsulation of small molecule drugs, proteins, and peptides.[38, 49, 88-89] The synthesis of PLGA particles is usually performed using flow-focusing microfluidics with poly(dimethylsulfoxide) (PDMS) based devices.[34, 42]. In this work, I designed a flow focusing microfluidic device based on device geometries known to generate monodisperse PLGA particles. The blueprint of the design was generated in AutoCAD and an .STL file was exported. The .STL file was sent to a microfluidic manufacturer (uFluidix, Scarborough, Ontario, Canada), where the .STL file was generated into a photolithography mask and subject to poly(dimethyl siloxane) (PDMS) based soft lithography[90]. PDMS was chosen due to the price of manufacturing and being optically transparent for microscopic visualization. Before synthesis, the microchannels of the device are subject to hydrophilic treatment to prevent organic wetting of the channel side walls.[91] The hydrophilic treatment consists of filling all channels with 1%(w/v) poly(vinyl alcohol) (PVA) (9-10 kDa, 80% hydrolyzed) for 15 min, followed by removal of PVA by blowing purified N_2 gas, and placing device in oven at 110 ℃ for 10 min to remove residual PVA. This process is repeated 2X to ensure maximum hydrophilic coating on PDMS.

The overall device is shown in figure 2.1, where the central MFFD is placed on an inverted microscope (Olympus, USA). A high-speed camera (Photron Ax100, Photron Inc., San Diego, CA) is attached to the optical microscope to allow in situ visualization of droplet formation which guided the optimization of our experimental parameters to achieve droplet flow. The camera has high sensitivity and frame rates up to 500,000/s.

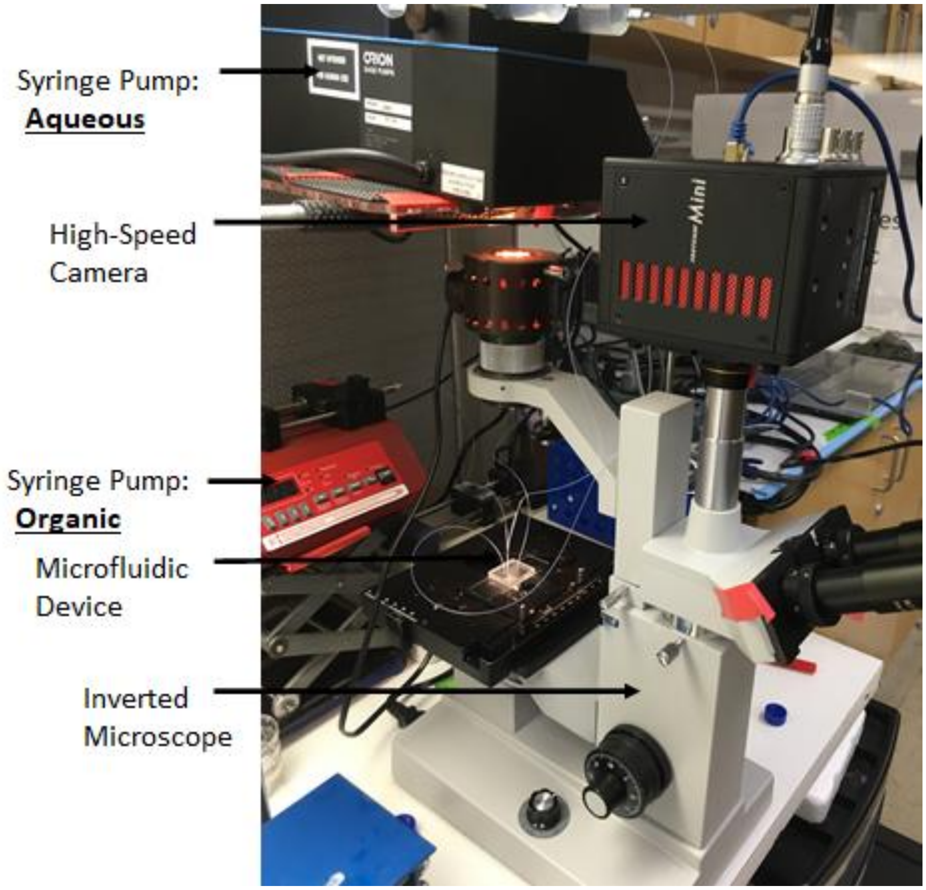

Figure 2.1. Home-built Flow Focusing Microfluidic Device

Aqueous inlets are separately connected via poly(tetrafluoroethylene) (PTFE) tubing (ID 0.7 mm) to a 20 mL gas-tight syringe (Hamilton) containing 1%(w/v) PVA equipped on a dual syringe pump (Sage Instruments Model 355 Syringe Pump, Orion Research, USA). The organic inlet is connected via PTFE tubing (ID 0.7 mm) to a 1 mL gas-tight syringe (Hamilton) containing organic solution equipped on a single syringe pump (NE-1002X Programmable Microfluidics Syringe

Pump, New Era Pump Systems Inc., NY, USA). The organic solution was prepared by dissolving 10-50 mg PLGA (50:50) (Corbion Purac, 5004A, 0.4 IV) in 1 mL dichloromethane (DCM) solution containing desired loading mass of Flavopiridol from stock solution (2 mg/mL in dichloromethane) (Freebase, Cayman). The outlet is connected via PTFE tubing and immersed in a 50 mL round-bottom flask containing 5 mL of 1% PVA which is on the right side of figure 2.2. The fluid flow path is seen in figure 2.2A, where the height and width of the channels is 120 and 300 μm and the flow focusing junction is 100 μm. The droplet generation occurs at the flow focusing junction, where the organic phase is sheared by the faster moving aqueous phase into monodisperse droplets, this process is visualized in the optical image seen in figure 2.2B.

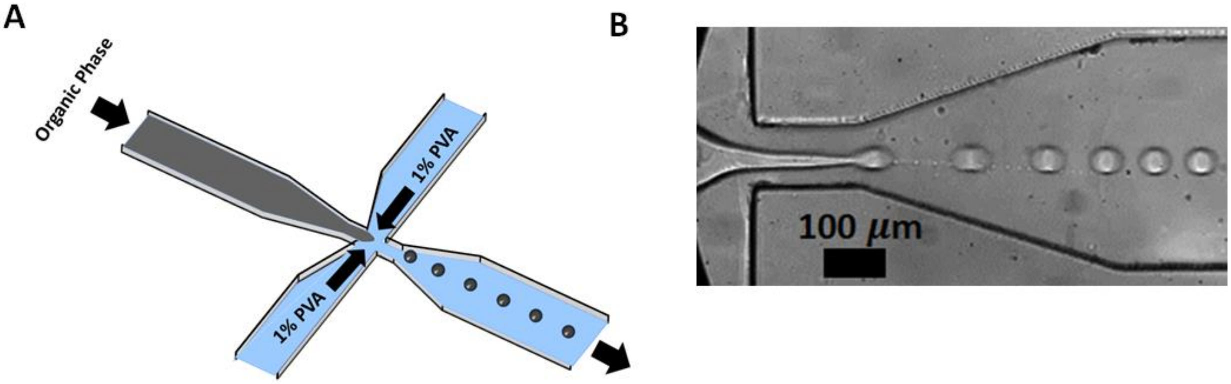

Figure 2.2. PLGA microparticle synthesis using flow focusing microfluidic device. A. Schematic representation describing fluid flow path in organic droplet formation process. B. Optical image obtained during microfluidic synthesis of PLGA droplets via high-speed camera.

2.2 Cleaning of PDMS-based Microfluidic Device.

The PDMS based microfluidic devices explained in the previous sections were subject to cleaning protocols to improve the sustainability and lifetime of the devices. Following PLGA microparticle synthesis, the microfluidic device is quite dirty and full of synthesis byproducts as seen in figure 2.3A and 2.3B. To clean the device channels, a stepwise procedure was developed. First, the microfluidic device was placed in 50 mL conical centrifuge tube (Corning^{TM}, Fisher Scientific, Hampton, NH), and 40 mL of 0.1 (w/v) Sodium dodecyl sulfate (SDS) in ultrapure water (EMD Millipore, Billerica, MA) was added to the tube. The tube was then placed in a bath sonicator (Cole-Parmer, Vernon Hills, IL) and sonicated for 15 min. Following sonication, the same steps above were applied using acetone. Following acetone treatment, 200 proof ethanol and then ultrapure water was used. Finally, this whole process is repeated 2X to ensure adequate cleaning. Following complete treatment, the microfluidic channels were blow dry with nitrogen gas. The optical images of the cleaned device are seen in figure 2.3C and 2.3D, showing channels free of debris and ready to use.

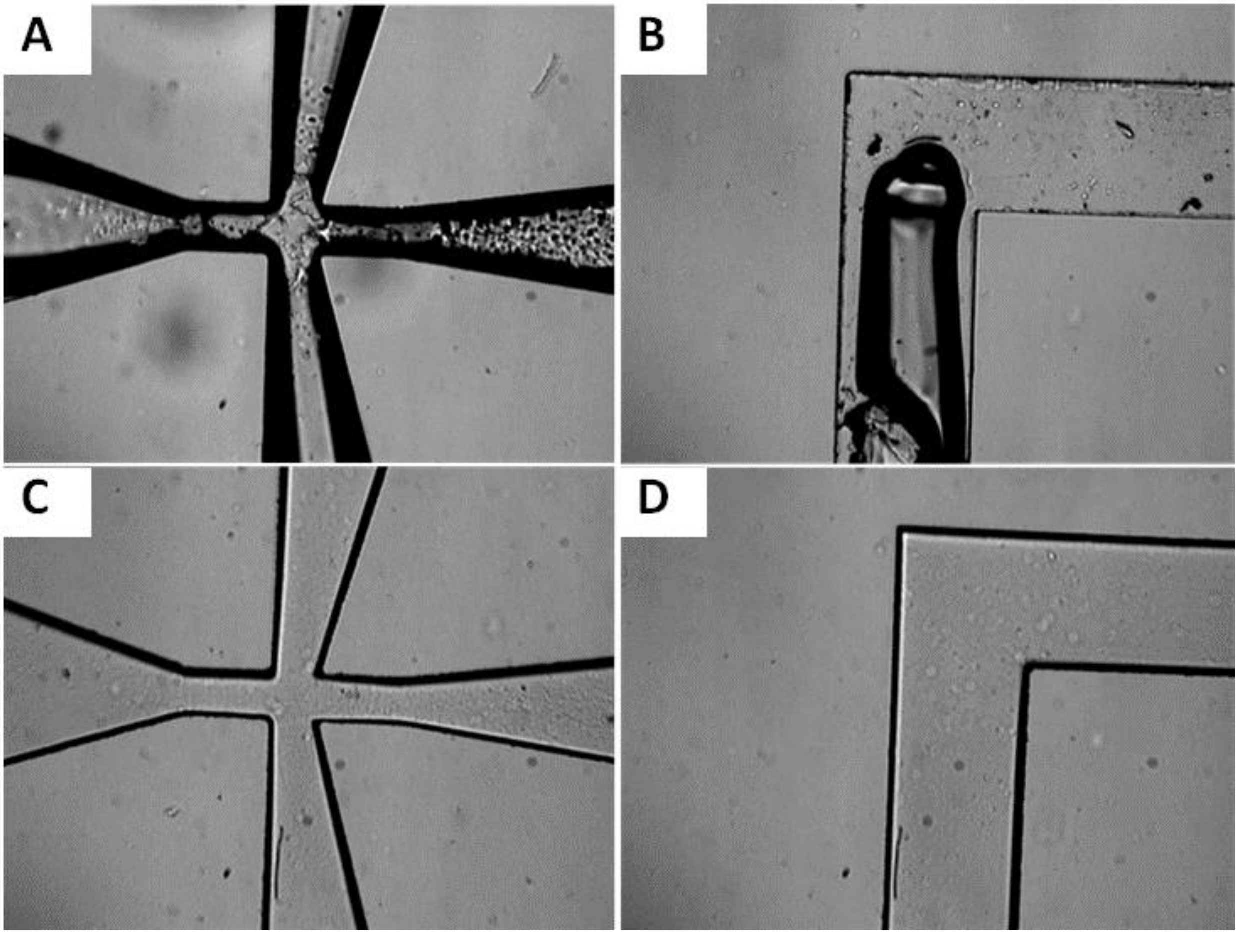

Figure 2.3. Cleaning of PDMS-based microfluidic devices. A flow focusing junction following PLGA microparticle synthesis. B. Aqueous phase channel corner following PLGA microparticle synthesis, C. Flow focusing junction after cleaning. D. Aqueous phase channel corner after cleaning.

2.3 Microfluidic Piezo and Cyclone Apparatus for Inhalable Particle Synthesis

Inhalable particles for pulmonary delivery can be produced in a variety of methodologies, the most common being spray drying[81, 83, 92-96]. Spray drying utilizes a hot gas, usually air to dry a spray of micronized droplets produced by fluid pushed through a nozzle.[97] This technique is ideal, due to production of dried particles without further drying treatment.[98] Recently, it has been shown to produce monodispersed particles using spray drying coupled with a multi-orifice piezo device.[99] In this work, we produced our own home-built spray dryer that incorporates a commercial humidifier to produce micronized droplets, with a custom built cyclone separator to collect dry particles from nitrogen gas carrier/drying gas. A microfluidic piezo and cyclone apparatus was developed to generate inhalable particles as seen in figure 2.4A. A solution composed of solvent, drug, and excipients is pumped via syringe pump and dropped onto the microfluidic piezo array. The microfluidic piezo array is a commercial humidifier (Steminc, Davenport, FL) , composed a stainless-steel disk with an array of 4- 11 μm holes, ceramic piezo rings are fixed on the top and bottom of the array. The microfluidic piezo is connected to a piezo driver, which is set at the resonant frequency of the piezo, 113 kHz. By applying 30 V to piezo driver, the device vibrates at 113 kHz. The feed solution is dropped on to the vibrating device at 5-30 mL/hr., and gravitational force causes the large droplet to be pulled into the array, leading to the formation of a spray of micronized droplets. At the top of the acrylic box, which houses the entire apparatus, a nitrogen inlet feeds into the enclosure at 20 L/min. As seen in figure 2.4B, the nitrogen gas carries and begins to dry the micronized droplets into the custom PTFE funnel and carried into the cyclone chamber. In the cyclone chamber, the particles strike the side walls causing a decrease in velocity, effectively landing in the glass collection vial, while the gas and evaporated solvent travel to the vacuum outlet and are removed via vacuum pump. This entire apparatus can be seen as a “poor man’s spray dryer” as it costs ~ $3500, as compared to commercial lab-scale spray drying ~ $120,000.

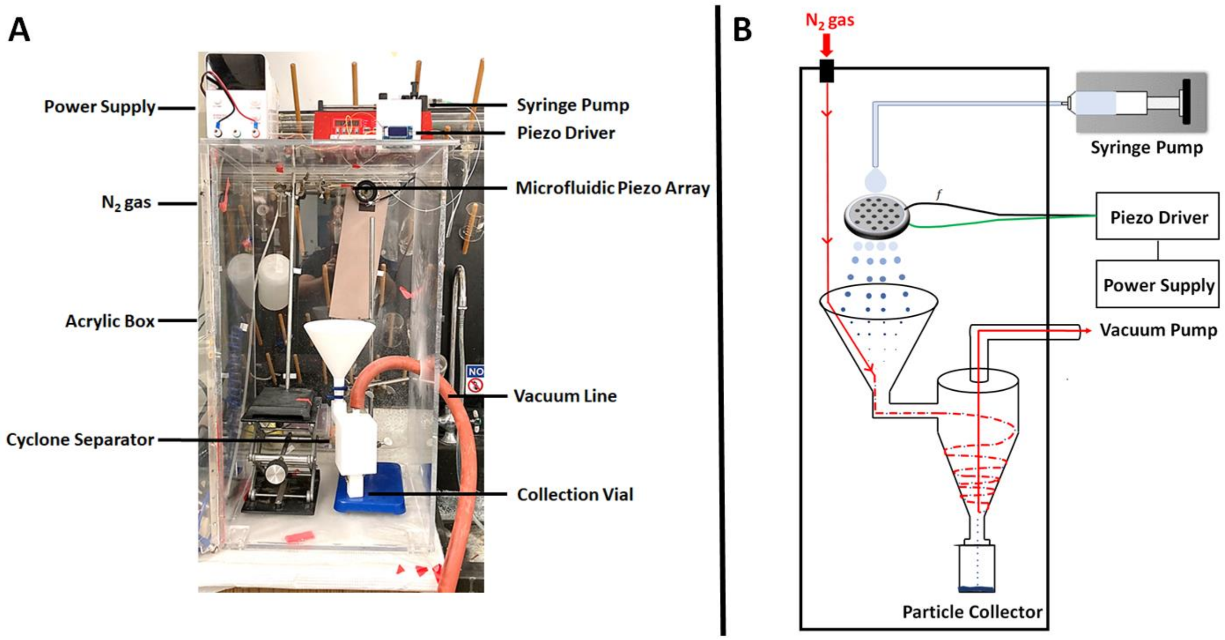

Figure 2.4. Microfluidic Piezo Array with Cyclone (MPAC) ambient temperature synthesis of inhalable particles. The instrumental set up is shown in (A), and the instrumental process schematic is shown in (B).

2.4 UV-Vis spectroscopy

Molecular spectroscopy is one of the oldest techniques to characterize molecules, and the basis for quantitative treatment started with the formulation of the Beers-lambert law in 1852.[100] Originally, the detection of a colored solution following reaction by eye was used to qualitatively characterize the sample and fast tracking to 2021, drastic advances has been made in molecular spectroscopy, especially Ultra-violet visible spectroscopy (UV-Vis).[101-104] UV-Vis spectroscopy is an analytical method that measures the absorption of light by a compound between the UV region (190-380 nm) and the visible region (380 – 750 nm). The incident light is absorbed by a compound up to certain energy levels is an inherent property that is related to transitions between quantized energy levels. These transitions can be characterized using a variety of detectors, from a monochromator to photo diode array.[105] Array based detectors are especially useful, because the full UV-Visible spectrum is the readout, allowing simultaneous analysis of the spectrum. The generic workflow of UV-Visible spectroscopy is shown below using a photodiode array detector in figure 2.5.

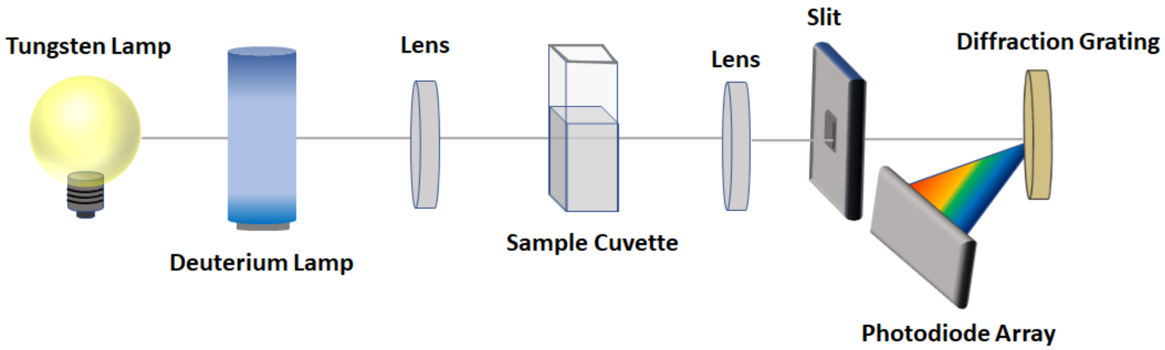

Figure **2.5.** Schematic representation of the light path of UV-Vis spectroscopy

Projected light from a tungsten lamp (370 – 1100 nm) and deuterium lamp (190 – 800 nm) is directed toward a lens that focuses it through a quartz cuvette containing a solution with a compound of interest. The transmitted light is passed through another lens which focuses it through a slit, where it is strikes a diffraction grating which separates into the wavelength range and diffracted towards a photodiode array. The photodiode array converts the photonic signal into absorbance units corresponding to the wavelength range (190-1100 nm).

2.5 Attenuated Transmittance Reflectance – Fourier Transform Infrared Spectroscopy

Fourier transform infrared spectroscopy (FTIR) is a spectroscopic method that quantifies infrared light (4000 – 400 cm^{-1}) absorbed by a compound. [106] This light absorbed by the compound causes vibrational modes to be activated at certain wavelengths for various functional groups, i.e. C=O stretching ~ 1700 cm^{-1}.[107] The identification of these vibrational modes is used for detection and in some cases quantification of compounds present. FTIR spectrometers commonly consists of major components such as an IR source, interferometer, sample cell, detector, and finally a computer.[106] The components of the FTIR instrument are seen in the block diagram below in figure 2.6.

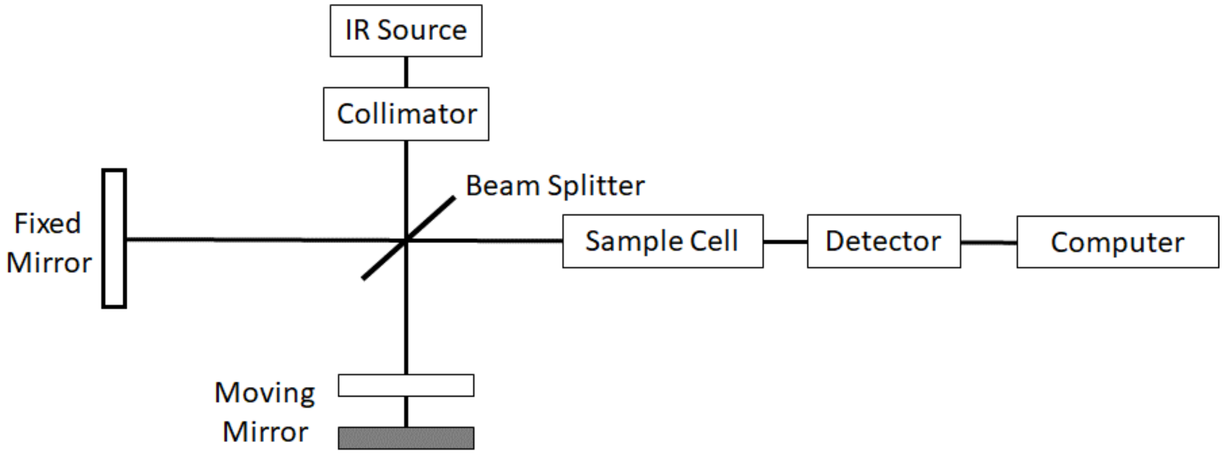

Figure 2.6. Block diagram of FTIR

The IR source generates radiation using heated compounds like silicon carbide.[108] The IR beam is then passes through a collimator, where the beam is focused towards a beam splitter. The beam splitter is a Michelson interferometer, which is widely considered the core of the FTIR, and allowed researchers to generate IR spectrum in seconds as compared to longer times previously.[109] The interferometer splits the IR beam into two beams, one beam travels towards a fixed mirror, while the other travels to a moving mirror, such that the intensity difference between the two beams when recombined is measured as a function of the difference of the beam paths. After recombining, the IR beam travels to the sample cell, where compound absorbs IR radiation. In this region, the sample is either in a solution/gas cell or an attenuated total reflectance (ATR) attachment where compound can be studied in liquid or solid state. The schematic of the ATR sampling method is seen in figure 2.7. An IR beam which is focused through a lens and the incident beam is directed through an ATR crystal and the beam is reflected internally in the ATR crystal, under a method called, total internal reflection, where it forms an evanescent wave extending into the sample up to a 2 μm depth.[110] Following exiting of sample, the beam is captured by a detector, generally a pyroelectric detector. The resulting readout on a computer shows an interferogram, where a Fourier transform is applied resulting in FTIR spectrum.

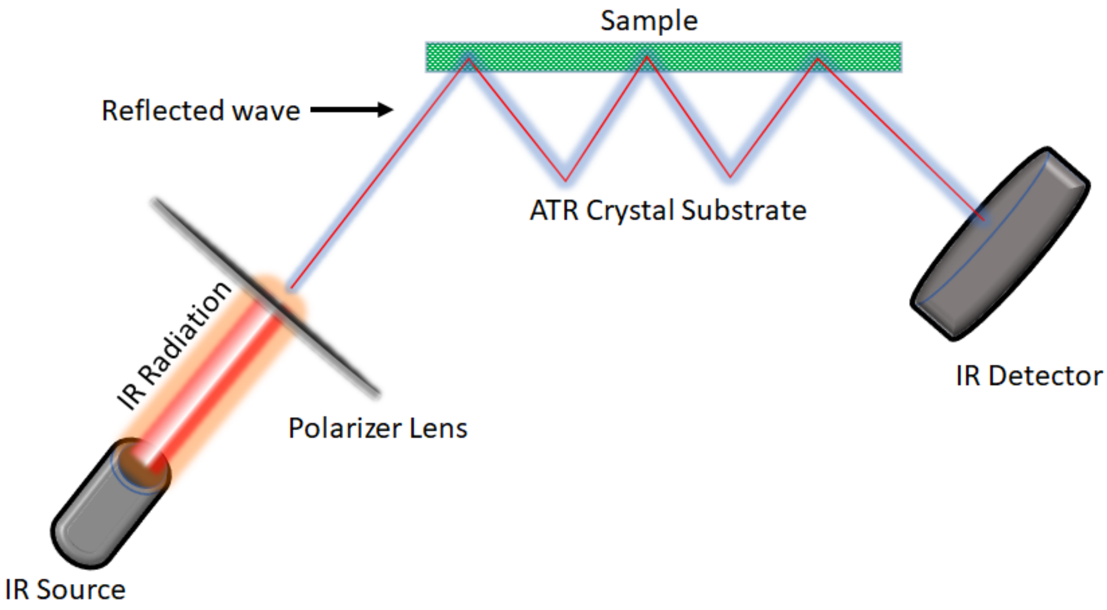

Figure 2.7. Schematic representation of the principle of ATR

2.6 Scanning Electron Microscopy

Scanning electron microscopy (SEM) is a technique that that scans a focused beam of high-energy electrons across a solid sample, generating a variety of signals to characterize the samples. These signals derive from the electron-sample interactions which reveals information on sample morphology, geometry, and in some set-ups chemical information. [111-112] The instrumental SEM schematic is shown in figure 2.8, where the movement and manipulation of electrons is visualized.

An electron gun which is generally fitted with a low-cost tungsten cathode filament, is thermionically heated to produce high energy electrons, typically up to 40 keV. This beam is then received by an anode which guides the electrons through the open core. Upon exiting the anode, the beam is focused by a converging lens, to a narrow beam, usually up to 5 nm in diameter. This narrow electron beam then enters a scanning coil, which configures the electron beam scanning into a raster movement. This raster scanning is then applied to the selected area on the surface of the sample, effectively decelerating the incident electrons on the sample causing various signals to be produced. The signals are generated by the electron-sample interaction, which includes the creation of secondary electrons, backscattered electrons, and characteristic x-rays. The detection of secondary electrons produces the SEM image seen on the TV screen, revealing the morphology and topography of the sample, which have area and spatial resolution as low as 25 μm^2 and 50 nm. The backscattered electrons detected reveal the differing contrast composition in multiphasic materials. The characteristic x-rays are produced by inelastic collisions from incident electrons onto electrons in discrete orbitals, effectively promoting electrons to a higher energy state, and releasing x-rays when retuning to lower states. The characteristic x-rays can be used to determine elemental compositions when the SEM is coupled with energy disruptive spectroscopy (EDS). [113]

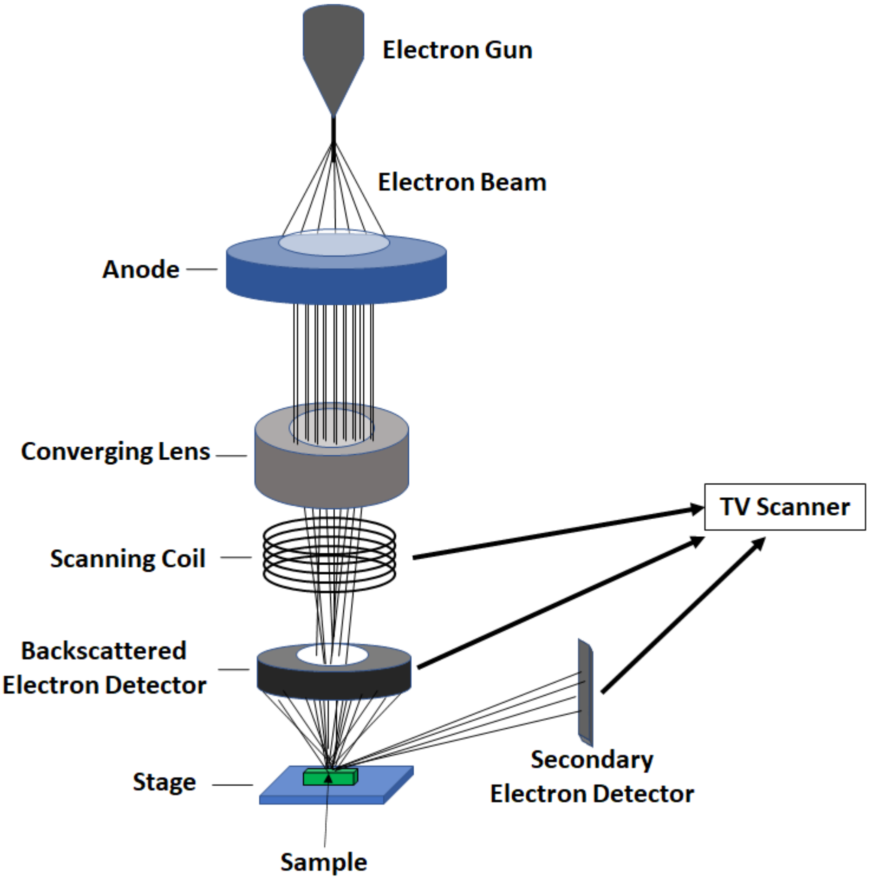

Figure 2.8. Schematic representation of SEM imaging

2.7 Atomic Force Microscopy

Atomic force microscopy (AFM) is a scanning probe microscopic technique, invented by Binnig, Quate and Gerber in 1986.[114-115] This technique is utilized to image the topography of a sample surface with nanometer scale resolution, reaching lateral and vertical resolutions as high as 0.1 Å and 0.01 Å. This technique was developed to image non-conductive surfaces, which scanning tunneling microscopy could not achieve, opening the doors to image a range of new materials.[116-119] AFM imaging can also be used on delicate systems like proteins, where application of force is as small as 10^{-18} N. [119] AFM functions by scanning a selected area of a surface using sharp tip, generally Si_3N_4, using a raster pattern, effectively mapping the topography of the surface. This can be accomplished using various imaging modes, including constant contact and intermittent contact. In this dissertation, intermittent contact mode, also called tapping mode, was utilized. This is accomplished by vibrating the tip very close to its resonant frequency by subjecting it to an oscillating voltage. As the tip is vibrating, it is brought close to the sample surface, such that the decreased contact allows the desired level of dampening to be attained. The level of dampening is tracked by reflecting a laser spot from the hind of the cantilever, such that the reflected beam is focused onto a split photodiode detector (SPD) as shown in figure 2.9.

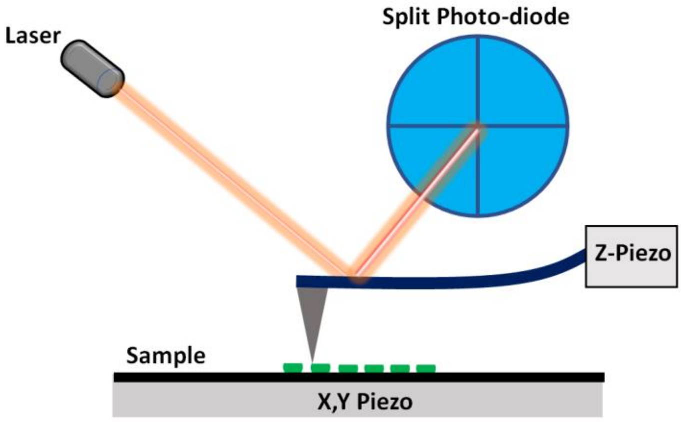

Figure 2.9. Schematic representation of AFM imaging

The beam position is monitored, until the desired dampening is achieved, and feed-back loop is created such that the piezo on the cantilever can maintain the tip-surface distance for desired dampening. This piezo movement allows precise mapping of the topography of a surface. Another readout from tapping mode is the characterization of mechanical properties of different samples, i.e., soft or sticky, this is achieved through determination of the offset-phase of the cantilever oscillation.

CHAPTER III

A Green Approach to Producing Polymer Microparticles for Local Sustained Release of Flavopiridol

3.1 Introduction

Injectable drug loaded microparticles have been used for applications such as bone regeneration and these microparticles are synthesized with a range of different materials suited to its application.[120] For examples, silica particles are mostly used due to their high range of surface functionality with different functional groups. Microparticles of poly(lactic-co-glycolic acid) (PLGA) have shown great promise in local sustained delivery of medicine as well as improving osteoinductivity and bone healing, owning to their biodegradable property and high biocompatibility.[30, 35-39] These particles were typically produced via conventional emulsion, which frequently utilized toxic organic solvents, such as dichloromethane (DCM).[40-41] Conventional emulsion has advantages of simplicity, but frequently exhibits limitations such as batch-to-batch irreproducibility in drug release kinetics, primarily attributed to large variation in particle size and intra-particulate structure.[42] Microfluidic flow-focusing device (MFFD) was introduced to address these limitations and are capable of producing monodispersed particles such as quantum dots, photonic particles, textiles, and polymer microparticles.[34, 42-47] MFFD typically produce particles with near monodispersion, and high reproducibility in size, load, and drug release profiles. The process also had less waste due to lower working volume.[48]

[ʃ] Reproduced in part with permission from Chemical Research in Chinese Universities (1) Owen,

M. J.; Yik, J. H. N.; Ye, C.; Netto, B.; Haudenschild, D. R.; Liu, G.-y. A Green Approach to Producing Polymer Microparticles for Local Sustained Release of Flavopiridol. *Chemical Research in Chinese Universities* **2021,** *37* (5), 1116-1124. Copyright © 2021 Springer Nature

Despite these new advances, DCM has remained as the organic phase solvent in most MFFD syntheses.[42, 49-50] DCM is a volatile organic compound (VOC) and a known carcinogen,[51] referred to as a Class 2 solvent as per International Council for Harmonization (ICH), whose residual amounts in medicinal products is limited to no more than 600 ppm.[51-52] DCM was recently banned for consumer use, to protect health and environment regulated by the United States government and environmental protection agency (EPA).[53] Green chemistry principles are strongly encouraged in chemical synthesis[54], thus it is essential to seek an alternative and green solvent to replace DCM in production of drug delivery polymer particles.

Using flavopiridol (FLAP) encapsulated in PLGA microparticles[40-41, 72, 121-122] as an example, this work reports the use of dimethyl carbonate (DMC) in the encapsulation of FLAP in PLGA particles. FLAP is a cyclin-dependent kinase inhibitor currently in development for anti-cancer[123] and osteoarthritis treatments.[64, 68, 124] DMC is classified as a green solvent [125] and exempt from restrictions of VOC by the EPA in 2009.[52] Our results demonstrate that using the green solvent does not hinder the synthesis process or product quality in MFFD. In fact, the use of DMC preserves the narrower size distribution, with high reproducibility in particle size and drug load. In addition, the particles exhibited drug release profiles more desirable for local sustained release in joints, an effective means for preventing post-traumatic osteoarthritis (PTOA).[124] Further, the biological activity and cytotoxicity of the FLAP encapsulated PLGA are measured via in vitro cell-based assays. The sustainability and greenness are assessed by comparing our MFFD synthesis using DMC with that of using DCM.

3.2 Materials and Methods

3.2.1 Materials

PLGA (PURASORB PDLG 5004A 50:50 DL-lactide:glycolide) was purchased from Corbion (Amsterdam, Netherlands). DMC, DCM, dimethyl sulfoxide (DMSO), poly(vinyl alcohol) (PVA) (80% hydrolyzed, MW 9000-10000; 98-99% hydrolyzed, MW 30000 - 40000), and tween 20 were all purchased from Sigma Aldrich (St. Louis, MO). Phosphate-buffered saline (PBS) (1X) was purchased from Mediatech (Manassas, VA). FLAP was purchased from Cayman Chemical Company (Ann Arbor, MI). Dulbecco's modified Eagle's Medium (DMEM), Fetal Bovine Serum (FBS), and 96 well plates were purchased from Fisher Scientific (Hampton, NH). Human embryonic kidney 293 cells (HEK-293) were purchased from ATCC (Manassas, VA). Nuclear factor kappa B (NF-κB) reporter (cat # H-60650) were purchased from BPS Bioscience (San Diego, CA). Tumor necrosis factor alpha (TNF-α) was purchased from Peprotech (Rocky Hill, NJ). 1X Lysis reagent (Cat # E1500) and Luciferase substrate (Cat # E151Z) were purchased from Promega (Madison, WI). CyQUANT LDH Cytotoxicity assay kit (Cat # C20300) was purchased from Invitrogen (Carlsbad, CA). Liquid and gaseous nitrogen were purchased from UC Davis (Davis, CA). Poly(tetrafluoroethylene) (PTFE) tubing was purchased from Cole-Parmer (Vernon Hills, IL). Ultrapure water with a resistivity of 18.2 MΩ·cm was generated using a Millipore Milli-Q system (EMD Millipore, Billerica, MA).

3.2.2 Production of FLAP-Loaded PLGA microparticles

The flow-focusing microfluidic device was fabricated as per our design (using AutoCAD 2018) by uFluidix (Toronto, Canada). The channels, shown in Figure 3.1, are 120 μm tall, and 300 μm wide, tapering to 100 μm at the crossing. Each device was made of poly(dimethyl siloxane)

(PDMS) using soft lithography technique[90] and bonded to a glass slide. The microfluidic channels were pretreated to hydrophilic using PVA, following protocols described previously.[91] Briefly, the microfluidic device was activated via plasma treatment (Harrick Plasma, Ithaca, NY) for 5 min, followed by filling the channels with 1% PVA aqueous solution for 15 min. Afterward, PVA solution was removed from the channel by blowing N_2 gas and then was placed the entire device in an oven at 110 ℃ for 15 min. The PVA treatment was repeated 3 times to ensure the interior of the channel is coated by PVA, i.e., becomes hydrophilic.

FLAP loaded PLGA microparticles were prepared following similar procedures reported previously.[42] Briefly, FLAP and PLGA were dissolved in DMC to the designated concentration, then the solution was pulled into a syringe mounted on a syringe pump (New Era Pump Systems Inc., Farmingdale, NY). The 1% w/v PVA aqueous solution was prepared following standard protocols[91] and was transferred into two syringes mounted on a syringe pump. The three outputs from the syringes were connected via PTFE tubing to the inlets of the three channels on the device, as illustrated in figure 3.1. The reaction began by flowing the dispersed organic phase and the continuous aqueous phase at designated flow rates of Q_d and Q_c, respectively. The organic phase droplet formation was visualized in-situ, using an inverted microscope (Olympus corp., Tokyo, Japan) equipped with a Photron AX-100 high-speed camera (Photron USA Inc., San Diego). The droplet containing liquid flowed through the outlet channel of the microfluidic device (Fig. 1) and was collected by a round bottom flask containing 1 % w/v PVA. Duration of synthesis ranged from 1-10 hr, depending on the amount of material needed. The flask was mounted to a Buchi R300 rotational evaporator (Buchi corp., New Castle, DE) to remove DMC under reduced pressure at room temperature (40 mbar, 5 min). Then the remaining PLGA microparticles were collected and subject to centrifugation (2500 RPM, 10 min) and washed 3X with Milli-Q water to remove residual PVA. Finally, the microparticles were quickly frozen in liquid nitrogen and lyophilized (Labconco corp., Kansas City, MO) to dryness overnight.

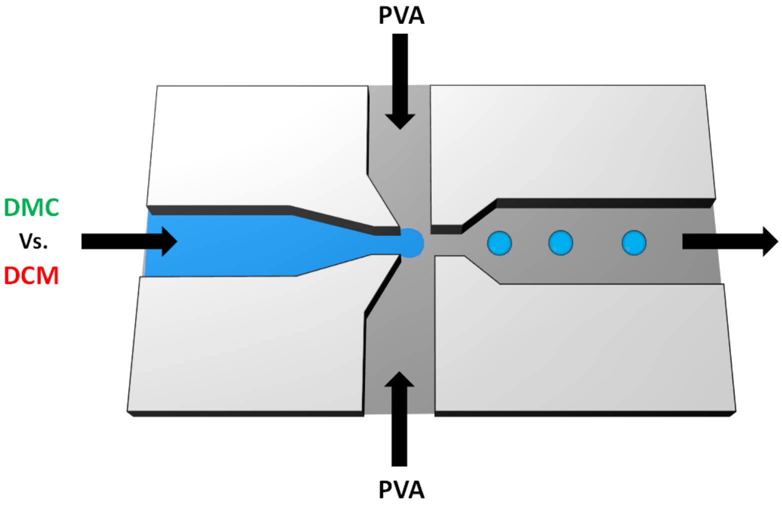

Figure 3.1 Schematic representation of the microfluidic flow-focusing device using DMC versus DCM as the organic phase solvent. The organic phase input channel is highlighted in blue, while the two inputs of aqueous phase containing PVA are in grey. The droplets formed due to flow focusing were collected for subsequent treatment including washing and drying to produce PLGA microparticles.

3.2.3 Measurements of load and encapsulation efficiency of FLAP in PLGA microparticles

The amount of FLAP encapsulated in PLGA microparticles was determined by first collecting and then dissolving ~1 mg of particles ($m_{particles}$) in 1 mL DMSO. The solution was subject to UV-Vis spectroscopy using a Denovix DS-11 spectrometer (Denovix Inc., Wilmington, DE), from which absorbance (A) at characteristic FLAP peak was measured. The molar extinction coefficient (ϵ) of FLAP was calibrated using standard solutions range from 1 to 100 μM, then the concentration of FLAP, c, in the DMSO solution was calculated using Beer's Law in eq. (1),

$$A = \epsilon \mathrm{cL} \tag{1}$$

where L = 1 cm is the light path through the solution. With the determination of c, the encapsulated mass of FLAP ($\mathrm{m_{FLAP}}$) in the PLGA particles was determined by multiplying c with the volume (1.00 mL) and molar mass of FLAP. Then the loading capacity (LC) was be quantified using eq. (2).

$$\mathrm{LC} = \left(\frac{\mathrm{m_{FLAP}}}{\mathrm{m_{particles}}}\right) \times 100\% \tag{2}$$

The encapsulation efficiency (EE) is defined as the mass of FLAP encapsulated (m_{FLAP}) divided by that of the initial FLAP used ($\mathrm{m_{FLAP,initial}}$). The $\mathrm{m_{intial}}$ was determined using eq. (3)

$$\mathrm{m_{FLAP,initial}} = \mathrm{c_{FLAP} Q_{org} t} \tag{3}$$

where, $\mathrm{c_{FLAP}}$ is the concentration of FLAP in the syringe, $\mathrm{Q_{org}}$ is the organic phase syringe pump flow rate, and t is the time of collection. The EE is defined and calculated by dividing the $\mathrm{m_{FLAP}}$ by the initial mass of FLAP ($\mathrm{m_{FLAP,intial}}$) following eq (4).

$$\mathrm{EE} = \left(\frac{\mathrm{m_{FLAP}}}{\mathrm{m_{FLAP,initial}}}\right) \times 100\% \tag{4}$$

3.2.4 Scanning Electron Microscopy Imaging

The particle geometry and size were determined using scanning electron microscopy (SEM) imaging using a field emission SEM (S-4100T, Hitachi High Technologies America, Inc., Pleasanton, CA). The sample preparation involved depositing 10 μL of PLGA particle dispersion in Milli-Q water onto an Al-stub, then washing with milli-Q water and drying. The dried sample was then coated with 10 nm of gold via sputter coating (Ted Pella Inc., Redding, CA) and transported to the SEM vacuum chamber. For SEM imaging, typical acceleration voltage and emission current were 2 kV at 10 μA, respectively. The SEM images were processed in Image J, from which the microparticle diameter and dispersity were determined. The dispersity, quantified using the coefficient of variation (CV), was calculated using eq. (5), where σ is the standard deviation, $\bar{\mathrm{d}}$ represents the average diameter. We used more than 100 particles for determination of CV in each set of samples.

$$\mathrm{CV} = \left(\frac{\sigma}{\bar{\mathrm{d}}}\right) \times 100\% \tag{5}$$

3.2.5 Measurement of the release of FLAP from PLGA microparticles

In vitro release experiments were carried out following established protocols[42] to determine the FLAP release kinetics using PLGA microparticles as carriers. First, 4 mg of lyophilized PLGA microparticles loaded with FLAP were dispersed in 0.5 mL of 1X PBS/0.2% Tween-20 aqueous solution at 37 °C. The Tween-20 solution was added to ensure sink conditions, such that the dissolution medium can dissolve at least two times the amount of FLAP encapsulated.[126] At selected time points, the solution was centrifuged at 4000 rpm for 5 min and the supernatant was extracted for determination of FLAP concentration using UV-Vis spectroscopy (see previous section). The particles were then dispersed again in 0.5 mL fresh medium until the next time point. The in vitro release at given time point, t, were quantified by the cumulative percentage of FLAP, defined as the total released divided by the total encapsulated FLAP, $\mathrm{m}_{\mathrm{FLAP}}$. At each given time point, the FLAP mass in the supernatant solution, m_{t} , can be determined using UV-Vis measurements of its FLAP concentration. Therefore, the cumulative percentage of FLAP can be calculated using eq (6) by adding the amount of FLAP released at each time point ($\sum_{t=0}^{t=t_f} m_t$) until the designated time, t, then divided by the amount of FLAP encapsulated (m_{FLAP}).

$$\text{Cumulative Release (\%)} = \frac{1}{\mathrm{m}_{\mathrm{FLAP}}} \sum_{\mathrm{t=0}}^{\mathrm{t=t_f}} \mathrm{m}_{\mathrm{t}} \tag{6}$$

3.2.6 Cytotoxicity Assay

The toxicity of released FLAP was measured in HEK293 cells using the CyQUANT LDH cytotoxicity assay kit according to the manufacturer's instruction and as reported previously.[64] Release medium was collected from the in vitro release experiments described above for both FLAP-loaded and empty PLGA microparticles. The concentration of released FLAP was determined using UV-Visible spectroscopy at 274 nm, and subsequently diluted with culture media (DMEM + 10% FBS) to designated concentrations of FLAP. To determine cytotoxicity, cells were seeded in a 96-well plate (10,000 cells/well) and cultured in an incubator (37 $°C$, 5% CO2). After 24 hours, cells were treated with 200 μL of culture media with different concentrations of FLAP in each well. After 5 hours, 50 μL of media was collected and mixed with 50 μL of LDH assay buffer, incubated for 30 minutes at room temperature for each well. Then 50 μL of stop solution was added and the optical density at 490 and 680 nm was measured with a fluorescence plate reader (Synergy HT plate reader, BioTek Instruments). The effects of release medium containing FLAP on the absorbance reading was compared to that of control cells, i.e., cells treated with media only.

3.2.7 Bioactivity Assays

The bioactivity of FLAP released from PLGA microparticles was determined by a luciferase reporter assay as described previously.[127] The release medium was collected and diluted to various FLAP concentration as described in the cytotoxicity assay. Briefly, a HEK293 cell line harboring a luciferase reporter gene driven by a NF-kB promoter was seeded in a 96-well plate at ~50% confluency (5,000 cells/well in 96-well). Cells were treated in triplicate with 0.6 nM of TNF-α, in the presence or absence of 200 μL culture media containing released FLAP at designated concentrations in each well. After 16 hours, cells were lysed with 50 µL of 1X lysis reagent in each well. Then 5 µL of lysate were mixed with 25 μL of luciferase substrate for each well and luminescence was measured by a luminometer (GLOMA X 20/20 Luminometer, Promega, Madison, WI).

3.2.8 Green E-Factor Calculation

The green E-Factors of using DMC versus DCM were quantified to demonstrate the greenness and sustainability of our PLGA microparticle synthesis. The simple E factor (sEF) and the complete E factor (cEF) were based on a simple mass balance using previously described methods.[128] This method was applied to quantify our PLGA microparticle formation via MFFD using DCM versus DMC:

$$\mathrm{sEF} = \frac{\sum \mathrm{m(raw\ mat.)} + \sum \mathrm{m(reag)} - \mathrm{m(prod.)}}{\mathrm{m(prod.)}}$$

$$= \frac{\mathrm{m_{PLGA}} + \mathrm{m_{FLAP,initial}} + \mathrm{m_{PVA}} - \mathrm{m_{particles}}}{\mathrm{m_{particles}}} \tag{7}$$

$$\mathrm{cEF} = \frac{\sum \mathrm{m(raw\ mat.)} + \sum \mathrm{m(reag.)} + \sum \mathrm{m(solv.)} + \sum \mathrm{m(water)} - \mathrm{m(prod.)}}{\mathrm{m(prod.)}}$$

$$= \frac{\mathrm{m_{PLGA}} + \mathrm{m_{FLAP,initial}} + \mathrm{m_{PVA}} + \mathrm{m_{org.solv.}} + \mathrm{m_{water}} - \mathrm{m_{particles}}}{\mathrm{m_{particles}}} \tag{8}$$

where $\sum \mathrm{m(raw\ mat.)}$ represents the total mass of PLGA ($\mathrm{m_{PLGA}}$) and FLAP ($\mathrm{m_{FLAP,initial}}$) in microfluidic synthesis of FLAP-loaded PLGA microparticles. $\sum \mathrm{m(reag)}$ represents the mass of all the other reagents used in the synthesis, e.g., mass of PVA ($\mathrm{m_{PVA}}$). The m(prod.) was the total mass of PLGA particles produced, i.e., $\mathrm{m_{particles}}$. $\sum \mathrm{m(solv.)}$ and $\sum \mathrm{m(water)}$ were the total mass of organic and aqueous solvents, respectively, in our MFFD synthesis, $\mathrm{m_{org.solv.}}$ and $\mathrm{m_{water}}$, respectively. The descriptions and values inputted into equations 7 and 8 are shown in Table 3.3

(discussed in the next section).

3.2.9 GSK Greenness Calculation

The greenness of the organic solvents used in our PLGA microparticle synthesis was determined using a GlaxoSmithKline (GSK) guide.[124, 129] The GSK guide contains four main green metric categories, and each category contains multiple assessment areas that are individually assessed. The assessment areas for each solvent are Incineration (Ic), Recycle (Rc), Biotreatment (Bt), VOC emissions (Vc), Environmental impact aqueous (Aqc), Environmental impact air (Aic), Health hazard (HHc), Exposure control (EPc), and Flammability & Explosion (FEc), Reactivity (RSc). Each area is assigned a score ranging from 1 – 10, where the highest score represents lowest environmental impact. The four categories used in this green metric were waste (Wm), environment (Em), human health (HHm), and process safety (PSm). The four categories are calculated in Eqs. (9)-(12) below.

$$\mathrm{Wm} = \sqrt[4]{\mathrm{Ic\ x\ Rc\ x\ Bc\ x\ Vc}} \tag{9}$$

$$\mathrm{Em} = \sqrt{\mathrm{Aqc\ x\ Aic}} \tag{10}$$

$$\mathrm{HHm} = \sqrt{\mathrm{HHc\ x\ EPc}} \tag{11}$$

$$\mathrm{PSm} = \sqrt{\mathrm{FEc\ x\ RSc}} \tag{12}$$

After determining the four category values of each solvent, the overall GSK greenness was calculated using eq. (13).

$$\mathrm{GSK\ Greenness} = \sqrt[4]{\mathrm{Wm} \times \mathrm{Em} \times \mathrm{HHm} \times \mathrm{PSm}} \tag{13}$$

3.3 Results and Discussion

3.3.1 Encapsulation of FLAP in PLGA Microparticles

Using MFFD, we began our synthesis of FLAP encapsulated PLGA microparticles. DMC was used as the organic phase solvent, in which 10 mg/mL PLGA was dissolved. FLAP was added to the same DMC until 1.22% (w/w) concentration. Under the aqueous phase flow rate, $Q_{aq} = 6$ mL/h and organic phase flow rate $Q_{org} = 0.1$ mL/h, the organic phase was sheared by the aqueous phase, producing spherical droplets at the orifice. The PLGA microdroplets were clearly visible at the cross section and to the exit channel. Following the post synthesis treatment and drying described, the particles were imaged using SEM (Figure 3.2A). The particles are uniform with diameter measured 15.1 ± 0.6 μm, (CV = 3.9%). Increasing the concentration of PLGA, while keeping other conditions constant, yielded larger particles. As summarized in Table 3.1, increasing the PLGA concentration to 40 mg/mL allowed production of particles with a diameter of 32.4 ± 1.0 μm, (CV = 3.1%). PLGA particles without drug encapsulation were produced using the same protocols without adding FLAP into the organic phase, as also included in Table I. By varying the PLGA concentration from 5 - 50 mg/mL, while keeping flow rates constant, and particle sizes could be controlled from 5 to 50 μm.

Table 3.1 Conditions in MFFD synthesis of PLGA microparticles in correlation to the particle size and FLAP loading efficiency.

[PLGA] (mg/mL)	[FLAP] (mg/mL)	Q_{aq} (mL/hr)	Q_{org} (mL/hr)	Diameter (μm)	CV (%)	LC (%)	EE (%)
10	0.122	0.1	6	15.1 ± 0.6	3.9	0.65 ± 0.12	55.0 ± 3.0
10	0	0.1	6	15.0 ± 0.5	3.3	0	0
40	0.358	0.1	6	32.4 ± 1.0	3.1	0.58 ± 0.02	65.2 ± 0.1
40	0	0.1	6	30.3 ± 0.9	3.0	0	0

The loading capacity of FLAP was measured using UV-Vis absorption spectroscopy after fully dissolving the particles. Figure 3.2B compares the spectra of the particle solutions (green line) with a standard 100 μM FLAP in DMSO (black solid line), and that of placebo PLGA microparticles (broken line). The spectrum from the encapsulated PLGA particles (FLAP-PLGA) resembles that of the standard flavopiridol solutions. The PLGA microparticles lack an absorption peak at 380 nm. Thus, the absorbance at 380 nm was used to determine the total FLAP encapsulated in the PLGA microparticles. With the extinction coefficient at 380 nm determined to be 5,456 $M^{-1}cm^{-1}$, the LC value was calculated to be 0.65 ± 0.12 % (w/w). The EE value of these microparticles reached 55.0 ± 3.0 %. To the best of our knowledge, this is the first time that FLAP was encapsulated within PLGA particles using a green solvent and the loading capacity, 0.65 % (w/w), is similar to previous work with FLAP encapsulation using conventional emulsion and DCM.[40] The 32.4 μm microparticles exhibited similar LC of 0.58 ± 0.02 % (w/w), and EE = 65.2 ± 0.1 %. The trend that EE increases with the increasing of microparticle diameter is consistent with the behavior of PLGA microparticles synthesized using conventional and MFFD.[59]

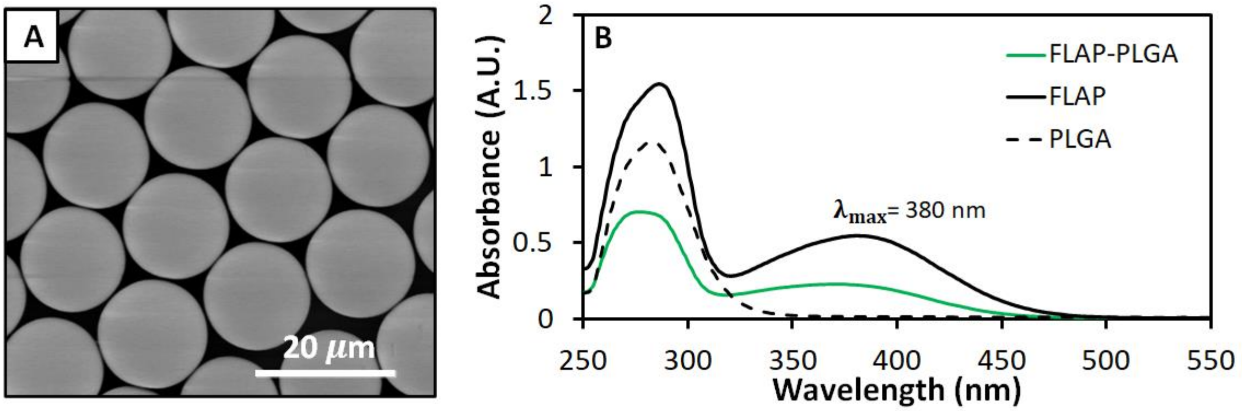

Figure 3.2 (A) An SEM image of PLGA microparticles with FLAP encapsulation made via MFFD under conditions summarized in Table I, first row. (B) Absorption spectra of the same batch of sample after dissolving in DMSO (green solid line), displayed with that of 100 μM FLAP in DMSO (black solid line) and PLGA microparticles (black broken line). The absorption at $\lambda_{max} =$ 380 nm was used to quantify FLAP concentration and calculate mass of loading.

3.3.2 Targeted release kinetics in order to fulfill sustained release at human joint

In delivery of FLAP encapsulated 15.1 μm microparticles (FLAP-PLGA) to human joint, the required concentration of FLAP in the synovial fluid should be 300 nM, preferable if maintained for at least 30 days.[40, 64, 72] Two chemical processes impact the concentration of soluble FLAP in the joint space, as illustrated in Scheme 3.1: dissolving of FLAP from the FLAP-PLGA microparticles, and clearance of soluble FLAP from the synovial fluid by the body. The former follows zeroth order kinetics, while the latter follows 1st order kinetics. It is also known that the clearance rate, measured by half-life of the drug, for adult knee joints, is about 2 hrs. [130] As shown in figure 3.3, FLAP is incorporated in PLGA microparticles and added to a saline solution of 300 nM of soluble FLAP, where it is delivered to the synovial joint of an injured human knee via intraarticular (IA) injection. Following injection, the fate of flavopiridol is shown in scheme 3.1 and described in figure 3.3, where initially the concentration of flavopiridol in the synovial joint is 300 nM and is quickly replenished with a half-life ($t_{1/2}$) of 2 hours.

Scheme 3.1 Chemical kinetics of FLAP from PLGA microparticles upon delivery to the synovial environment.

$$\textbf{FLAP-PLGA (s)} \xrightarrow{k_{\text{Release}}} \textbf{FLAP (aq)} \xrightarrow{k_{\text{Clearance}}} \textbf{FLAP (outside synovial)}$$

In order to reach the local sustained release required, the soluble FLAP concentration must be maintained at ~ 300 nM. Therefore, the delivery mixture targets to meet two conditions:

(a) The delivery mixture contains FLAP-PLGA particles plus soluble FLAP at ~ 600 nM, and the total volume is approximately equal to the synovial fluid at the joint. As such the initial FLAP concentration would be ~ 300 nM.

(b) The dissolving of FLAP from FLAP-PLGA and the clearance of FLAP from the synovial fluid must reach a steady state (SS). In another word, the kinetics of our particles must satisfy the kinetics equation (1) below.

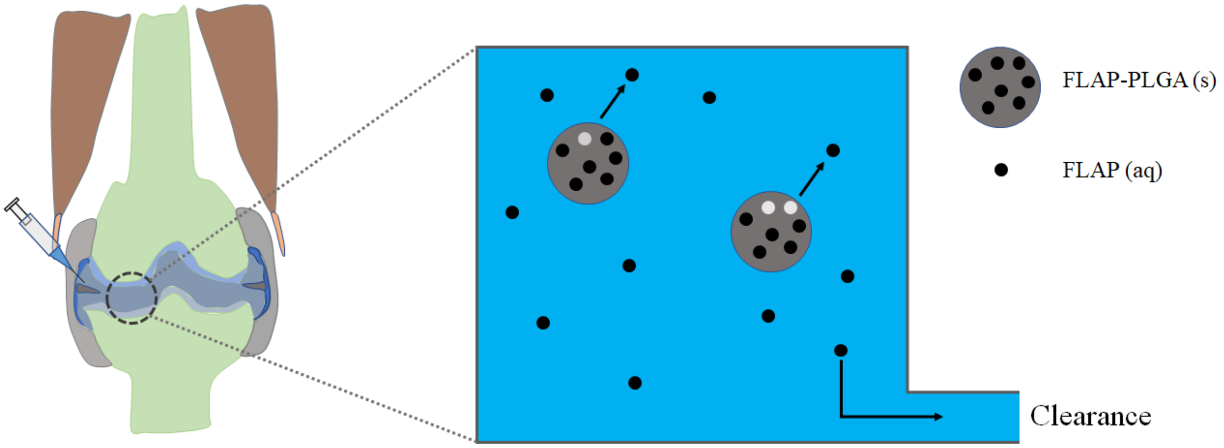

Figure 3.3 Schematic of Intraarticular injection into the Synovial joint and Kinetics of Flavopiridol Transport.

$$\frac{d[\mathrm{FLAP}]}{dt} = k_{\mathrm{release}} - k_{\mathrm{clearance}}[\mathrm{FLAP}] = 0 \tag{14}$$

Where $k_{release}$ and $k_{clearance}$ are rate constant of FLAP dissolving from PLGA and being cleared by the body from joint, respectively.

Plugging in the known clearance rate, $k_{\mathrm{clearance}} = \frac{\ln(2)}{t_{\frac{1}{2}}}$ and [FLAP] = 300 nM into eq. (14) yields eq. (15)

$$k_{\mathrm{release}} = \frac{\ln(2)}{t_{\frac{1}{2}}}[\mathrm{FLAP}] = 104\ \mathrm{nM/hr} \tag{15}$$

The desired value of $k_{release}$ = 104 nM/hr, in other units, 2495 nM/day.

The Food and Drug Administration, states that 80% of drug released is considered complete, therefore the slope can be found using the following analysis.

$$\frac{w_{30days}}{w_{tot}} = \frac{k_{release}\ x\ 30\ days\ x\ V\ x\ MW}{w_{tot}} = 80\ \% \tag{16}$$

$$\frac{w_{1day}}{w_{tot}} = \frac{k_{release}\ x\ 1\ day\ x\ V\ x\ MW}{w_{tot}} = X \tag{17}$$

$$\frac{1}{30} = \frac{X}{80\%} \tag{18}$$

$$X = \frac{80\ \%}{30} = 2.7\% \tag{19}$$

As shown above in eq. (16), the cumulative weight of FLAP until 30 days ($w_{30\ days}$) is normalized by the total encapsulated weight of FLAP (w_{tot}) and set equal to 80%. This can be rewritten using dimensional analysis which involves the product of the release constant found in eq. (15), 30 days, volume of synovial fluid (V), and the molecular weight of FLAP (MW). To determine the 1-day release %, the cumulative weight of FLAP released after 1 day ($w_{1\ day}$) is normalized using w_{tot} and follows the same dimensional analysis as eq. (16). The slope (X) is determined by the ratio of eq. (17) and eq. (16). This operation as shown in eq. (18-19) yielding a slope of 2.7%/day.

3.3.3 Drug Release Profiles

The estimated therapeutic dosage of FLAP, in vivo, is 300 nM for at least 21 days with 30 days preferred.[40, 64, 72] The half-life of drug clearance from the joint is approximately 2 hrs, following preclinical pharmacokinetics of mice.[130] Thus the release kinetics for FLAP-PLGA must reach 2,495 nM/day. In addition, the Food and Drug Administration (FDA) guidance for the pharmaceutical industry states that drug release is complete at 80% or an asymptote is reached.[131] Assuming linear release, the corresponding cumulative release rate in vitro is calculated to be 2.7%/day of FLAP , as shown in figure 3.4 (broken line). Further, the FLAP-PLGA release profile needs to maintain 300 nM FLAP concentration within the first 30 days. Collectively, if our 15.1 mm FLAP-PLGA particles were used for a knee joint, the final formulation in the syringe for injection would be 5 mL of synovial fluid containing 1.2 μg of soluble FLAP (i.e., initial concentration of 300 nM) and 23.1 mg of FLAP-PLGA (see also the SI for detailed calculations).

The release profiles for the 15.1 mm FLAP-PLGA microparticles (row 1, Table 1) was measured for 30 days (green dots) and are displayed in the same coordinate as the required profile in figure 3.4. The release profile for the 15.1 μm particles is approximately linear, with the slope of 2.6%/day as per least square fitting (R^2 = 0.98). This release profile clearly satisfies the pharmacokinetics in vivo. For comparison, particles made from conventional emulsion using DCM (solid black dots) are plotted also in the same coordinate. The average diameter for these PLGA particles as measured via SEM imaging is 18.9 μm, with diameter ranging from 3.8 to 30.9 μm.[40] The in vitro release profile of these particles (black dots in Figure 3) is not linear, beginning with a rapid release ~6.3%/day for 4 days, then a slower release of ~ 1.2%/day until day 40. The narrow size distribution and degradation behavior (see next section) of our FLAP-PLGA particles are likely responsible for a more controllable and linear release profile.

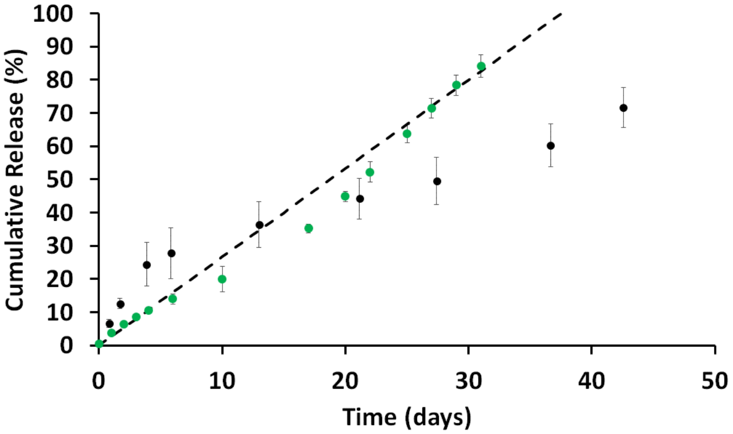

Figure 3.4 In vitro release profiles of the 15.1 μm PLGA particles produced via MFFD using DMC (green circles), and that of in vitro profiles from conventional emulsion (black circles), and the targeted linear release profile (dashed black line). In each synthesis method, data are expressed as mean +/- SD from n = 3 independent batches of microparticles.

3.3.4 The PLGA microparticles retain structural integrity during sustained release

The degradation of the PLGA microparticles were monitored using SEM imaging of these particles taken from designated time point during the in vitro release. Twin samples were used, one for kinetics and another for degradation measurements, to assure reliable comparison. Figure 3.5 shows the representative SEM images of the 15.1 μm particles during in vitro release. Initially (0 day), the microparticles had a spherical shape with a smooth exterior morphology and a uniform diameter of 15.1 ± 0.6 μm. At 3 days, most particles remained similar in size, geometry and morphology, a small portion, 27%, of the particles began to deform, i.e., flattening to some degree. At 7 days, the exterior surface of the particles appeared rough, with small surface dimples (< 1 μm) all over. The geometry of the particles also begun to deform with indentations, and the diameter of the microparticles increased to 17.0 ± 0.9 μm, indicating the geometry change from a sphere to a pancake. At 21 days, most microparticles flattened into a pancake shape, with diameters measured 29.2 ± 4.2 μm. The surfaces of these pancake shaped particles appeared rough with small number of cracks at the sides. At 30 days, almost all microparticles have flattened, and many degraded into pieces. The SEM investigations indicated that our particles remained intact for at least 3 weeks.

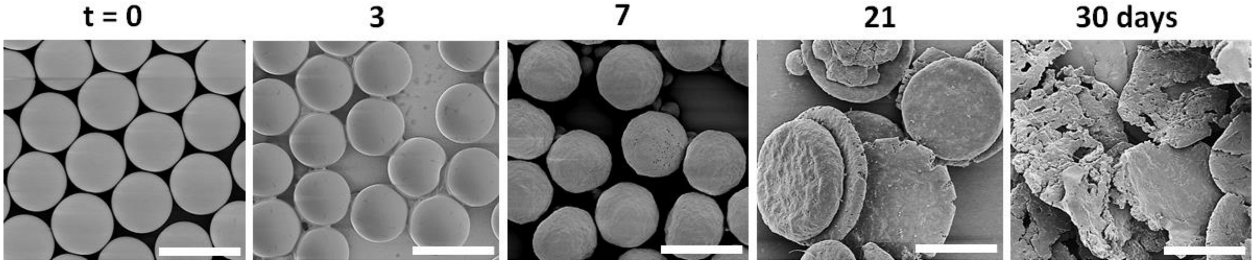

Figure 3.5 SEM imaging of PLGA microparticles taken at designated time points (see above the images) during in vitro release measurements. Scale bars = 20 μm.

The particle size distribution was determined for the spherical microparticles undergoing in vitro release in figure 3.6. As shown below in figure 3.6, the particle distribution from days 0 – 7 were determined.

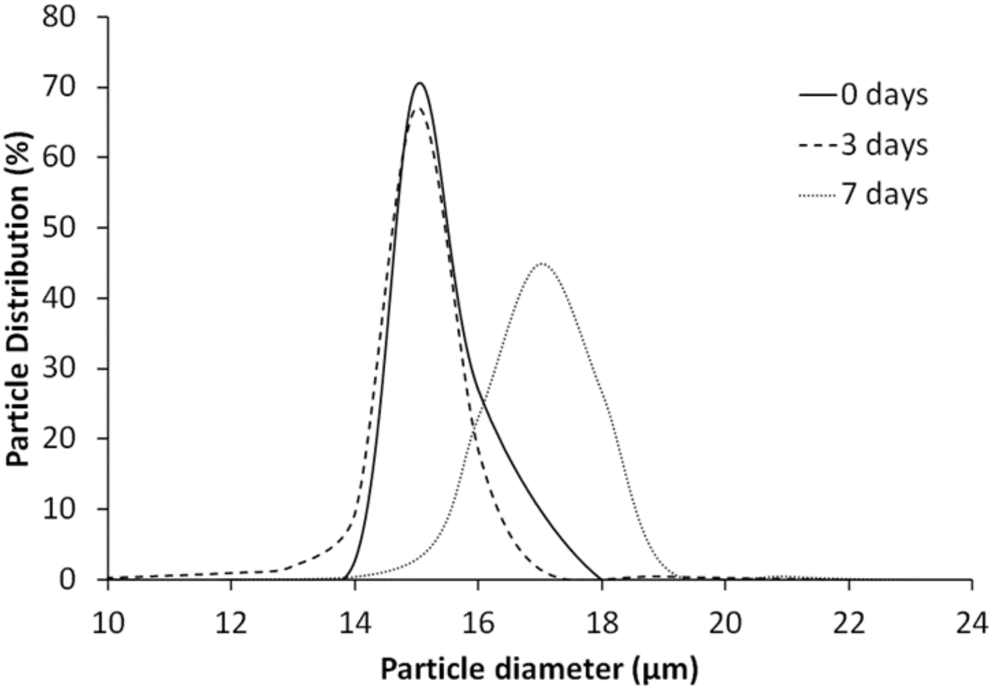

Figure 3.6. Particle size distribution of FLAP-PLGA during in vitro release for three data points at t = 0, 3, 7 days.

As seen in Table 3.2, the average microparticle diameter decreases slightly from 15.1 $\pm$ 0.6 μm to 15.0 $\pm$ 0.7 μm during degradation from 0 – 3 days. From 3-7 days, the average microparticle diameter increases to 17.0 $\pm$ 0.9 μm. The dispersity as determined by the CV, increases from 3.9 % to 4.7% after 3 days and to 5.3 % after 7 days. From this data, we can conclude that the microparticles are monodispersed up to 3 days, after which degradation causes polydispersity in particle diameter.

Table 3.2 Statistics of FLAP-PLGA during in vitro release from 0-7 days

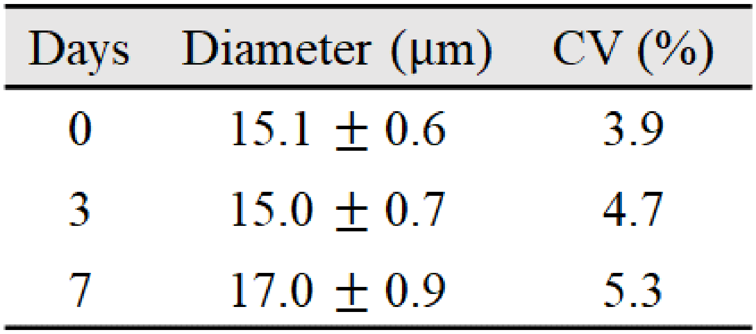

Days	Diameter (μm)	CV (%)
0	15.1 ± 0.6	3.9
3	15.0 ± 0.7	4.7
7	17.0 ± 0.9	5.3

In order to meet the local sustained release requirement for intra articular injection in the synovial joint, microparticles need to be retained locally in the joint. Although many factors impact the fate of these microparticles in vivo, one obvious factor is the synovial membrane pore diameter, ~ 20-90 nm for human knees.[132] Thus, microparticles throughput the 30-day duration shall at least exceed 90 nm to remain in the joint. In addition, microparticles below 10 μm could be subject to phagocytosis by macrophages, while microparticles above 100 μm could elicit an inflammatory or foreign body reactions forming foreign body giant cells.[133-134] Thus, PLGA particles shall fall in between 10-100 μm during the 30-day period. In fact, a PLGA microparticle therapy (ZILRETTA ® by Flexion) with encapsulated corticosteroid, triamcinolone acetonide (TA) met FDA approval for treatment of OA. These microparticles were in the size range of 20-100 μm in the synovial fluid for 12 weeks post injection.[135-136] This size range is consistent with our in vivo considerations discussed above. Since our PLGA particles remained intact and maintained at least 15.1 μm for at least 3 weeks, these particles are expected to remain inside synovial joint upon local delivery.

3.3.5 Bioactivity and Cytotoxicity Tests

The biological activity of FLAP was assessed using a luciferase assay[127]. During this assay, the presence of TNF-α activates luciferase expression driven by the NF-KB promoter, which in the presence of FLAP will be suppressed. As expected, maximum luciferase activity was detected in cells treated with TNF-α diluted in media only, or release medium from blank PLGA microparticles with no statistical difference as shown in Figure 3.7. In comparison, cells treated with released media from FLAP-PLGA demonstrate a dose-dependent inhibition of luciferase activity, with greater inhibition resulting when FLAP concentration increases from 30 to 300 nM. This result suggests that the biological activity of FLAP released from PLGA microparticles is retained in our deliver vehicles and approaches.

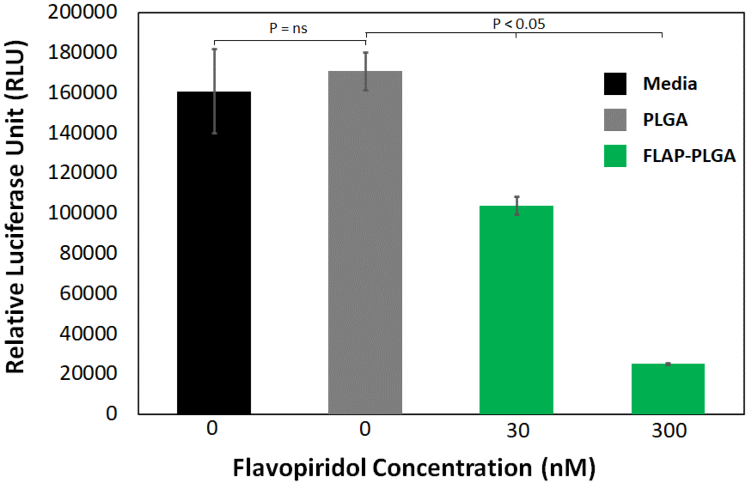

Figure 3.7 Bioactivity of released FLAP measured by luciferase assay. Released FLAP (FLAP-PLGA), and release medium from blank PLGA microparticles (PLGA) were assessed of their bioactivity through suppression of luciferase activity in HEK-Luc reporter cells stimulated with TNF-α (0.6 nM). Experiments were performed in triplicate (N=3)from one batch of particles, and results were reported as mean +/- SD. *Measurements were taken in conjunction with Dr. Jasper Yik and Dr. Dominik R. Haudenschild in the School of Medicine at University of California, Davis.*

As shown in figure 3.8, the cytotoxicity of released FLAP (300 nM) from PLGA microparticles on HEK cells was assessed using an LDH cytotoxicity kit. As a positive control, cells treated with lysis buffer showed the largest absorbance, indicating 100% cell death. As a negative control, cells treated with media only showed the lowest absorbance, where no or minimal cytotoxicity is expected. Moreover, results from cells treated with either free FLAP, released media from FLAP-PLGA or PLGA only, were statistically indistinguishable from the negative control.

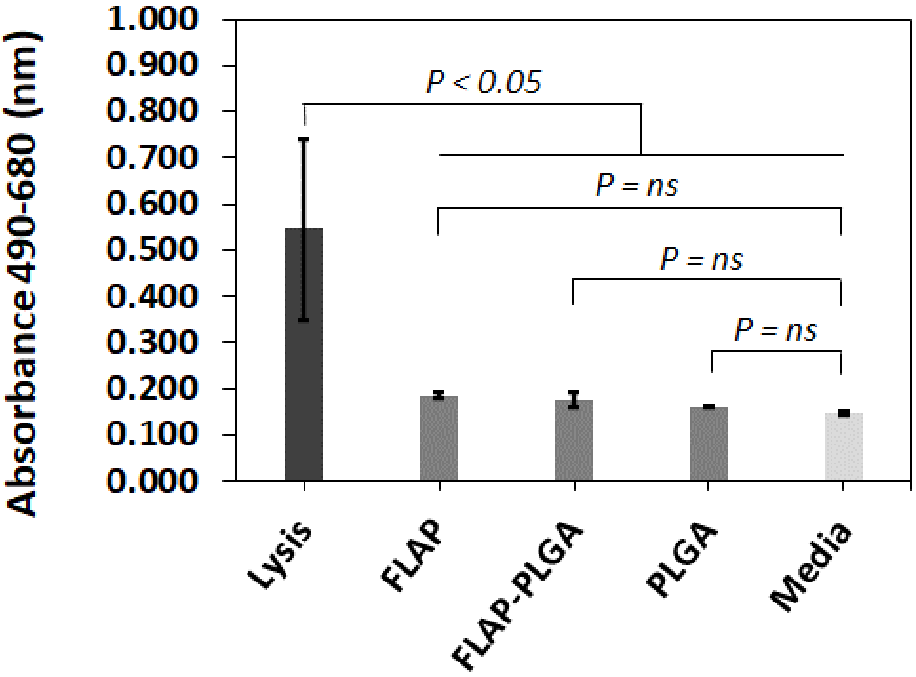

Figure 3.8 Assessment of cytotoxicity of Released FLAP from Encapsulated PLGA Microparticles. Sample treated with lysis buffer indicated maximum cell death. The media only group was the negative control, where cell death was minimum. Cytotoxicity of free FLAP (FLAP) was compared to that of the released FLAP (FLAP-PLGA) and blank PLGA (PLGA). Experiments were performed in triplicate measurements on one batch of particles (N=3) and results were reported as mean +/- SD. *Measurements were taken in conjunction with Dr. Jasper Yik and Dr. Dominik R. Haudenschild in the School of Medicine at University of California, Davis.*

3.3.6 GSK Greenness and sustainability metrics

The toxicity and the overall greenness were assessed by comparing the green solvent, DMC, used in this work, with that of DCM frequently used in PLGA microparticle synthesis in both emulsion and MFFD. First the toxicity of DMC and DCM is compared using previously reported values and summarized in Table 3.3. The median lethal dose for ingestion in a rat for DMC is 8.1X higher that for DCM.[52] This fact is important to consider for drug delivery applications, because if there were small amount of organic solvent remaining in the PLGA particles, serious health repercussions would occur. Additionally, for the personnel exposed to these solvents during manufacturing, handling DMC is significantly safer than DCM. The biodegradation rate for DMC is 28 days, which is 6.9X faster than that of DCM.[125, 137] This indicates that when organic solvent is released to the environment, the DMC vapors could have a lower environmental persistence than that of DCM vapors, whether it is in the water, air, or soil.

The GlaxoSmithKline (GSK) greenness metrics[129] provides another useful quantification to compare the greenness of using both solvent. The four categories used in the GSK green metric include waste (Wm), environment (Em), human health (HHm), and process safety (PSm) and their values were calculated using eq. (9)-(12) and summarized in Table 3.5. In all four categories, the DMC values are greater than that of DCM (see last column), indicating to what degree DMC is greener than that of DCM. The overall combined score was calculated using eq. (13), clearly indicating that DMC being 30% greater than DCM. Thus, DMC is intrinsically a much greener solvent and good candidate to replace DCM.

Table 3.3 Comparison of toxicity between DMC and DCM.

	Property	DMC	DCM	DMC/DCM
Toxicity Comparison	LD50 (Rat, Oral, mg/kg)	13,000	1,600	8.1
	Biodegradation Rate (%/28 days)	90	13	6.9
GSK Greenness	Wm	4.2	3.0	1.4
	Em	7.9	6.9	1.1
	HHm	7.7	5.3	1.4
	PSm	7.7	6.3	1.2
	Combined Score	6.7	5.1	1.3

We also calculated the E-factors,[128] specifically simple E-factor (sEF) and complete E-factor(cEF), to compare the sustainability using DMC versus DCM in production of PLGA microparticles using MFFD. In our synthesis of FLAP-PLGA particles, the values of each parameter required for sEF and cEF quantifications are summarized in Table 3.4. These values were utilized in E-Factor calculation described in the experimental section.

Table 3.4 Values of masses of reactants used in our synthesis that are pertaining to quantification of sEF and cEF.

Term (mg)	Description	DMC (15.1 μm)	DCM (15.9 μm)	DMC (32.4 μm)	DCM (31.9 μm)
m_{PLGA}	Mass of PLGA	10.00	10.00	40.00	40.00
$m_{FLAP,initial}$	Initial FLAP mass	0.12	0.12	0.36	0.36
m_{PVA}	Mass of PVA	600.00	800.00	600.00	800.00
$m_{particles}$	Mass of particles	9.27	9.37	37.59	35.49
$m_{org.solv.}$	Mass of organic solvent	1070.00	1330.00	1070.00	1330.00
m_{water}	Mass of water	6.00×10^4	8.00×10^4	6.00×10^4	8.00×10^4

Applying our actual experimental values in Table 3.4 for the PLGA particles to eq. (7) yielded sEF = 64.84 for DMC, almost 24% lower than that of DCM (85.43). The complete E-Factor cEF = 6,654.81 for DMC based on calculations using eq. (8), is also 24% lower than that of DCM

(8,762.30). These comparisons as shown in Table 3.5 indicate that using DMC as solvent for MFFD synthesis of PLGA particles presents a more sustainable route.

Table 3.5 E-factor calculation and comparison for production of PLGA particles using MFFD and DMC solvent versus that using DCM as organic solvent.

Parameter	DMC	DCM	DMC/DCM
sEF	64.84	85.43	0.76
cEF	6654.82	8762.30	0.76

3.4 Conclusions

Current means for synthesizing PLGA microparticles, using either conventional emulsion or MFFD, frequently employ DCM as the solvent in organic phase. Due to DCM's health and environmental toxicity and slow degradation, a green solvent, DMC, is introduced to replace DCM. Using production of FLAP encapsulated PLGA microparticles as an example, this work demonstrates that the use of green solvent does not hinder the synthesis procedure or quality of products. In fact, the use of DMC preserves the narrower size distribution leading to high reproducibility in particle size and drug load. In addition, the particles produced exhibited drug release profiles more desirable for local sustained release into joint for future applications of osteoarthritis treatment. Further, cytotoxicity and biological activity tests demonstrated high biocompatibility and efficacy, respectively. DMC was shown to be a much greener solvent than DCM with approximately one order of magnitude higher LD50 values in rat, 5-fold degradation rate. Additional measures include a 30% higher GlaxoSmithKline (GSK) combined greenness value. In the context of PLGA particle production process, the simple E-Factor (sEF) and complete E-Factor(cEF) of DMC are only a fraction of that of DCM, i.e., 76% and 76%, respectively, which indicates greater sustainability. The approach reported in this work shall also provide a new and green means for production of polymer-based microparticles for local sustained delivery of FLAP for the treatment of osteoarthritis and cancers, and for drug delivery in general.

CHAPTER IV

New Insight into Drug Release Profiles of Flavopiridol Loaded Poly(lactic-co-glycolic acid) Microparticles

4.1 Introduction

Poly(lactic-co-glycolic acid) (PLGA) microparticles are among the most well-known and frequently used drug delivery vehicles because of their low cost, high biocompatibility, and FDA approval.[31, 35, 138-140] Key in vitro tests prior to animal and clinical applications require that the drug release profile meets clinical needs, e.g., fast and short-term release, or local sustained release over desired period. Therefore, many iterations have to take place to optimize the formulation, to reach the desired particle size and drug loading, as well as the required release kinetics.[140-142] To reduce these iterations and shorten the research and development (R&D) time, insights into the mechanism of drug release at molecular level are essential.[143-144] The frequently practiced initial efforts to gain these insights include, measuring the drug release profile, applying currently known kinetics model(s), and non-linear least square fitting to attain the kinetics parameters, which allows glimpsing into molecular level mechanisms.[33, 56-57, 126, 145]

In vitro release profiles are typically measured experimentally by $\frac{M_t}{M_\infty}$ versus time (t), where M_t is the cumulative amount of drug released at time t, and M_∞ is the cumulative amount of drug released at saturation release point (aka, at infinite time).[146] The currently adopted kinetic model utilized to account for the measured drug release kinetics is shown in eq. (4.1)

$$\frac{M_t}{M_\infty} = \theta_b(1 - \exp(-k_b t)) + \theta_r \left(\frac{\exp(k_r(t - t_{max}))}{1 + \exp(k_r(t - t_{max}))} \right) + \theta_d \left(1 - \frac{6}{\pi^2} \sum_{n=1}^{\infty} \frac{1}{n^2} \exp\left(-\frac{\pi^2 n^2 D_e t}{r_p^2} \right) \right) \qquad (1)$$

The first term represents the process of “burst release”,[62, 147] with k_b as the burst constant and θ_b as the contribution of burst release. Burst release typically occurs rapidly during the initial release. The 2nd term describes degradation release, where the whole analytical expression was derived from Prout-Thompkins model,[148-149] with θ_r as the contribution of degradation release, k_r as the degradation-relaxation rate constant, and t_{max} as the time required to achieve 50% of cumulative drug release. The 3rd term represents diffusion of drug molecules from PLGA microparticles. The expression is an analytical solution to Fick’s second law of diffusion assuming spherical PLGA particle geometry,[56, 150-151] where D_e is the effective diffusion coefficient, r_p is the mean microparticle radius, and θ_d is the contribution of diffusion release.

The present work includes production and characterization of four series of PLGA microparticles loaded with flavopiridol (FLAP). FLAP is a known Cyclin-dependent kinase 9 (Cdk9) inhibitor being evaluated for the treatment of post traumatic osteoarthritis (PTOA)[65, 152-153] and cancer.[154-155] Our prior investigations indicated that local sustained release of FLAP into the joint capsules provided a new and effective means for reducing PTOA severity.[40, 153, 156] The attempts to apply current kinetics model, e.g., eq (4.1) to our measured FLAP release profiles clearly reveal model limitations. Aided by using high-resolution imaging tools: scanning electron microscopy (SEM) to monitor structural evolution during release, and atomic force microscopy (AFM) imaging to reveal intra-particular structures, this work provided modifications to the current kinetics model. As such, new insights into drug release processes were revealed. This approach can be easily adopted by researchers in the drug formulation and delivery fields, to facilitate R&D efforts and accelerate understanding of drug release.

4.2 Experimental Methods

4.2.1 Materials

Flavopiridol (FLAP) was purchased from Cayman Chemical Company (Ann Arbor, MI). PLGA (PURASORB PDLG 5004A 50:50 DL-lactide:glycolide) was purchased from Corbion (Amsterdam, Netherlands). Tween-20, dichloromethane (DCM), dimethyl carbonate (DMC), poly(vinyl alcohol) (PVA-99) (98-99% hydrolyzed, MW 30000 – 40000), poly(vinyl alcohol) (PVA-80) (80% hydrolyzed, MW 9000-10000), dimethyl sulfoxide (DMSO) (≥ 99.7%) were all purchased from Sigma Aldrich (St. Louis, MO). Phosphate-buffered saline (PBS) (1X) was purchased from Mediatech (Manassas, VA). Ultrapure water with a resistivity of 18.2 MΩ·cm was generated using a Millipore Milli-Q system (EMD Millipore, Billerica, MA). Two-component epoxy (S-31) was purchased from ITW performance polymers (Riviera Beach, FL). AFM cantilevers (AC 240) were purchased from Olympus America (Center Valley, PA). Liquid nitrogen was purchased from Airgas, Inc. (Radnor, PA). Gaseous nitrogen was purchased from Praxair, Inc. (Danbury, CT). Glass scintillation vials (20 mL) and glass coverslips (22 x 22 mm^2) were purchased from Fisher Scientific (Hampton, NH). Poly(tetrafluoroethylene) (PTFE) tubing was purchased from Cole-Parmer (Vernon Hills, IL, USA).

4.2.2 Synthesis of FLAP-Loaded PLGA microparticles

As described in our prior publication,[156] monodisperse PLGA microparticles containing flavopiridol were synthesized via microfluidic flow-focusing. The microfluidic flow focusing device was designed (AutoCAD, 2018) and fabricated by μFludix (Toronto, Canada) using a poly(dimethyl siloxane) (PDMS) soft lithography technique.[90] The device was rendered hydrophilic by aqueous 1% (w/v) PVA-99 treatment as described previously.[157] FLAP loaded PLGA microparticles were generated using procedures described elsewhere.[156, 158] The aqueous phase in the synthesis was aqueous 1% (w/v) PVA-80 and the organic phase was FLAP/PLGA dissolved in either DCM or DMC. The organic and aqueous phases were pumped through the inlet PTFE tubing of microfluidic device via syringe pump (New Era Pump Systems Inc., Farmingdale NY, USA) at flow rates, Q_{org} and Q_{aq}, respectively. The organic droplets were formed at the flow focusing orifice where the two fluids met, as visualized *in-situ*, using an inverted microscope (Olympus Corp., Tokyo, Japan) equipped with a high-speed camera (Photron AX-100, Photron USA Inc., San Diego, CA). The organic droplets were carried by the aqueous phase into the outlet PTFE tubing immersed in a round bottom flask with 5 mL of 1% (w/v) PVA-80. Immediately following synthesis, the flask was mounted on a rotary evaporator (Buchi R300, Buchi Corp, New Castle, DE) and the organic solvent was removed (40 mbar, 40 °C, 5 min). The remaining FLAP/PLGA particles were collected via centrifugation at 2500 rpm (Champion F-33D, Ample Scientific, Norcross, GA) and subsequently washed with Milli-Q water. This was repeated 2X to remove unbound PVA-80. The washed particles were kept in 1-2 mL of Milli-Q water, and quickly frozen in liquid nitrogen, and lyophilized (Labconco Corp., Kansas City, MO, USA) to dryness overnight. For this investigation, four types of FLAP loaded PLGA microparticles, referred to as PLGA-1 through PLGA-4, were synthesized at conditions summarized in Table 4.1, where Q_{org} is the organic phase flow rate and Q_{aq} is the aqueous phase flow rate.

Table 4.1. Synthesis conditions and resulting products of four types of FLAP-Loaded PLGA Microparticles.

Sample name	Organic Solvent	[PLGA] (mg/mL)	Q_{org} (mL/hr)	Q_{aq} (mL/hr)	Diameter (μm)	CV (%)	LC (%)	EE (%)
PLGA-1	DCM	10	0.1	8	15.9 ± 0.6	3.8	1.15 ± 0.06	63.0 ± 0.5
PLGA-2	DCM	40	0.1	8	31.9 ± 0.9	2.8	2.35 ± 0.09	78.3 ± 1.0
PLGA-3	DMC	10	0.1	6	15.1 ± 0.6	3.9	0.65 ± 0.12	55 .0± 3.0
PLGA-4	DMC	40	0.1	6	32.4 ± 1.0	3.1	0.58 ± 0.02	65.2 ± 0.1

4.2.3 Drug loading and Encapsulation Efficiency of FLAP loaded PLGA microparticles.

Following established procedures[156, 158] the loading capacity (LC) of PLGA-1 to PLGA-4 were determined and summarized (Table 5.1, column 8). Briefly, 1 mg of PLGA particles (m_p) was dissolved in DMSO to a concentration of 1 mg/ml. The absorption spectrum was determined using UV-Vis spectroscopy (Denovix, Inc., Wilmington, DE) where the absorbance at 380 nm was measured and compared to known set of standards, ranging from 1-100 μM. Applying Beer's law yielded the concentration of FLAP, which is converted to FLAP mass (m_{FLAP}). The LC was then quantified using eq. (2) and is seen in Table 5.1.

$$\mathrm{LC} = \left(\frac{\mathrm{m_{FLAP}}}{\mathrm{m_p}}\right) \times 100\% \qquad (2)$$

The encapsulation efficiency(EE) was determined using eq. (3) by dividing LC with the initial loading of FLAP in the syringe (LC_{initial}).

$$\mathrm{EE} = \frac{\mathrm{LC}}{\mathrm{LC_{initial}}} \text{ x } 100\% \qquad (3)$$

4.2.4 In vitro release profile of FLAP from the FLAP-loaded PLGA microparticles

In vitro release experiments were performed to determine FLAP release from the four types of PLGA particles using previously described methods.[156, 158] Briefly, 4 mg of FLAP loaded PLGA microparticles were dispersed in 0.5 mL of 1X PBS/0.2% Tween-20 aqueous solution at 37 °C. At designated time during release, the supernatant was collected via centrifugation at 4000 rpm for 5 min and the absorbance spectrum of FLAP was measured using UV-Vis spectroscopy at 274 nm. Comparing against a known set of standards from 3 – 100 μM with extinction coefficient, 22,478 $M^{-1}cm^{-1}$, the concentration of FLAP was determined using Beer's Law. Following measurement, 0.5 mL of fresh release medium was added to disperse the particles until the next time point. The cumulative release percentage of FLAP in the in vitro release profile was calculated using eq. (4) by adding the mass of FLAP released at the time point ($\sum_{t=0}^{t_f} m_t$) and dividing by the total mass of FLAP encapsulated (m_{FLAP}).

$$Cumulative\ Release\ (\%) = \frac{\sum_{(t=0)}^{t_f} m_t}{m_{FLAP}} \text{ x } 100\% \tag{4}$$

4.2.5 Time-lapse Scanning Electron Microscopy Imaging

Using previously reported methods,[156] the particle size and morphology was determined using scanning electron microscopy (SEM) imaging (S-4100T, Hitachi High Technologies America, Inc., Pleasanton, CA). Time dependent measurements were performed on the particles that underwent release at certain time points, and this was accomplished using a twin sample during release, which was only used for structural investigation of the particles. Briefly, the microparticle suspension was centrifuged to a pellet and the supernatant was removed, leaving a pellet of particles in a minimum volume. 5-10 μL of the suspension was drop dried on a plasma cleaned (Harick Plasma Inc., Ithaca, NY) silicon wafer substrate in a laminar flow hood (Cleatech, Orange, CA). Following drying, the substrate was tilted at 10° above the surface, and 30 μL of pure water was dropped from the top corner and allowed to flow over the particles to rinse repeatedly, followed by drying in clean ambient environment. The dried substrate was fixed to an Al-stub using double-sided carbon tape, then transferred to a vacuum chamber to be coated with 10 nm of gold via sputtering coating (Ted Pella Inc., Redding, CA). The metal-coated samples were transferred to the SEM for imaging. At the acceleration voltage and emission current of 2 kV at 10 μA, respectively, the SEM images were acquired. The resulting SEM images were processed using Image J (National Institutes of Health, Bethesda, MD), from which the mean diameter and dispersity of the particles were determined (Table I, columns 6-7). The dispersity of the particles was quantified using the coefficient of variation (CV) via eq. (5) where the standard deviation (σ) is divided by the mean diameter ($\bar{\mathrm{d}}$) of at least 100 particles.

$$\mathrm{CV} = \left(\frac{\sigma}{\bar{\mathrm{d}}}\right) \times 100\% \tag{5}$$

4.2.6 Atomic Force Microscopy Imaging

Atomic force microscopy (AFM) characterization was performed using an MFP-3D AFM (Oxford Instrument, Santa Barbara, CA). All images were acquired using a microfabricated cantilever (AC 240, k = 0.6 N/m, Olympus America, Center Valley, PA). 1 mg of PLGA microparticles were embedded in 5-min epoxy on a precleaned glass slide. The pre-cleaning was carried out using a plasma cleaner at 1 minute with high radiofrequency. After air drying for 24 hours in the laminar flow hood, the particles were cut by de-capping using a #22 scalpel blade (Fisher Scientific, Hampton, NH). All images were acquired in air using tapping mode over a 50 x 50 μm^2 scan area. The driving frequency of the cantilever was set at its resonant frequency of 73.2 kHz. Free amplitude of the cantilever was set at 1000 mV with a set point of 35% damping. Acquisition of data was completed using the vendor's software developed using an Igor Pro 6.12 platform.

4.3 Results and Discussion

4.3.1 Insights into FLAP-PLGA microparticle drug release profiles using current kinetics model

The in vitro release profile of PLGA-1 is shown in Figure 1 (blue dots). A non-linear least-squares fitting of the release profile in Figure 4.1 was generated using the existing kinetics model, eq. (1), and the result is shown as a solid black line. The fitting was performed using a nonlinear least squares algorithm in MATLAB (Math Works, Natick, MA).

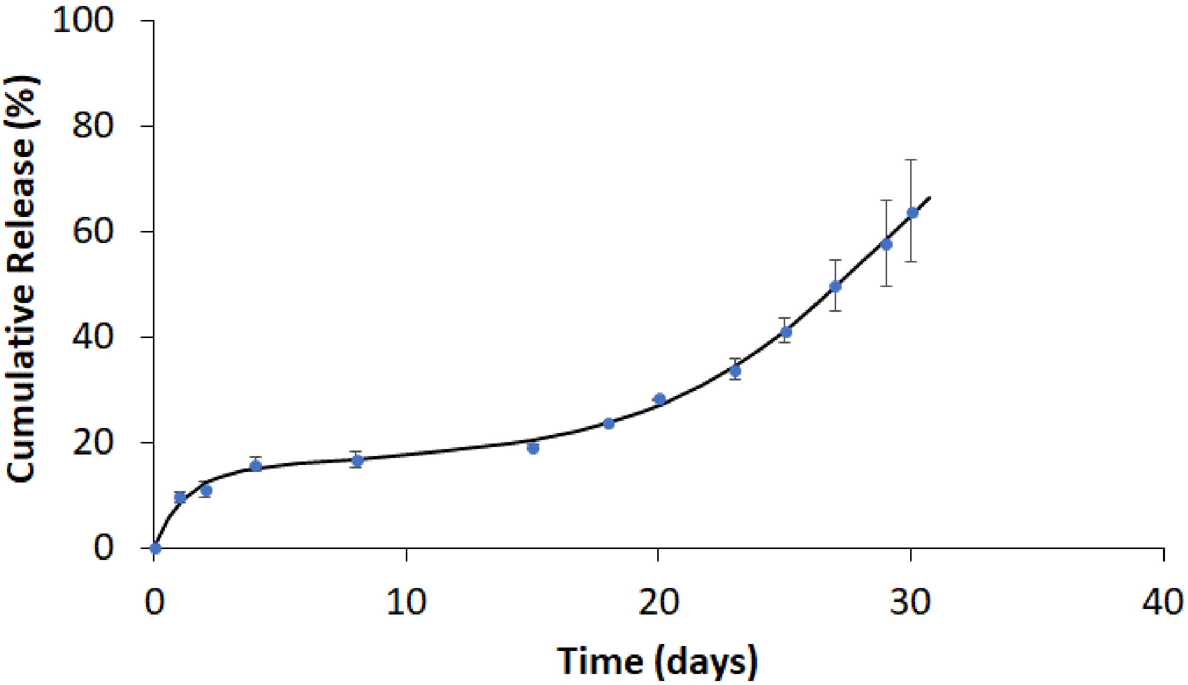

Figure 4.1. Drug release profile of PLGA-1 (blue dots). At each time point of measurement, the result was expressed as mean ± SD from $n = 3$ independent sets of microparticles. Nonlinear least-squares fitting of the release profile using eq. (1) was shown as a solid black line.

From a mathematical perspective, the fit is excellent as demonstrated by the high coefficient of determination, R^2=0.9982; and a low root mean squared error, RMSE = 1.507. The coefficient of determination is frequently used as an evaluation of model performance, but not sufficient for model comparison when non-linear regression is involved.[159] RMSE or the standard error of regression is a measure of the average distance observed values fall from the regression line and can be used to determine a confidence interval. These parameters, summarized in Table 4.2, column 4, allow for evaluation of fitting quality, and for the comparison between models, with a preference towards lower RMSE values.[160-161] While the burst release contribution (θ_b), and degradation-relaxation contribution (θ_r) were obtained from fitting, the diffusion contribution (θ_d) was calculated by $\theta_d = 1 - \theta_b - \theta_r$ to obey boundary conditions.

Quantitatively, the contribution of burst release, $\theta_b = 12\%$, and the burst constant, $k_b = 0.85$ days^{-1} were obtained. Based on the current kinetics model, θ_b and k_b were kept constant throughout the 30 days (Figure 4.1). These outcomes are not consistent with known burst release mechanisms, as burst release typically occurred in the initial period of drug release, e.g., the first five days or shorter, then significantly decreased or diminished.[62, 147, 158] In the case of our PLGA-1, the release profile appeared to have 3 regions of slopes, including a short sharp release during the first 4 days, which is likely due to burst release behavior. This burst release clearly did not continue for 30-days.

Table 4.2. Kinetics parameters extracted from the non-linear least-square fitting of the drug release profile of PLGA-1 shown in Figure 1, using eq. (1).

Parameters	Definition	Unit	Results
k_b	Burst constant	days^{-1}	0.85
θ_b	Burst release fraction	-	0.12
k_r	Degradation constant	days^{-1}	0.23
t_{max}	Time to achieve 50% release	days	28.94
θ_r	Degradation release fraction	-	0.79
D_e	Diffusion Coefficient	$\frac{cm^2}{s}$	9.15E-14
r_p	Radius of particle	cm	0.00159
θ_d	Diffusion release fraction	-	0.09
R^2	Coefficient of determination	-	0.9982
RMSE	Root Mean Squared Error	-	1.507

Other kinetics parameters include the contribution of degradation release, $\theta_r = 79\%$ with rate constant, $k_r = 0.23$ days^{-1}. Based on the current kinetics model, both θ_r and k_r remained constant throughout the entire 30-day release process. These outcomes are not consistent with known degradation release behavior of PLGA microparticles. It has been reported that degradation release from PLGA microparticles was not a constant event, typically slow in the beginning and accelerated when degradation was approaching the core of the particles.[162-164] Collectively, although the release model mathematically fits the release profiles of PLGA particles, the physical insight extracted from this practice would need improvement to better reconcile with the known release mechanism. Therefore, modification to the kinetics model would be necessary to better reconcile the actual release mechanism in general and the release of PLGA-1 in specific. A new method needs to be developed to address this limitation.

4.3.2 Modified kinetics model to account for PLGA microparticle drug release profile and mechanism

A direct means to address the limitations (see section above) of the current kinetics model is to use a piecewise function to account for the initial short burst release, and the late-stage degradation release. Piecewise functions have been used before in the fitting of drug release profiles from PLA filaments. In that case[165], the time region was decided, based on the measured drug release profile, without a separate, independent verification. In order to better account for our release profiles, for spherical and near spherical particles, a new piecewise set of equations needs to be derived. As shown in eq. (6), a new kinetics model, as a simple modification of eq. (1), is generated to clearly reveal the two different time regions in flavopiridol release. The first time region ($t \leq t_1$ days) only incorporates the 1st and the 3rd term of eq. (1), since burst release is known to occur during the initial period of release, while diffusion occurs throughout the duration of release.[56, 62, 145, 148] Beyond t_1, $t \geq t_1$ days, only the 2nd and 3rd term of eq. (1) were used, to quantify the degradation and diffusion processes.

$$\frac{M_t}{M_\infty}=\begin{cases}\theta_b(1-\exp(-k_b t))+\theta_d\left(1-\frac{6}{\pi^2}\sum_{n=1}^{\infty}\frac{1}{n^2}\exp\left(-\frac{\pi^2 n^2 D_e t}{r_p^2}\right)\right) & t\leq t_l\\ \theta_d\left(1-\frac{6}{\pi^2}\sum_{n=1}^{\infty}\frac{1}{n^2}\exp\left(-\frac{\pi^2 n^2 D_e t}{r_p^2}\right)\right)+\theta_r\left(\frac{\exp\left(k_r(t-t_{max})\right)}{1+\exp\left(k_r(t-t_{max})\right)}\right) & t\geq t_l\end{cases} \qquad (6)$$

These models fit the experimental data well, but the fitting occurs over the entirety of release. By utilizing the new kinetics model, the piecewise function allows release terms like burst release to be limited to the beginning of release.

In order to determine the time regions defined in eq. (6), high-resolution SEM imaging was performed by visualizing the particles at designed time during release. Some of the snapshots at important junctures of release processes are shown in Figure 4.2. At t = 0 days, SEM reveals a smooth and spherical morphology for all microparticles. Only small number of dimples per particle (1) were present at the outermost surface, whose diameter range from 0.3 – 1.1 µm. At t = 3 days, dimples appeared in larger numbers (3) per particle and diameters ranging from 0.3 – 3.4 µm. This trend is consistent with the mechanism of burst release.[158] At t = 7 days, the dimples increased in size ranging from 1.0 – 5.6 µm indicating the beginning of erosion involving PLGA degradation.[166-167] By t = 21 days, the craters evolved into merged heterogenous openings with obvious erosion along the peripheral of the particles. By t = 30 days, fragmentation occurred resulting in observed polydisperse fragments. These time-dependent SEM studies enabled determination of the time when erosion occurred and monitoring of the morphological changes due to degradation. In the case of PLGA-1, t_l = 8 days, from careful SEM investigation. The structural evolution revealed by our SEM investigations are also consistent with PLGA chemistry. The labile esters bonds of the PLGA polymer are cleaved via hydrolysis from the aqueous medium, effectively forming oligomers of varying molecular weight within the particle.[58, 138, 144] The creation of oligomers promotes water penetration and relaxation which ultimately leads a more porous network for faster drug release.[167]

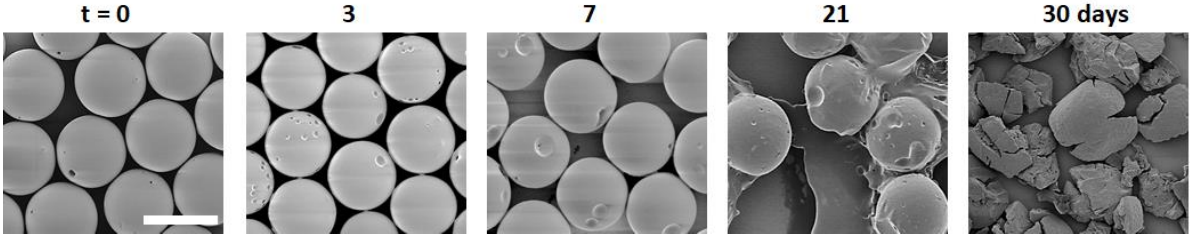

Figure 4.2. SEM image of PLGA-1 microparticles, taken at designated time (atop of the images) during in vitro release measurements. Scale bar = 20 µm.

A non-linear least square fitting of the measured release profile of the PLGA-1 particles using eq. (6) was performed (Figure 4.3). Mathematically, the fitting works well, with R^2 = 0.9644 and RMSE = 1.456, for t = 0-8 days. Beyond 8 days, the fitting works even better, with R^2 = 0.9904 with a low RMSE = 1.940. Both of these fitting statistics are summarized at the bottom of Table 4.3, columns 4-5.

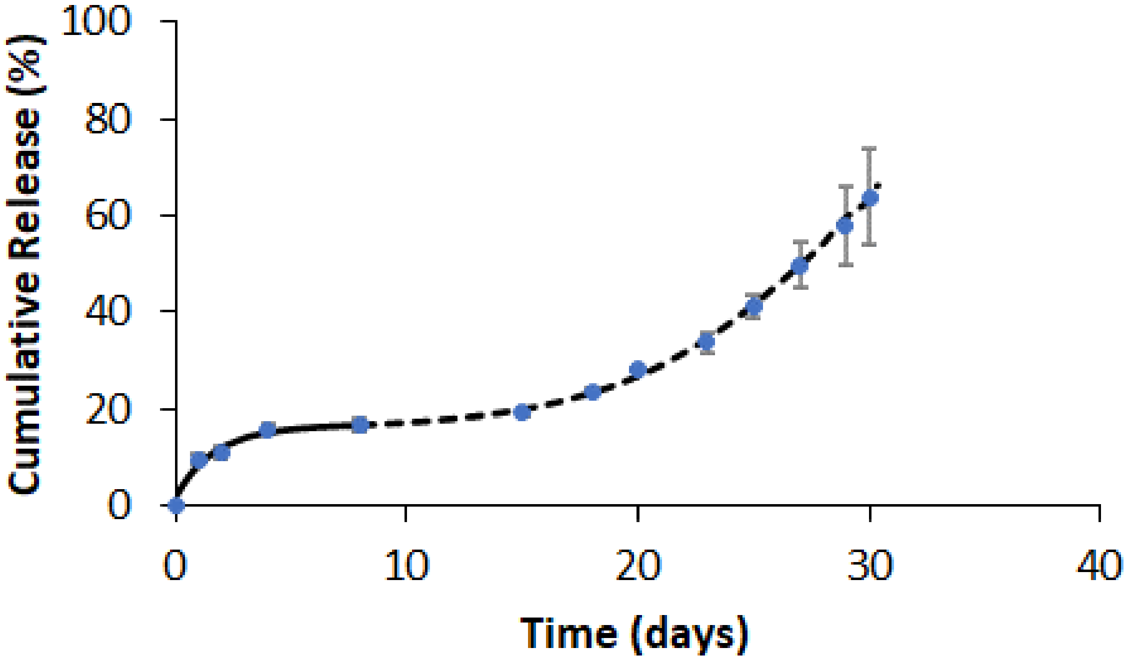

Figure 4.3. Drug release profile of PLGA-1 (blue dots). In each time point of measurement, the result is expressed as mean ± SD from n = 3 independent batches of PLGA microparticles. Nonlinear least-square fitting of the release profile using eq. (6) is shown as the solid black line for 0-8 days and dashed black line for 8-30 days.

Table 4.3. Kinetics parameters extracted from non-linear least-square fitting of the drug release profiles of all four types of PLGA particles listed in Table 4.1, using eq. (6) for PLGA-1 and PLGA-2, and eq. (7) for PLGA-3 and PLGA-4, respectively.

Parameters	Definition	Unit	PLGA-1		PLGA-2		PLGA-3		PLGA-4	
			0-8 days	8-30 days	0-6 days	6-32 days	0-6 days	6-31 days	0-6 days	6-31 days
k_b	Burst constant	days^{-1}	0.62	-	0.06	-	0.12	-	0.05	-
θ_b	Burst release fraction	-	0.14	-	0.14	-	0.19	-	0.49	-
k_r	Degradation constant	days^{-1}	-	0.28	-	0.39	-	0.17	-	0.14
t_{max}	Time to achieve 50% release	days	-	29.03	-	24.35	-	22.32	-	16.01
θ_r	Degradation release fraction	-	-	0.68	-	0.76	-	0.91	-	0.91
D_e	Diffusion Coefficient	$\frac{\mathrm{cm}^2}{\mathrm{s}}$	2.62E-16	1.10E-13	6.20E-16	2.69E-13	7.46E-16	1.40E-12	2.56E-15	8.850E-12
r_p	Radius of particle	cm	0.00159	0.00159	0.00319	0.00319	0.00151	Disk	0.00324	Disk
l	Thickness of film	cm	Sphere	Sphere	Sphere	Sphere	Sphere	0.0004	Sphere	0.0002
θ_d	Diffusion release fraction	-	0.86	0.32	0.86	0.24	0.81	0.09	0.51	0.09
R^2	Coefficient of determination	-	0.9644	0.9904	0.8826	0.9967	0.9690	0.9988	0.8679	0.9945
RMSE	Root Mean Squared Error	%	1.456	1.940	1.824	2.265	0.9822	1.156	2.899	2.145

Based on the result of the fitting and applying the boundary conditions of $\theta_b + \theta_d = 1$, during t = 0-8 days, the burst release was, θ_b = 14%, with burst constant, k_b = 0.62 days^{-1}, and burst release diminished beyond 8-days. This description is more consistent with the known burst release behavior of drug-loaded PLGA microparticles.[62] The contribution of diffusion release was, θ_d = 86% with effective diffusion coefficient, D_e = 2.62 x 10^{-16} cm^2/s. These results suggest diffusion release is quite slow, which is consistent with the slower diffusion through a dense polymer network.[167] These kinetics parameters are summarized in Table 4.3, column 4.

Beyond 8 days, the contribution of diffusion release was, θ_d = 32%, while the effective diffusion coefficient was, D_e = 1.10 x 10^{-13} cm^2/s. In comparison to t = 0-8 days, the diffusion coefficient increased, while the contribution of diffusion decreased. These trends are consistent with the creation of a more porous PLGA polymer network, allowing greater water penetration for drug dissolution and release..[56, 166, 168] Applying the boundary conditions of $\theta_d + \theta_r = 1$, we attained the contribution by degradation. The contribution of degradation release was, θ_r = 68% and with degradation constant, $k_r = 0.28\ \text{days}^{-1}$. These results suggest degradation release is dominant during this second region, because erosion of the particles exposes hidden pockets of drugs which are now easily assessable for release.[162, 164, 167] These kinetics parameters are summarized in Table 4.3, column 5.

4.3.3 New insight into drug release profiles of FLAP-PLGA microparticles via modified kinetics models

To demonstrate the robustness of the new approach described in eq. (6), particles twice the size (PLGA-2) were shown in table 4.1, row 2. Similarly, to the analysis described previously, time dependent SEM imaging was used to monitor particle morphology and geometry of PLGA-2 during release as shown in Figure 4.4.

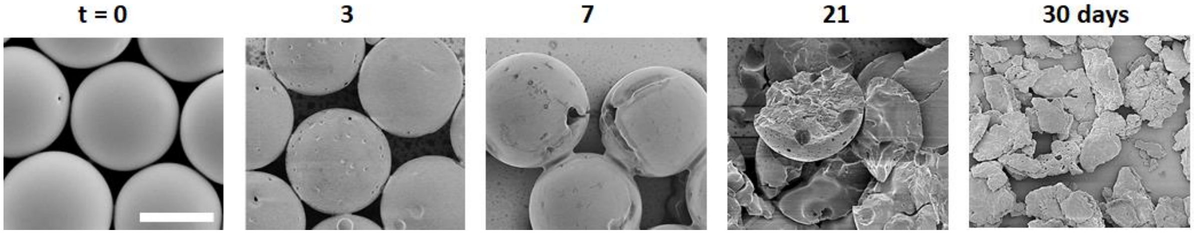

Figure 4.4. SEM imaging of the PLGA-2 particles, taken at designated time points (see on top of the images) during in vitro release measurements. Scale bar = 20 μm, for all images.

It can be seen at t = 0 days, that the particle morphology was smooth with spherical geometry and less than 1 dimple per particle. At t = 3 days, SEM revealed the sporadic appearance of dimples with ~ 8 dimples per particle, ranging in size from 0.6 – 4.9 µm. This sporadic appearance of dimples was similarly seen in PLGA-1 which indicated the aftermath of burst release. By t = 7 days, the dimples evolved into craters with non-spherical openings and in addition, large gashes with sizes, 5.3 – 19.9 µm, on the particle surface were visualized. The evolved particle surface features were similarly seen in PLGA-1 which indicated the start of degradation mechanism. By

21 days, all particles had cracked into 2-4 pieces, revealing a solid core, with exposed cavities near the peripheral. At t = 30 days, the particles were visualized as polydisperse fragments, similarly seen in PLGA-1. Because of the similarities in the particle structural evolution with PLGA-1. the time region for burst release was identified to be 0 – 6 days and the second region was 6 – 32 days. The time regions identified from Figure 4.4, were utilized in eq. (6), and applied on the measured release kinetics of the PLGA-2 particles through non-linear fitting as seen in Figure 4.5. The burst release region fitting, 0-6 days, was visualized as a solid black line. The model fits mathematically well to the release profile with $R^2 = 0.8826$ and RMSE = 1.824. The second region was plotted as a dashed black line and also fits even better to the release profile with $R^2 = 0.9987$ and RMSE = 2.265. Both of these fitting statistics are seen at the bottom of Table 4.3, columns 6-7.

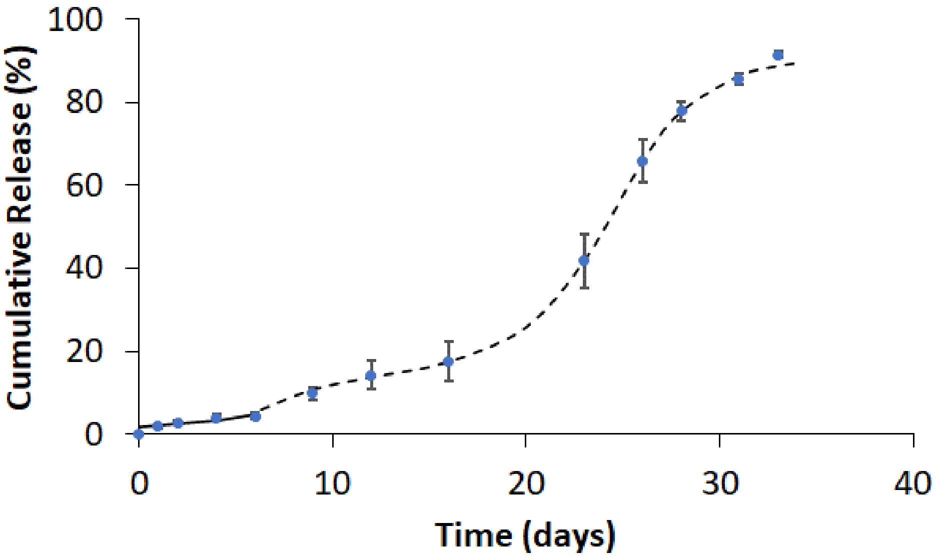

Figure 4.5. Drug release profile of PLGA-2 (blue dots). In each time point of measurement, the result is expressed as mean ± SD from *n* = 3 independent batches of PLGA microparticles. Nonlinear least-square fitting of the release profile using eq. (6) is shown as the solid black line for 0-6 days and dashed black line for 6-30 days.

During t = 0-6 days, quantitatively, burst release was θ_b = 14% with burst constant k_b= 0.06 $days^{-1}$. The burst release contribution was similar to the PLGA-1 particles, however the burst constant decreases 11-fold which was consistent with what has been reported elsewhere[61]. The contribution of diffusion release with θ_d = 86% and effective diffusion coefficient D_e = 6.20 x 10^{-16} cm^2/s was similar to those in PLGA-1, but the diffusion coefficient was 2.4-fold greater. An increase in particle size has been reported to be directly proportional to the magnitude of D_e, where larger particles have larger diffusion coefficients.[56] These kinetics parameters were summarized in Table 4.3, column 6.

Beyond 6 days the contribution of diffusion release was θ_d = 24% with the effective diffusion coefficient $D_e =$ 2.69 x 10^{-13} cm^2/s. The diffusion coefficient D_e increased over 400-fold past 6 days which was similarly observed and described with PLGA-1. The contribution of degradation release was θ_r = 76% and with degradation constant k_r = 0.39 $days^{-1}$. The degradation constant k_r was larger for PLGA-2, which was similarly reported for increasing particle size.[61] The greater θ_r for PLGA-2 is verified with earlier particle cracking observed in Figure 4.4, which resulted in sharper release. These kinetic parameters were summarized in Table 4.3, column 7. Utilizing this new model on larger particles demonstrated robustness when comparing against PLGA-1.

The generic applicability of the new approach was tested by utilizing particles fabricated with vastly different synthesis conditions, namely the use of DMC as the organic solvent. These particles, PLGA-3 and PLGA-4 are seen in Table 4.1, columns 3-4. The use of the organic solvent during synthesis has been shown to affect the morphology of the particles during in vitro release[50, 156], therefore particle morphology and geometry was assessed during release to guide in the model development.

Time dependent SEM imaging as seen in Figure 4.6 was used to monitor particle morphology from PLGA-3 (top row) and PLGA-4 (bottom row) particles.

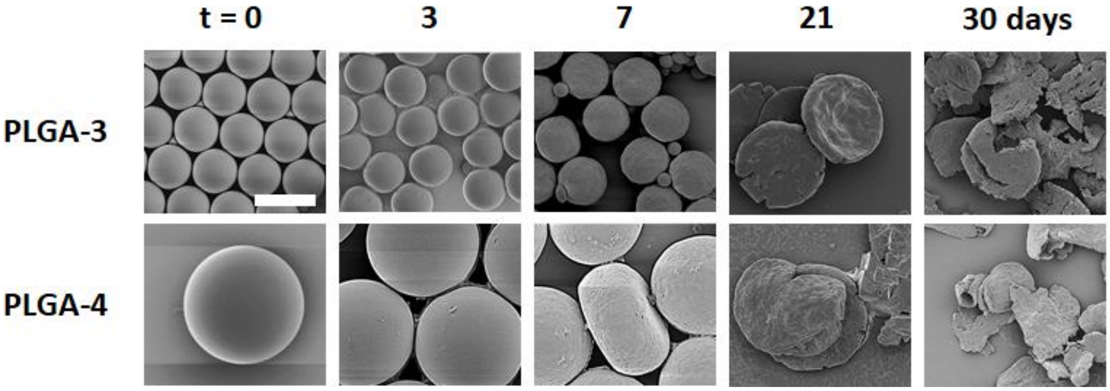

Figure 4.6. SEM imaging of PLGA-3 and PLGA-4particles taken at designated time points (see atop of images) during in vitro release measurements. Scale bar = 20 μm, for all images.

For PLGA-4 particles, it can be seen at t=0 days, there was a smooth and spherical morphology. At t=3 days, all of the particle's present small grooves and about 1 dimple per particle located on the exterior. In comparison to PLGA-2 particles, the presence of surface features like dimples was similar, which indicates the aftermath of burst release. At t=7 days, the particle surface roughness increased, which was consistent with degradation[169] and 1 out of 7 particles presented some deflation. The increase in surface roughness was similarly observed in PLGA-2, however the deflation of the particle was unique. At t = 21 days, all of the particle's geometry evolved into a "pancake" geometry with erosion along the peripheral. In comparison to structural evolution of PLGA-2, this "pancake" geometry was not observed in PLGA-2, however this geometrical change has been observed previously when DMC is used as the organic solvent[156, 170]. By t = 30 days, the particles have flattened in a higher degree with a film-like geometry, and some were degraded into polydisperse fragments. This polydisperse fragmentation was similarly observed in PLGA-4.

The flattening of PLGA microparticles has been previously reported when DMC was used the organic solvent during synthesis[156, 170], however a possible explanation has not yet been explored. AFM imaging was performed on cross-sectioned PLGA particles described in table 1, to reveal the internal structure of the particles. It was seen in Figure 4.7, that the PLGA-2 particles in 4.7A revealed a solid internal structure, which was consistent with those produced in DCM.[162] The PLGA-4 particles seen in 4.7B revealed a porous internal structure consisting of 6 large cavities ranging in diameter from 2.3 – 4.2 µm with many smaller cavities sporadically throughout the particle.

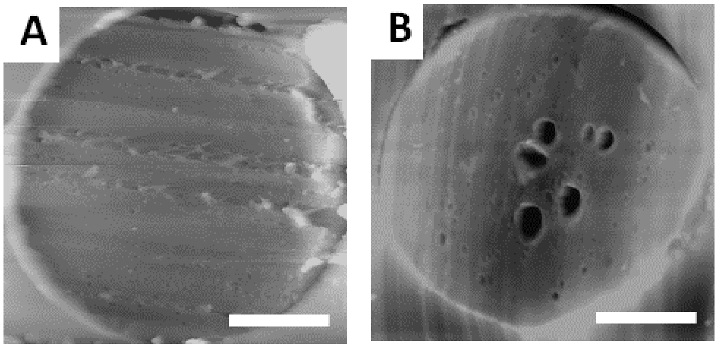

Figure 4.7. Topographic AFM imaging of the cross-sectioned PLGA-2 (A) and PLGA-4 (B) microparticles. For all images, scale bar = 10 µm.

It has been reported that PLGA particles fabricated out of DMC, reveals a hollow internal structure, which is similar to the cavities observed.[43] The center of a PLGA particle has been shown to degrade faster than the rest of the matrix, which could create a larger and coalesced cavity for the PLGA-4 particles during release. This coalesced cavity, could cause structural instability in the particle, and the external release forces, i.e., particle collisions during release, leading to particle collapse, which would form the pancake like structure observed.

Using this insight into PLGA-4 morphology and geometry from time dependent SEM imaging , the burst release region was identified to occur in the first 6 days, while past 6 days, entered a degradation region. During the burst release region, Fickian diffusion occurs through a spherical particle geometry, similarly to PLGA-2, however in the degradation region a "pancake" like geometry was revealed, indicating diffusion occurs through a thinner geometry. Utilizing the regions identified by Figure 4.6, a piecewise model was generated as eq. (7). The first region in the model is identical to eq. (6), however in the second stage of release the Fickian diffusion term for a sphere is replaced for a film[146], to better represent the observed geometry during release.

$$\frac{M_t}{M_\infty}=\begin{cases}\theta_b(1-\exp(-k_b t))+\theta_d\left(1-\frac{6}{\pi^2}\sum_{n=1}^{\infty}\frac{1}{n^2}\exp\left(-\frac{\pi^2 n^2 D_e t}{r_p^2}\right)\right) & t\leq t_1\\ \theta_d\left(1-\frac{6}{\pi^2}\sum_{n=1}^{\infty}\frac{1}{(2n+1)^2}\exp\left(-\frac{\pi^2(2n+1)^2 D_e t}{2l^2}\right)\right)+\theta_r\left(\frac{\exp\left(k_r(t-t_{max})\right)}{1+\exp\left(k_r(t-t_{max})\right)}\right) & t\geq t_1\end{cases} \tag{7}$$

The model was applied on the PLGA-4 particles through non-linear fitting of its measured release kinetics using eq. (7), and the resulting plot was visualized in Figure 4.8B. The burst region was plotted up to 6 days, seen as a solid black line, and was fit mathematically good with R^2 = 0.8697 and RMSE = 2.899. The second region was seen a dashed black line and fits even better with R^2 = 0.9945 and RMSE = 2.145. The extracted fitting parameters were summarized in Table 4.3, columns 10-11.

During t = 0-6 days, the contribution of burst release was, θ_b = 49% with k_b = 0.05 days^{-1}. The diffusion contribution was, θ_d = 50% with D_e = 2.56 x 10^{-15} cm^2/s. In comparison to PLGA-2, θ_b was 3.6-fold higher and D_e was 4.1-fold higher, which was consistent with release from a more porous particle as shown in Figure 4.7 and reported elsewhere.[166-167, 171] These kinetic parameters are seen in Table 4.3, column 10. Past 6 days, diffusion contribution, θ_d = 9% decreased while the D_e = 8.85 x 10^{-12} cm^2/s increased. This trend was similarly seen in PLGA-2, however, θ_d was 3-

fold lower and D_e was 33-fold higher. The dramatic decrease in diffusion contribution was linked to the increase in the diffusion coefficient, where the magnitude was similarly reported in release from polymer films.[146] The contribution of degradation release was, θ_r = 91% with a degradation constant, k_r = 0.14 $days^{-1}$. The degradation contribution was 1.2-fold smaller for PLGA-2, while the degradation constant 2.7-fold larger. The increase in θ_r indicates that degradation release might be more sustained past 6 days for particles that flatten. The decrease in k_r was verified by greater release rate stimulated by particle fragmentation.

Application of this new approach was demonstrated even further with the use of the smaller PLGA-3, seen in Table 4.1, row 3. As shown in figure 6, top row, at t = 0 days, all of the particles presented a smooth and spherical geometry. At t = 3 days, 7 out of 15 particles present geometrical distortion in the form of deflation, while all particles presented grooves on the exterior, similarly seen in PLGA-4. At t = 7 days, the particle surface increased in roughness, which was indicative of the onset of degradation, seen in PLGA-4. At t = 21 days, the geometry of the particles evolved into a "pancake" like structure, with minor erosion along the peripheral. The thickness of these "pancakes" was approximated in the SEM images, where $l \sim 4$ µm, which is slightly larger than those in PLGA-4. By t = 30 days, the particles evolved further in the flattening process to film-like geometries, where erosion was clearly visualized. The identification of the time regions in PLGA-3 is the same as those reported in PLGA-4.

The model described for PLGA-3 particles was applied on the measured release kinetics through non-linear least squares fitting using eq. (7) as shown in Figure 4.8A. The burst region was plotted up to 6 days, seen as a solid black line, and was fit mathematically well with R^2 = 0.9690 and RMSE = 0.9822. The second region is seen a dashed black line, and also fits well with R^2 = 0.9988 and RMSE = 1.156.

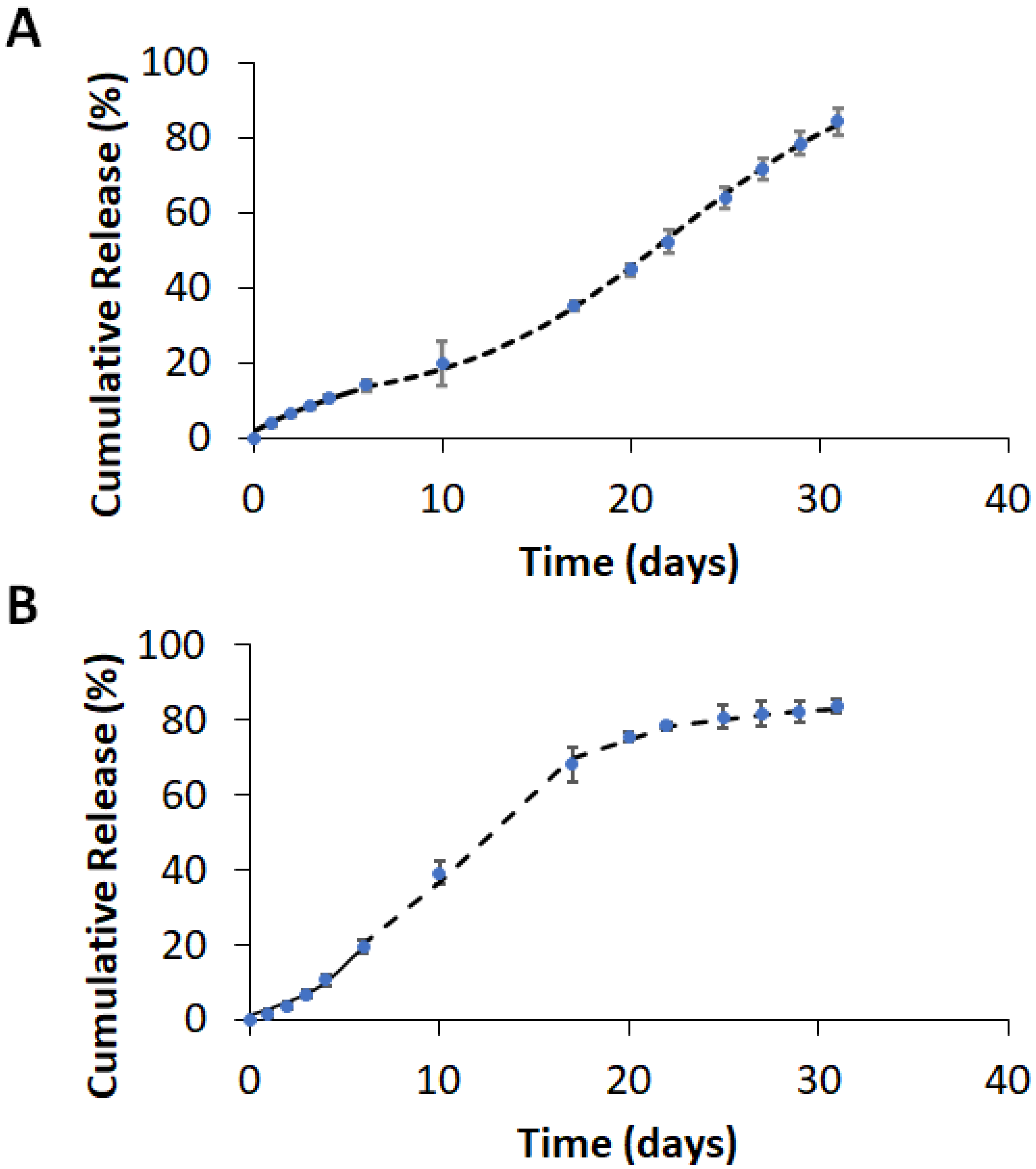

Figure 4.8. Drug release profile of PLGA-3 (blue dots, A) and PLGA-4 (blue dots, B). In each time point of measurement, the result was expressed as mean ± SD from *n* = 3 independent batches of PLGA microparticles. Nonlinear least-square fitting of the release profile using eq (7) was shown as the solid black line for 0-6 days and dashed black line for 6-31 days.

During t = 0-6 days, contribution of burst was, θ_b = 19% with burst constant, k_b = 0.12 $days^{-1}$. When comparing to PLGA-4, it is shown that the burst constant is 2.3 fold larger, which was consistent with slower burst release reported in larger particles.[31, 158] The diffusion contribution was, θ_d = 80.64% with effective diffusion coefficient, $D_e = 7.46 \times 10^{-16}$ cm^2/s. The diffusion contribution was similar to PLGA-4; however, it was revealed that D_e is 3.4 fold slower. Past 6 days, diffusion contribution drastically dropped to 8% with diffusion coefficient, D_e = 1.40×10^{-12} cm^2/s. This was similarly seen in PLGA-4, however the diffusion coefficient decreased, which is consistent when particle size decreases.[56] The contribution of degradation was, θ_r = 92% with k_r = 0.17 $days^{-1}$. These results are similar to those reported in PLGA-4.

When comparing against particles that fragment, i.e., PLGA-1 and PLGA-2, there are insights that are revealed. For instance, the degradation rate constant was overall larger for particle fragmentation, which was correlated with the sudden release around 21 days, seen in Figures 4.1 and 4.5. This revealed insight that particle fragmentation led to faster degradation release. However, the contribution of degradation release was larger for flattened particles, revealing new insight that degradation release during a geometrical shape change played a larger role in release mechanism than when fragmentation occurs. In terms of the diffusion coefficient, particles that flatten have a faster diffusion rate than particles that fragment revealing new insight that geometrical change to a "pancake" result in faster diffusion of drug. Application of this approach in the new kinetics model demonstrated genericness and revealed new insight in drug release that current model could not unveil.

4.4 Conclusions

We developed a new approach to quantify the release kinetics of flavopiridol loaded PLGA microparticles. In contrast to the multiple term single equation model used in the past, we used a piecewise model with the time region determined independently using time-dependent SEM imaging. When applying the conventional model to quantify release profile of flavopiridol loaded PLGA microparticles, we ran into the limitations that the contribution of burst release, θ_b, and burst constant, k_b, remained constant throughout the long term 30-day release period. This new approach has addressed this limitation. High resolution SEM and AFM enabled accurate monitoring of geometry changes during release as such, the correct diffusion term can be utilized where an accurate equation involving spherical or film diffusion can be selected. Accurate morphology and geometry evolution enable the selection of the correct piecewise equation. Degradation of the particles underwent different geometrical resolution, because of a intraparticulate porous structure as revealed by AFM. The parameters derived from our piecewise equation approach can be used to guide particle synthesis in order to meet the local sustained release requirement, in vivo. The approach reported in our work, can be utilized with other encapsulated drugs or even in other polymeric systems, where researchers can use the extracted parameters to tune formulations and release kinetics.

CHAPTER V

Production of Flavopiridol Loaded Inhalable Ultra-small Particles for Pulmonary Delivery

5.1 Introduction

Flavopiridol is a well-known small molecule cyclin dependent kinase inhibitor (CDK) originally designated by the Food and Drug Administration (FDA) as an orphan drug for treatment of rare leukemia.[63]. The activity of flavopiridol has been known to prevent activation of primary response genes, thus inhibiting down-stream inflammation of cells and tissues. [40, 64-68] Therefore, Flavopiridol has been used to treat inflammation caused by illnesses ranging from cancer[63, 69-70], viral[71-73] and post-traumatic-osteoarthritis (PTOA)[40, 65-66], Given its high efficacy, Flavopiridol has been identified as a very promising candidate to treat illness such as lung cancer[74] or coronavirus disease 2019 (COVID-19) pertaining to lung inflammation.[75-76] In past attempts to treat lung injury, the delivery means included intraperitoneal (i.p.) injection into the lower quadrant of the abdomen or via gavage, which involved forcible oral delivery.[77] To improve efficacy and patient-friendliness, pulmonary delivery of inhalable particles using a device such as a dry powder inhaler (DPI) is becoming an urgent need, as inhalation delivery has intrinsic advantage of being non-invasive and rapid. [78-80] While inhalable delivery of drugs has been reported[81-83], none of the current vehicles have been used to carry flavopiridol. Therefore, new research and development (R&D) efforts must be invested from determining the formulation, to reaching the desired physio-chemical property, inhalability, release profile and efficacy. This work reports our effort in the production and characterization of flavopiridol-loaded inhalable ultra-small particles for pulmonary delivery. The particles produced meets the physio-chemical property, inhalability, and release profiles. In vitro activity also meets the requirements. To the best of our knowledge this work represents the first vehicles to carry flavopiridol for pulmonary delivery purposes. This investigation reveals important insights of particle formulation-structure and morphology-property correlation. The application potentials include treatment of lung inflammation from diseases like lung cancer, pulmonary fibrosis, and COVID-19.

5.2 Experimental Methods

5.2.1 Materials

1,2-dipalmitoyl-sn-glycero-3-phosphocholine (DPPC) was purchased from Avanti Polar Lipids (Birmingham, AL). Flavopiridol was purchased from Cayman Chemical Company (Ann Arbor, MI). L-leucine, L-isoleucine, D-(+)-Glucose, Calcium chloride ($CaCl_2$), Tween-20, and Ethanol 100% was purchased from Sigma Aldrich (St. Louis, MO). Phosphate-buffered saline (PBS) (1X) was purchased from Mediatech (Manassas, VA). Gaseous nitrogen was purchased from Praxair (Danbury, CT). 10- and 20-mL glass scintillation vials was purchased from UC Davis (Davis, CA). Poly(tetrafluoroethylene) (PTFE) tubing was purchased from Cole-Parmer (Vernon Hills, IL). 96 well plates, 10- and 20-mL glass scintillation vials, and 1.00 mm ID glass capillary tubes were purchased from Fisher Scientific (Hampton, NH). Variable area flowmeter was purchased from Dwyer Instruments Inc (Michigan City, IN) Dulbecco's modified Eagle's Medium (DMEM), Fetal Bovine Serum (FBS), and 2X Lysis reagent were purchased from Invitrogen (Waltham, MA). Human embryonic kidney 293 cells (HEK-293) were purchased from ATCC (Manassas, VA). Nuclear factor kappa B (NF-κB) reporter (cat # H-60650) and One-Step Luciferase Assay System were purchased from BPS Bioscience (San Diego, CA). Tumor necrosis factor alpha (TNF-α) was purchased from Peprotech (Cranbury, NJ). Ultrapure water with a resistivity of 18.2 MΩ·cm was generated using a Millipore Milli-Q system (EMD Millipore, Billerica, MA).

5.2.2 Production of Flavopiridol Loaded L-isoleucine/DPPC Microparticles

The Microfluidic Piezo and Cyclone Apparatus (MPCA) was designed and fabricated by us and is visualized schematically in Figure 5.1. Some components of the apparatus were similar to previously reported spray drying technique, however the use of a piezoelectric nebulizer disk with orifice array and cyclone design is unique. Feed solutions of L-isoleucine/DPPC (ILD) were prepared using similar methods previously reported.[172] Briefly, 27 mg of L-isoleucine was added to a 10 mL glass scintillation containing 3 mL of Milli-Q water. 3 mg of DPPC was added to a 10 mL glass scintillation vial containing 7 mL of ethanol. Both vials were closed tightly and sonicated(Cole-Parmer, Vernon Hills, IL) for 15 minutes until complete dissolution. Following sonication, the entire contents of the DPPC vial was added to the L-isoleucine vial, and sonicated for 15 minutes, making a 0.3 % (w/v) ILD feed solution. The ILD feed solution was pulled into a 10 mL syringe (BD, Franklin Lakes, NJ) and equipped on a syringe pump (New Era Pump Systems Inc., Farmingdale, NY). For synthesis operation, as visualized in the schematic in figure 1B, the ILD feed solution was pumped into PTFE tubing via syringe pump at 22 mL/hr. The end of the PTFE tubing contained a 30 AWG blunt needle hovering 1 cm directly over the piezo actuated orifice array. The piezo actuated orifice array is a commercial humidifier (STEINER & MARTINS, INC., Davenport, FL), composed of a stainless-steel disk with an array of 4- 11 μm holes, ceramic piezo rings are fixed on the top and bottom of the array. The ILD solution was dropped onto the microfluidic piezo array which was actuated via custom piezo driver at 113 kHz with 30V of power. The gravitational force caused the large droplet on top of the device to be pulled into the array, causing the formation of a spray of micronized droplets. At the top of the acrylic box, which houses the entire apparatus, a nitrogen inlet fed into the enclosure at 15 L/min.. The nitrogen gas carried and began to dry the micronized droplets for 55 cm until it reached the custom PTFE funnel where the vacuum pull led to the cyclone chamber. The cyclone separator with funnel was designed in Solidworks® CAD software with a cylinder-on-cone design with a tangential inlet and manufactured in PTFE at Crocker machine shop (UC Davis, CA). In the cyclone chamber, the particles strike the side walls causing a decrease in momentum effectively landing in the screwed on 20 mL glass scintillation collection vial, while the gas and evaporated solvent traveled to the vacuum outlet and were removed

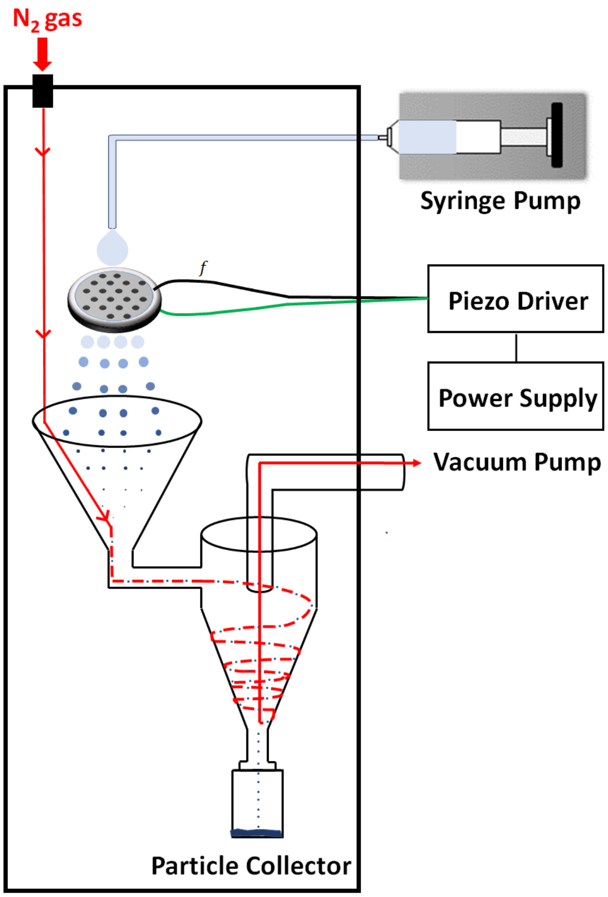

Figure 5.1 Schematic representation of the Microfluidic Piezo and Cyclone Apparatus for inhalable particle production.

Via an RV5 vacuum pump (Edwards Vacuum LLC, San Jose, CA). The synthesis was performed at ambient room temperature, 24 °C. The detailed and optimal synthesis parameters are seen in

Table 5.1.

Table 5.1. Optimal MPCA operation parameters for particle synthesis

Parameter	Value
Micro-piezo orifice diameter	11 μm
Feed solution temperature	23 ± 1 °C
Feed solution flow rate	22.0 mL/hr
N_2 gas flow rate	15 L/min
N_2 gas temperature	23 ± 1 °C
Piezoelectric driving frequency	113 kHz

To demonstrate robustness, 0.1 and 0.5 % (w/v) total excipient concentrations are also prepared and used using identical conditions seen in Table 5.1. Flavopiridol incorporation into the formulation (ILDF) was prepared by adding 28.8 μL of a 1 mg/mL Flavopiridol in ethanol solution, into the DPPC vial described above.

5.2.3 Measurements of Loading Capacity and Efficiency of Flavopiridol in L-isoleucine/DPPC Microparticles

Flavopiridol loading in the ILDF formulation microparticles was determined using similar methods reported[67] by dispersing ~ 4.8 mg of particles (m_p) in 1 mL of 70% (v/v) Ethanol in water. The dispersion was sonicated for 15 minutes, until complete dissolution of the particles was complete. The dissolved solution was loaded in a 1 mL syringe and filtered into a quartz cuvette using a 0.2 μm PTFE syringe filter (Sigma Aldrich, St. Louis, MO). The filtered solution was subject to UV-Vis spectroscopy using a Denovix DS-11 spectrometer (Denovix Inc., Wilmington, DE), and the absorbance (A) at 358 nm, characteristic of Flavopiridol was measured. The molar extinction coefficient (ϵ) of flavopiridol at 358 nm was determined using a standard concentration range from 3 – 100 μM, and the concentration of flavopiridol (c) was calculated using Beer's law. The encapsulated mass of flavopiridol (m_f) in the ILDF particles was determined by multiplying c with the volume (1.00 mL) and the molar mass of flavopiridol. The loading capacity (LC) of flavopiridol was quantified using eq. (1),

$$\mathrm{LC} = \left(\frac{\mathrm{m_f}}{\mathrm{m_p}}\right) \mathrm{x}\ 100\% \qquad (1)$$

The encapsulation efficiency (EE) of flavopiridol was quantified using eq. (2) by dividing the LC with the desired loading capacity of flavopiridol in the formulation ($\mathrm{LC_{desired}}$ = 0.192 % (w/w)).

$$\mathrm{EE} = \frac{\mathrm{LC}}{\mathrm{LC_{desired}}}\ \mathrm{x}\ 100\% \qquad (2)$$

5.2.4 Scanning Electron Microscopy Imaging of Produced Particles

The microparticle geometry and size were determined using a field emission scanning electron microscope (SEM) (S-4100T, Hitachi High Technologies America, Inc., Pleasanton, CA). Produced particles stuck to double sided carbon tape mounted on an Al stub were coated with 10 nm of gold using a sputter coater (Ted Pella Inc., Redding, CA) and then transported to the SEM vacuum chamber. The typical acceleration voltage and emission current were 2 kV and 10 μA, respectively. The SEM images were loaded into Image J, where the size of the microparticles was determined using the geometrical Feret diameter (d_g).

The aerodynamic diameter (d_a) was calculated using eq. (3), where The tapped density was measured using established protocols[80], where the measured tapped density (σ) which was determined over 1000 taps, and the reference density (ρ) is 1 mg/mL.

$$d_a = d_g \sqrt{\frac{\sigma}{\rho}} \tag{3}$$

5.2.5 In vitro release of Flavopiridol from L-isoleucine/DPPC Microparticles

In vitro release experiments were performed to characterize release of flavopiridol from the ILDF particles by utilizing demonstrated release protocols[67, 173]. Briefly, 5 mg of ILDF particles were placed in 6 x 1.5 mL Eppendorf tubes containing 0.5 mL of 1X PBS/0.2% Tween-20 aqueous solution at 37 $°C$. To establish sink conditions as described previously[126], tween-20 was added to ensure dissolution of flavopiridol in the release medium. At each selected time point, one vial was removed and centrifuged at 16,000 rpm for 10 min, and the supernatant was collected and filtered using a 0.2 μm PTFE syringe filter. The supernatant was analyzed at 358 nm using UV-Vis spectroscopy for determination of flavopiridol concentration. After all vials were analyzed for release of flavopiridol, the cumulative percentage of flavopiridol was calculated using eq. (4), by taking the summation of flavopiridol released up to a designated time, t, and then normalizing by the amount of flavopiridol loaded ($\mathrm{m_f}$).

$$\text{Cumulative Release (\%)} = \frac{1}{\mathrm{m_f}} \sum_{\mathrm{t=0}}^{\mathrm{t=t'}} \mathrm{m_t} \tag{4}$$

5.2.6 Quantification of In-vitro release kinetics

The in vitro release profile described above was quantified using a 2-term model similarly to previously described methods.[61, 148] that incorporates initial burst and Fickian diffusion release as shown in eq. (5).

$$\frac{\mathrm{M_t}}{\mathrm{M_\infty}} = \theta_\mathrm{b}\left(1 - \mathrm{e}^{-\mathrm{k_b t}}\right) + \theta_\mathrm{d}\left(1 - \frac{6}{\pi^2}\sum_{\mathrm{n=1}}^{\infty} \exp\left(-\frac{\pi^2 \mathrm{n}^2 \mathrm{D_e t}}{\mathrm{r_g^2}}\right)\right) \tag{5}$$

The first term represented the process of "burst release", with k_b as the burst constant and θ_b as the contribution of burst release. This burst process was mostly described as interfacial diffusion, where drug that was located near or at the surface of the particle underwent rapid dissolution.[60] The 2nd term describes diffusion of drugs from spherical matrices under Fickian diffusion, where D_e was the effective diffusion coefficient, r_g was the geometrical mean particle radius, and θ_d was the contribution of diffusion release. [151, 174-175]. The constraint, $\theta_b + \theta_d = 1$, was used for mathematical completeness, representing individual contributions in the release mechanism. The in vitro release profile underwent regression analysis using nonlinear least squares algorithm in MATLAB (Math Works, USA).

5.2.7 Stability measurements of ILDF particles

The stability of the ILDF particles was determined in some of the previously reported conditions[176-177]. 1-2 mg of freshly prepared particles described above was placed in 24 x 1.5 mL Eppendorf tubes equally over four different environments. The four environments were 24 °C in the light and dark, 4 °C in the refrigerator, and 37 °C in an incubator. At certain time points, 0.5 mL of 70% ethanol was dispensed in the vial, and the contents were sonicated for 15 minutes until complete dissolution was reached. The solution was filtered into a quartz cuvette via 0.2 μm PTFE syringe filter and the UV-Vis spectrum was measured from 220 – 750 nm for each of the samples. The measured spectrums were compared qualitatively against freshly produced ILDF formulation to determine stability of the formulation.

5.2.8 ATR-FTIR

Attenuated Total Reflectance – Fourier Transform Infrared Spectroscopy (ATR-FTIR) was used to characterize the ILDF formulation for identification of excipients in the produced particles using established methods.[172] Briefly, < 1 mg of solid L-isoleucine, DPPC, and flavopiridol starting materials and produced ILDF formulation particles were placed and compressed on the ATR diamond crystal. The FTIR spectrum was scanned 30 times with 4 cm^{-1} resolution over the wavenumber range of 4000 – 400 cm^{-1} using a Bruker Tensor 27 FTIR (Bruker Corporation, Billerica, MA).

5.2.9 In-Vitro Bioactivity Assay

The bioactivity of flavopiridol released from ILDF particles was determined by a luciferase reporter assay as described previously.[67, 127] 18.94 mg of ILDF particles containing 0.190 % (w/w) flavopiridol was dissolved in DMEM with 10% FBS to a stock solution of 8.9 x 10^4 nM flavopiridol. The bioactivity of flavopiridol was measured by its ability to suppress TNF-stimulated luciferase reporter expression, driven by a NF-kB responsive promoter. The HEK293 cells harboring a NF-kB-driven luciferase reporter were seeded in 96-well plates (10,000 cells/well in triplicates) 24 hours before the experiment. Cells were then treated with 100 μL of media containing 0.6 nM recombinant human TNF-α, in the presence or absence of various amount of dissolved flavopiridol formulation or blank formulation equivalent. After 24h, 100 μL of 2X lysis buffer containing luciferase substrate was added directly to each well. Luminescence was measured in a plate reader (SpectraMax iD3, Molecular Devices, San Jose, CA). The luminescence reading from samples treated with TNF-α only was arbitrarily set to 100% and then compared to flavopiridol-treated samples.

5.3 Results and Discussion

5.3.1 Formulation of flavopiridol-loaded particles to be used for pulmonary delivery

In the design of inhalable particles, excipients represent the major components, thus determine the physio-chemical property, impact, release profile, and toxicity.[79-80] Many excipients have been used in inhalable particle formulations, such as amino acids, sugars, and lipids.[82, 93, 99, 172, 178] The amino acids like L-leucine and L-isoleucine are generally used due to their property as dispersibility enhancers.[80, 99] In this work, we tested both L-Leucine and L-isoleucine as the primary excipients in the formulation. L-leucine was found to precipitate and made a cloudy appearance in an ethanol-water mixture; therefore, we went with L-isoleucine which was soluble. Addition of phospholipids, to the formulation has been demonstrated to present successful entry into cells for delivery of the therapeutic.[179-180] Following additions of a phospholipid to the L-isoleucine was visualized in Figure 5.2A resulted in particle morphology composed of outward folded sheets that were analogous to a "rose-bud" morphology. It has been shown with the commercial product, Pulmosphere®, that the addition of (2:1) $CaCl_2$ to phospholipid formulations, resulted in improved environmental robustness.[181] As seen in Figure 5.2B, the addition of $CaCl_2$ resulted in heterogeneity in shape with a flattened heterogenous morphology, therefore $CaCl_2$ was excluded from the formulation. The addition of sugars, like glucose to the formulations has been demonstrated through enhancing bioavailability during pulmonary delivery.[178, 182] Addition of glucose to the formulation as shown in Figure 5.2C, resulted in solid particles with low surface to volume ratio, which was not desired for pulmonary delivery, since it was been shown to inhibit dispersibility of the particles during inhalation.[183]

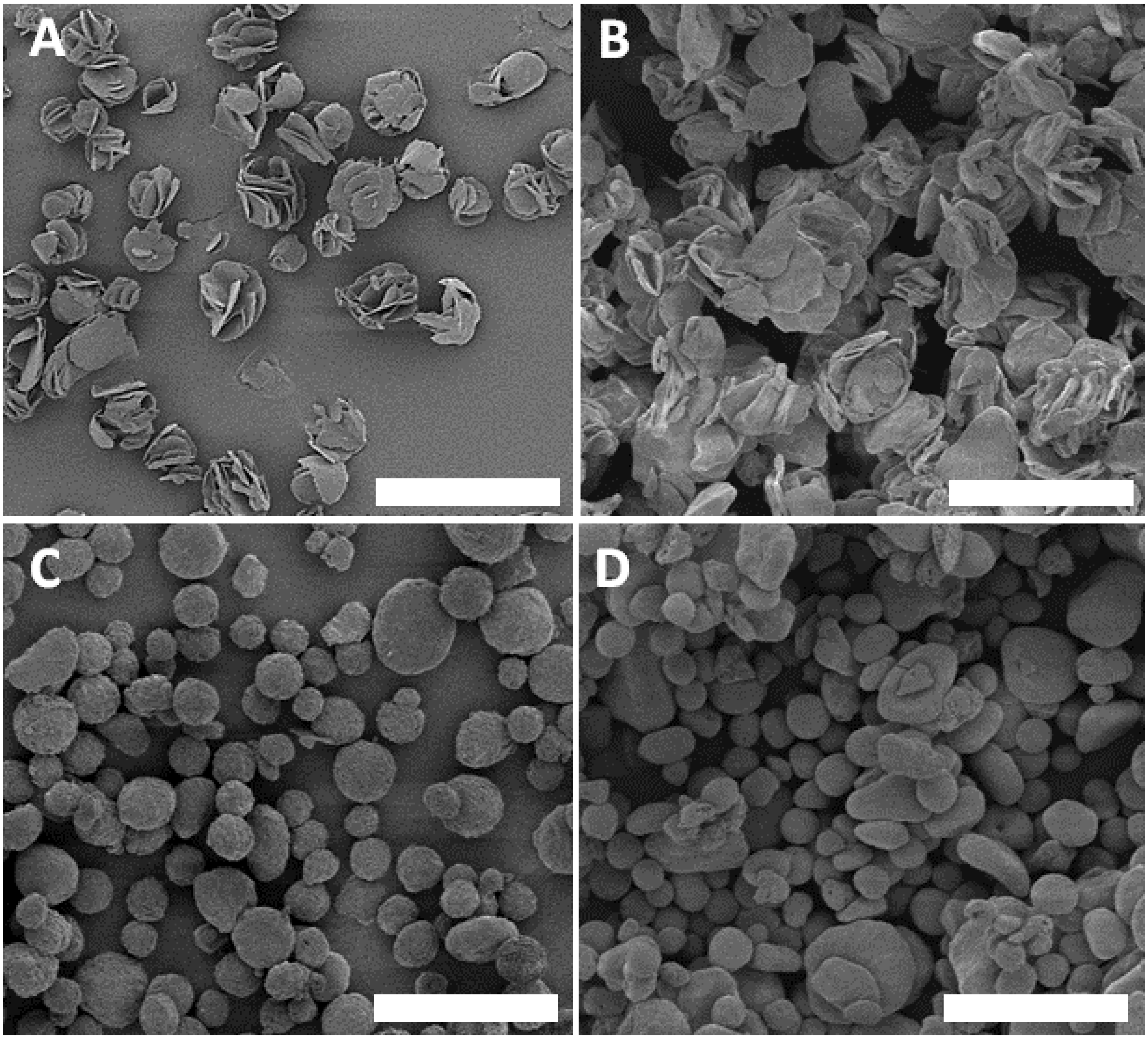

Figure 5.2. SEM imaging of potential formulation components. A. (90:10) L-isoleucine/DPPC B. (89.25:10:0.75) L-isoleucine/DPPC/$CaCl_2$. C. (10:10:80) L-isoleucine/DPPC/Glucose at 70 % (v/v) ethanol:water. D. (10:10:80) L-isoleucine/DPPC/Glucose at 80 % (v/v) ethanol:water. All scale bars = 20 µm

The phospholipid used in the formulation was DPPC, which has been demonstrated in literature for many pulmonary delivery vehicles.[172-173] Ethanol-water mixed solvent was utilized during synthesis, due to DPPC high solubility in Ethanol and L-isoleucine solubility in water. The active component, flavopiridol, is easily identified in the UV-Vis spectrum at λ_{max} = 358 nm as shown in Figure 5.3. because there is no overlap with any other component in the particle.

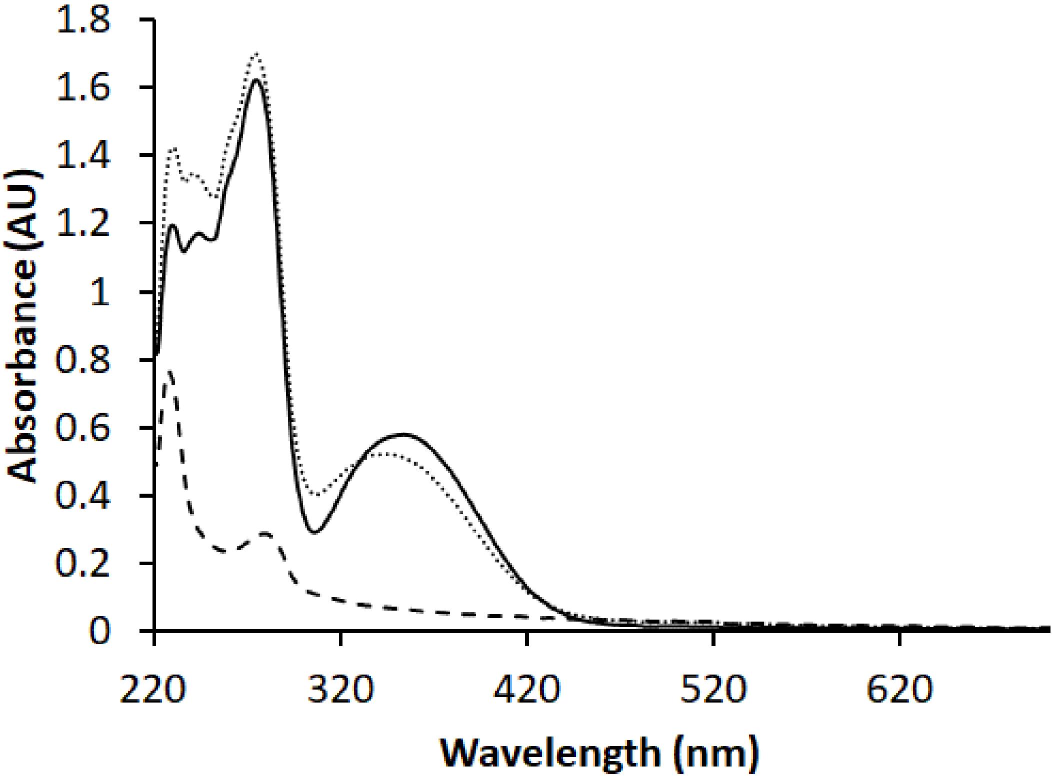

Figure 5.3. Absorption spectra of L-isoleucine/DPPC particles loaded with Flavopiridol after dissolving in 70 % Ethanol (small black dash) displayed with that of 50 μM Flavopiridol in 70% Ethanol (Solid black line) and L-isoleucine/DPPC particles (large black dash). The absorption at λ_{max} = 358 nm was used to quantify flavopiridol concentration and calculate loading capacity.

5.3.2 Quantitative determination of the formulation of flavopiridol-loaded particles for pulmonary delivery

With the formulations at hand, we varied the MPCA operation parameters systematically until optimal values were reached. The microfluidic piezo orifice diameter was varied from 4 – 11 μm. It was found that the minimum orifice diameter for droplet spray production was 11 μm, while <

11 μm was unable to produce a continuous spray due to orifice clogging. The formulation feed flow rates were varied from 5 – 30 mL/hr. From 5- 22 mL/hr, the droplet spray was continuous over the entire synthesis timeline, while 23 – 30 mL/hr resulted in intermittent droplet spray due to overfilling. Therefore, 22 mL/hr was chosen as the optimal formulation feed flow rate. From these parameter variations, the optimal operation parameters were selected and were summarized in Table 5.1.

The % composition of DPPC in the formulation was varied from 5 – 30 %. When DPPC is 5%, the majority of the particles presented a flattened morphology, while greater than 10% DPPC, the curvature and surface to volume ratio increased. Therefore, the optimal % of DPPC was selected to be 10%, due to the desired "rose-bud" particle morphology, described previously.

The total excipient concentration has been shown to affect particle size and morphology and was typically in the range of 0.1 – 0.5% (w/v).[184] In this work we tested 0.1 – 0.5% (w/v), whereas the concentration increased, the size of the particles increased proportionally. At 0.1 %(w/v), the particle production rate is too slow for adequate sample testing, while at 0.5 %(w/v), micro piezo orifice frequently clogged, causing an intermittent production rate. The optimal concentration was determined to be 0.3 %(w/v), due to an excellent continuous process and yield.

The EtOH:water feed solvent composition has been demonstrated to affect particle morphology and drying kinetics[99], therefore the composition was varied from 50:50 - 80:20. At 50:50, the ethanol concentration was too low for complete evaporation of solvent during synthesis, which resulted in liquid in the collector. At 70:30, complete evaporation of the solvent was observed with dry powder in the collector, producing particles as shown in Figure 5.1C. When the ethanol composition increased to 80:20, the particle morphology became flattened as shown in Figure 5.1D. Therefore, EtOH:water at 70:30 was selected as the solvent. The optimal composition, concentration, and solvent are summarized in Table 5.2.

Table 5.2. Optimal formulation for particle synthesis using MPCA

Sample	EtOH:Water (%(v/v))	IL (%)	DPPC (%)	Flavopiridol (%)	Total Concentration (% (w/v))
ILD-3	70	90	10	0	0.3
ILDF	70	89.808	10	0.192	0.3

For each synthesis, we characterized the process yield, LC, EE, ρ_{tapped} following the protocols described in the experimental above. In addition, the geometrical and aerodynamic diameter of the particles and their dispersity was investigated using SEM. Among the multiple series of synthesis performed, we included the representative results in Table 5.3.

Table 5.3. Properties of the ILD and flavopiridol loaded ILD particles for pulmonary delivery

Formulation	Process Yield (%)	LC (%)	EE (%)	ρ_{tapped} (mg/mL)	d_g (μm)	d_a (μm)	Dispersion
ILD-3	43	0	0	0.19 ± 0.01	5.4 ± 1.2	2.4 ± 0.5	High
ILDF	45	0.19 ± 0.01	99 ± 2	0.20 ± 0.01	5.5 ± 1.3	2.5 ± 0.6	High

The concentration of flavopiridol of 300 nM has been demonstrated to be optimal for treatment of inflammation, in the synovial knee joint.[64, 68, 156] During the route to the lung, the inhalable particles reach the epithelial lung lining fluid (LLF), where eventually flavopiridol becomes bioavailable.[185] The LLF has been shown to have a volume of ~ 20 mL[186], and a typical dose for a DPI is 5 mg.[187] Therefore, the required loading of flavopiridol in the formulation particles is 0.048% (w/w). However, it has been shown that pulmonary delivery using a DPI can result in around 25% deposition of the dose in the lung[188], therefore the amount of flavopiridol was increased by 4-fold to 0.19% in order to account for the loss of drug.

Using MPCA with the optimal operation parameters and formulations listed in Tables 5.1 and 5.2, we began the production of flavopiridol loaded ILDF particles as described in Table 5.3. The flavopiridol loading is 0.19% as determined using UV-Vis spectrum (black dots) in Figure 5.2. The spectrum reveals the same characteristic peaks of the flavopiridol standard (solid black line) in Figure 5.3, from which the peak at 358 nm, was used to quantify the absorbance (A = 0.5003). The loading capacity of flavopiridol in the ILDF particles was quantified using eq (1) and was determined to be, LC = 0.19%. As a negative control, the unloaded ILD particles (black dash) do not exhibit absorption at λ_{max} = 358 nm. The Encapsulation Efficiency (EE) in this synthesis was quantified using eq (2) reached 99 $\pm$ 2%.

The composition was confirmed using FTIR spectroscopy as seen in Figure 5.4. The spectrum of the ILDF formulation (D) most similarly resembles L-isoleucine (A) with a characteristic 1514 cm^{-1} (red star), with a slight presence of the characteristic C=O stretching[189] (blue star) of DPPC (B) indicated above. It was confirmed that L-isoleucine is the major component of the formulation, while DPPC plays a minor role in the composition.

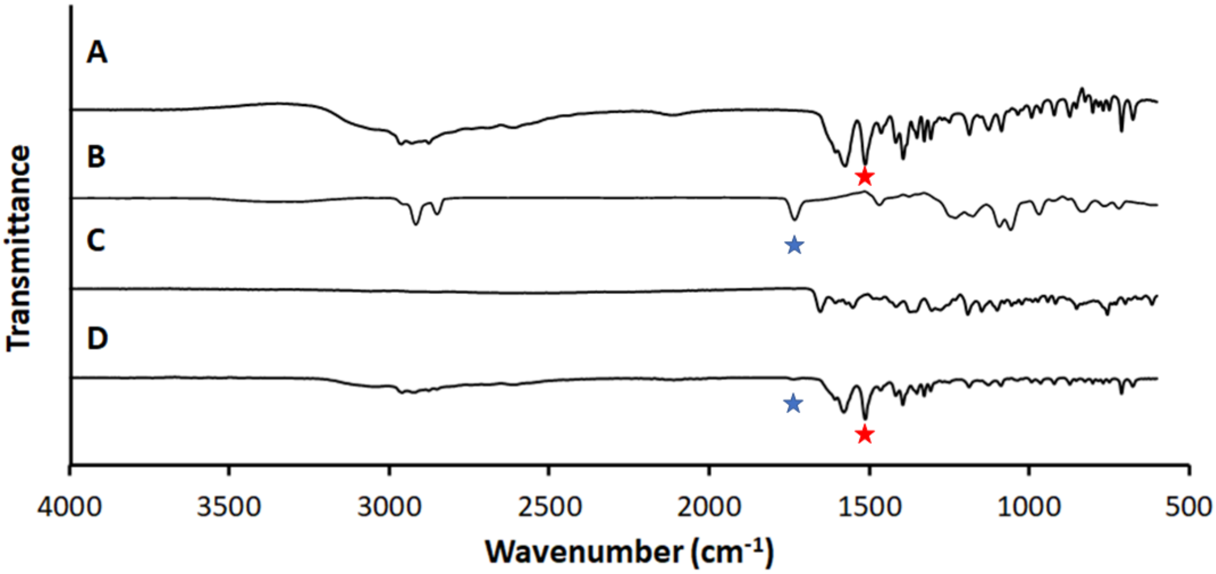

Figure 5.4. Attenuated total reflectance Fourier transform infrared (ATR-FTIR) spectra of starting material (A) L-isoleucine (B) DPPC, (C) Flavopiridol and (D) ILDF particles. The blue and red stars are indicators of reagent specific absorption events.

5.3.3 The ILDF particles exhibit high dispersity and aerodynamic property for pulmonary delivery

The dispersity of the ILDF formulation particles as described in Table 5.3, Row 2, was visualized in Figure 5.5B by mimicking the pulmonary inhalation process from the bench top. The schematic representation for the sampling methodology is seen in Figure 5.5A.

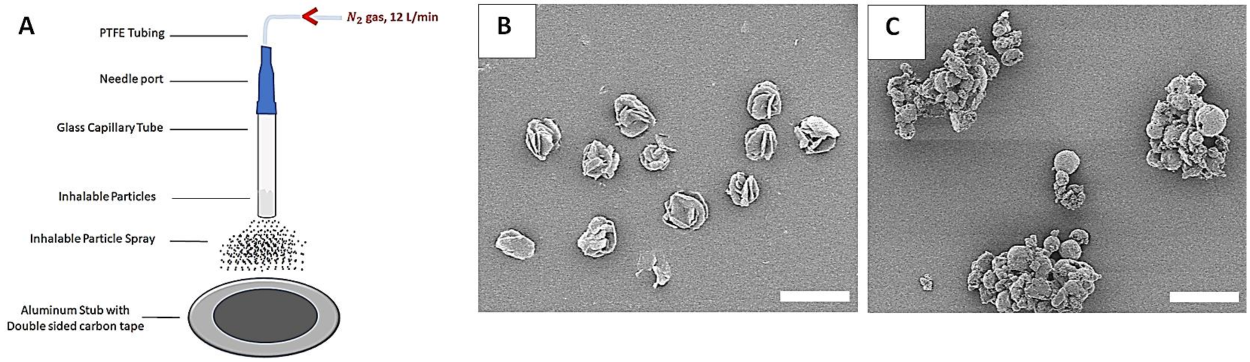

Figure 5.5. Mimicking inhalability of produced particles for pulmonary delivery. A. Schematic representation of new technique to immobilize sprayed particles for dispersity visualization using SEM. B. ILDF formulation particles as described in Table 3, Row 2. C. ILDG particles. All scale bars = 20 μm

Briefly, < 1 mg of powder formulations were inserted into a 1.00 mm ID glass capillary tube and mounted vertically via 3-fingered clamps. The end of the capillary tube was custom fitted with a syringe-needle port, which is inserted into a PTFE tubing. The end of the PTFE tubing is directly fitted to a variable area flowmeter attached to nitrogen gas tank. The flow rate of nitrogen was set at rates comparable to the human breath at sea level, at 12 L/min.[190] Following the spray of the particles, the sample was prepped for SEM imaging as described in the experimental section. As seen in Figure 5.5B, the ILDF particles exhibit high dispersity, with a mean distance between particles $(\bar{x}) = 7.3 \pm 5.5$ μm clearly resolved between particles. To demonstrate the robustness of this method, ILDG particles were synthesized using MPCA and parameter listed in Table 5.1, with D-α-glucose at 80% composition, while DPPC and L-isoleucine was each 10%. It is well known that sugars at high compositions are sticky and cohesive.[178] In Figure 5.5C, ILDG particles are clumped together into aggregates of at least 20 particles, indicating little to no dispersibility. The physical diameter of the ILDF particles as shown in Table 5.3, row 2, was measured from SEM images to be 5.5 ± 1.3 μm. The mean aerodynamic diameter, as following literatures conventions[80], was determined to be 2.5 ± 0.6 μm, which falls into the required aerodynamic range for pulmonary delivery, 1-5 μm.[191]Therefore, the ILDF particles are inhalable with high dispersity and aerodynamic property for pulmonary delivery.

5.3.4 In vitro flavopiridol release profile meets the requirement for pulmonary delivery

In vitro release experiments were performed on the flavopiridol loaded ILDF particles (blue dots) described in Table 5.3, row 2, by utilizing demonstrated release protocols. [67, 173] The required delivery is to release flavopiridol from 5 mg particles rapidly from the particles within hours.[173, 192-193] The overall release profile is visualized in Figure 5.6, where by 3 hours, 99.4 % of drug is released.

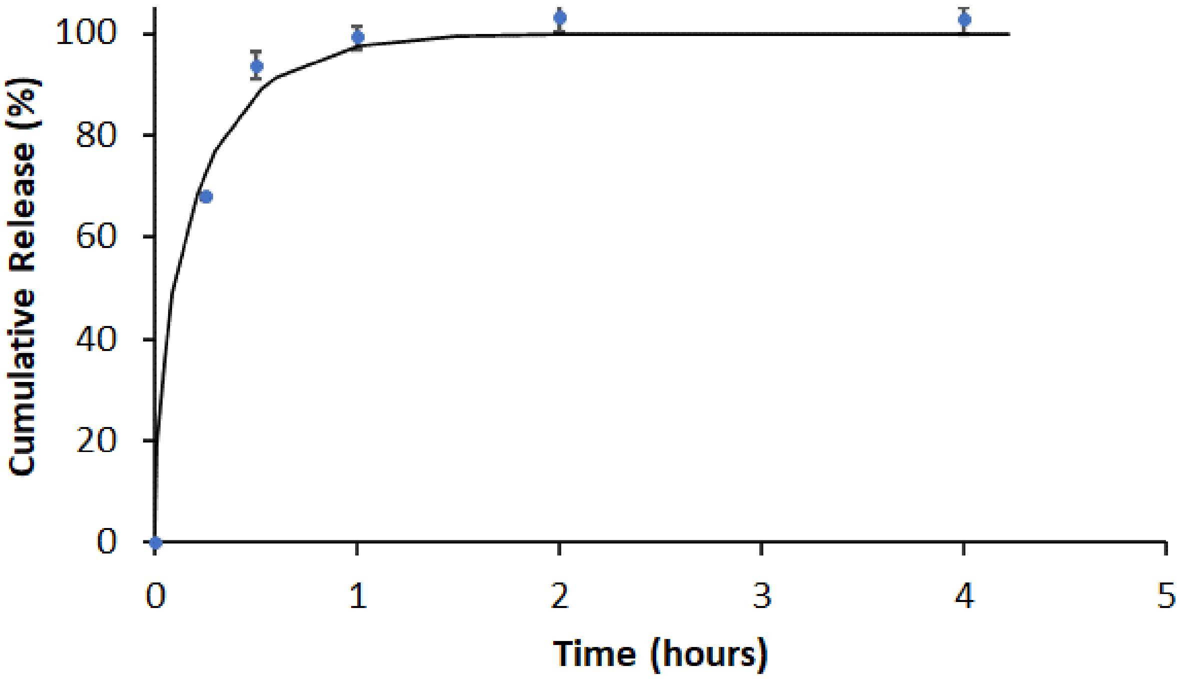

Figure 5.6. Drug release profile of ILDF (blue dots). In each time point of measurement, the result is expressed as mean ± SD from n = 3 independent batches of ILDF microparticles. Nonlinear least-square fitting of the release profile using eq. (5) is shown as the solid black line.

The quantitative kinetics is fitted using known kinetics model, described in experimental and is shown in eq. (5), and the extracted parameters are shown in Table 5.4. The burst constant, k_b = 1.599 hr^{-1}, demonstrates how fast the release of flavopiridol occurs. The diffusion coefficient, D_e = 2.3 x 10^{-11} cm^2/s, was shown to be similar to those calculated in literature.[174] The in vitro release profile of flavopiridol matches the required release kinetics for pulmonary delivery.

Table 5.4. Kinetics parameters extracted from the non-linear least-square fitting of the drug release profile of the ILDF particles using eq(8).

Parameters	Description	Unit	Results
k_b	Burst constant	hr^{-1}	1.599
θ_b	Burst release fraction	-	0.00186
D_e	Diffusion Coefficient	$\frac{cm^2}{s}$	2.341E-11
r_p	Radius of particle	cm	0.00025
θ_d	Diffusion release fraction	-	0.9981
R^2	Coefficient of determination	-	0.9905

5.3.5 The ILDF particles are sufficiently stable for 4 weeks

The ILDF particles described in Table 5.3, row 2 was assessed for chemical and thermodynamic stability under ICH guidelines.[176-177] This was performed under three storage conditions for 4-weeks: refrigerated at 4 $^\circ C$, shelf-stability at 24 °C, and elevated temperature of 37 °C. The stability of flavopiridol in the ILDF particles was monitored by tracking the chemical stability of the molecules with time, using the UV-Vis spectroscopy. Figure 5.7 shows the comparison the outcome in the beginning and at the end of these measurements.

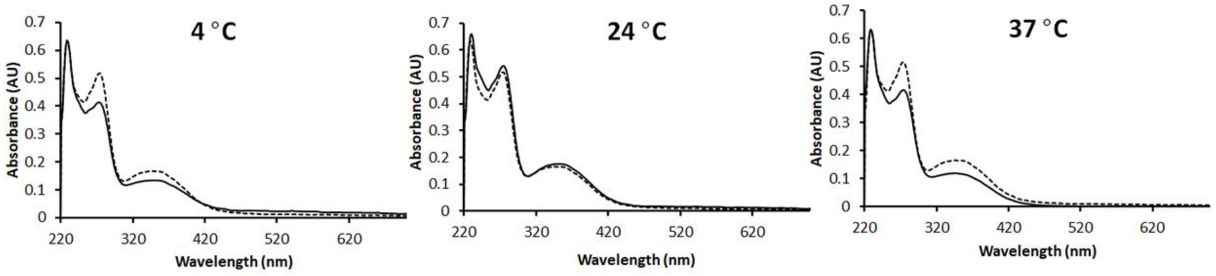

Figure 5.7. The stability of Flavopiridol in ILDF inhalable particles for up to 4 weeks at 4, 24, and 37°C. The UV-Vis spectrum of the ILDF particles in 70% Ethanol (solid black line) after 4 weeks under the three storage conditions are plotted with the freshly produced ILDF particles in 70% Ethanol (dashed black line). The absorption at λ = 230 nm for each spectrum was normalized throughout all profile.

Figure 5.7A reveals the stability under 4 °C, mimicking the storage under house-hold refrigeration, where the appearance of the spectrum of ILDF particles after 4 weeks closely resembles the spectrum of freshly produced particles. Therefore, under refrigerated conditions the formulation particles are stable. Under 24 °C and in the presence of room light, i.e., house-hold shelf storage, the stability remains throughout the 4 weeks of our test period (Figure 5.7B). Even at incubation temperatures, e.g., 37 °C (Figure 5.7C), the stability remains. Therefore, due to the stability remaining throughout the accepted testing described previously, we anticipate the ILDF particles meet the standard and are ready for animal testing.

5.3.6 Flavopiridol in the ILDF particles exhibit high biological activity in vitro

The biological activity of flavopiridol in the ILDF particles was accessed using a luciferase assay.[67, 127] The presence of TNF-α in the luciferase assay, causes activation of luciferase expression which is driven by the NF-κB promoter. In the presence of flavopiridol, this activation is suppressed. As seen in Figure 5.8, The expected maximum luciferase activity was detected in cells treated with TNF only (black bar) and the blank ILD particles (Grey bar) with no statistical difference.

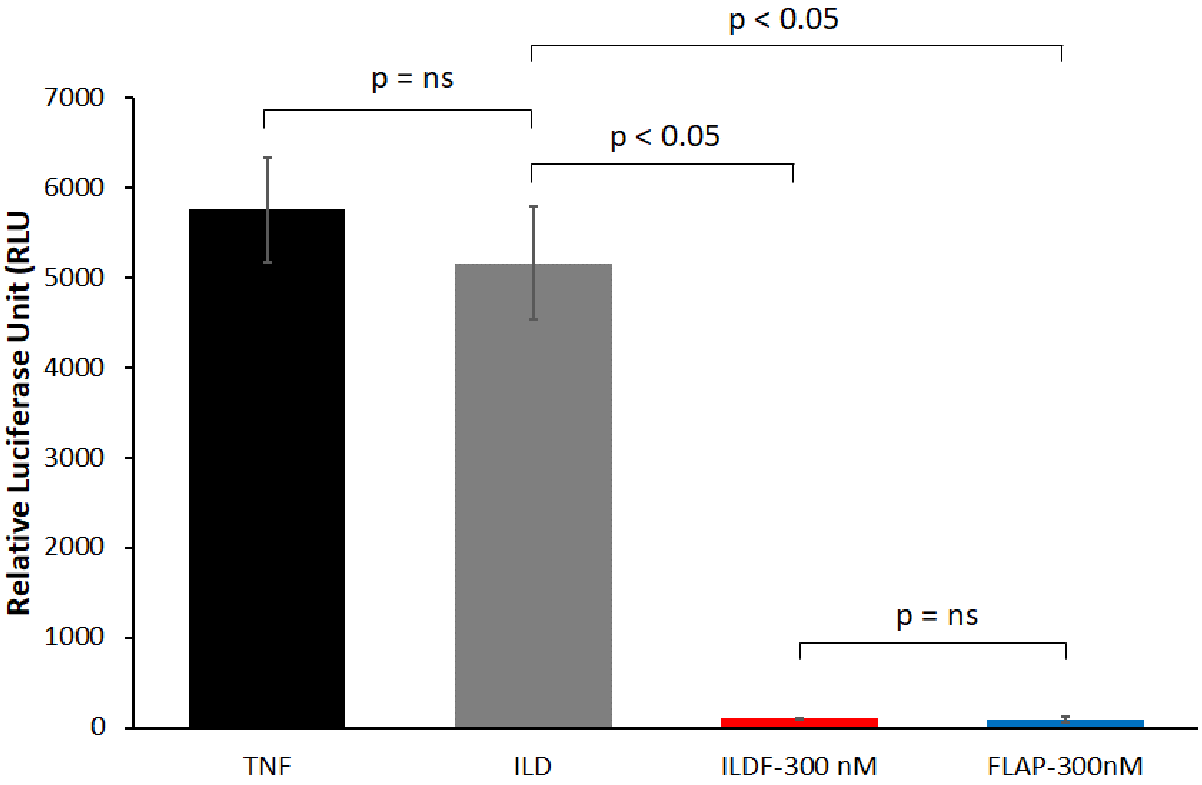

Figure 5.8. Bioactivity of Flavopiridol in ILDF particles measured by luciferase assay. Released flavopiridol (FLAP) from ILDF particles and blank ILD particles were assessed of their bioactivity through suppression of luciferase activity in HEK-Luc reporter cells stimulated with TNF-α (0.6 nM). Experiments were performed in triplicate(N=3) from one batch of particles, and results were reported as mean±SD. *Measurements were taken in conjunction with Dr. Jasper Yik and Dr. Dominik R. Haudenschild in the School of Medicine at University of California, Davis.*

In comparison, cells treated with 300 nM of flavopiridol in the ILDF particles (Red bar) or 300 nM of soluble flavopiridol present the lowest luciferase activity with no statistical difference. This result suggests that the biological activity of flavopiridol in the ILDF particles is retained for pulmonary delivery, which is a powerful indicator in good in vivo behavior.

5.4 Conclusion

This work demonstrates the successful production of inhalable ultra-small particles containing flavopiridol via spray drying technique. These produced particles represented the first time that flavopiridol has been incorporated into particles for pulmonary delivery. The presence of the particle components was verified using UV-Vis and ATR-FTIR spectroscopy. The particles produced were shown to be dispersible in flight, by a new method to determine dispersibility and morphology in the same readout. The in-vitro release profile was demonstrated to match the required release requirement for pulmonary delivery. These particles were demonstrated to be stable at all conditions tested, with no observed spectral changes. The incorporated flavopiridol in the formulation particles was demonstrated to be biologically active and ready for animal studies. This work enabled, the use of flavopiridol as a treatment option for inflammation-based diseases in the lung via pulmonary delivery of inhalable particles.

CHAPTER VI

Conclusions and Future Perspectives

6.1 Conclusions

6.1.1 A Green Approach to Producing Polymer Microparticles for Local Sustained Release of Flavopiridol

Encapsulation of flavopiridol within PLGA microparticles using greener practices was reported for the first time. Current means for synthesizing PLGA microparticles, using either conventional emulsion or MFFD, frequently employ DCM as the solvent in organic phase. Due to DCM's health and environmental toxicity and slow degradation, a green solvent, DMC, is introduced to replace DCM. Using production of FLAP encapsulated PLGA microparticles as an example, this work demonstrates that the use of green solvent does not hinder the synthesis procedure or quality of products. In fact, the use of DMC preserves the narrower size distribution leading to high reproducibility in particle size and drug load. In addition, the particles produced exhibited drug release profiles more desirable for local sustained release into joint for future applications of osteoarthritis treatment. Further, cytotoxicity and biological activity tests demonstrated high biocompatibility and efficacy, respectively. DMC was shown to be a much greener solvent than DCM with approximately one order of magnitude higher LD50 values in rat, 5-fold degradation rate. Additional measures include a 30% higher GlaxoSmithKline (GSK) combined greenness value. In the context of PLGA particle production process, the simple E-Factor (sEF) and complete E-Factor(cEF) of DMC are only a fraction of that of DCM, i.e., 76% and 76%, respectively, which indicates greater sustainability. The approach reported in this work shall also provide a new and green means for production of polymer-based microparticles for local sustained delivery of FLAP for the treatment of osteoarthritis and cancers, and for drug delivery in general.

6.1.2 New Insight into Drug Release Profiles of Flavopiridol Loaded Poly(lactic-co-glycolic acid) Microparticles.

We developed a new approach to quantify the release kinetics of flavopiridol loaded PLGA microparticles. In contrast to the multiple term single equation model used in the past, we used a piecewise model with the time region determined independently using time-dependent SEM imaging. When applying the conventional model to quantify release profile of flavopiridol loaded PLGA microparticles, we ran into the limitations that the contribution of burst release, θ_b, and burst constant, k_b, remained constant throughout the long term 30-day release period. This new approach has addressed this limitation. High resolution SEM and AFM enabled accurate monitoring of geometry changes during release as such, the correct diffusion term can be utilized where an accurate equation involving spherical or film diffusion can be selected. Accurate morphology and geometry evolution enable the selection of the correct piecewise equation. Degradation of the particles underwent different geometrical resolution, because of a intraparticulate porous structure as revealed by AFM. The parameters derived from our piecewise equation approach can be used to guide particle synthesis in order to meet the local sustained release requirement, in vivo. The approach reported in our work, can be utilized with other encapsulated drugs or even in other polymeric systems, where researchers can use the extracted parameters to tune formulations and release kinetics.

6.1.3 Production of Flavopiridol Loaded Inhalable Ultra-small Particles for Pulmonary Delivery

This work demonstrates the successful production of inhalable ultra-small particles containing flavopiridol via spray drying technique. These produced particles represented the first time that flavopiridol has been incorporated into particles for pulmonary delivery. The presence of the particle components was verified using UV-Vis and ATR-FTIR spectroscopy. The particles produced were shown to be dispersible in flight, by a new method to determine dispersibility and morphology in the same readout. The in-vitro release profile was demonstrated to match the required release requirement for pulmonary delivery. These particles were demonstrated to be stable at all conditions tested, with no observed spectral changes. The incorporated flavopiridol in the formulation particles was demonstrated to be biologically active and ready for animal studies. This work enabled, the use of flavopiridol as a treatment option for inflammation-based diseases in the lung via pulmonary delivery of inhalable particles.

6.2 Future Perspectives

6.2.1 Further characterization of the flavopiridol loaded inhalable particles

The inhalable particles containing flavopiridol described in Chapter V, will undergo further testing for characterization of the in vitro aerodynamic properties from a dry powder inhaler and physical properties of the particles. This will be performed at a local company, iPharma ltd. (Union City, CA). First, the company will load 5 mg of inhalable particles into DPI capsules in an air-free environment. The capsule-based DPI device that will be used is “Plastiape” where the gravimetric and aerodynamic particle size distribution will be determined using a Next Generation Impactor. The moisture content of 20-50 mg of the produced particles will also be tested, using Karl Fischer titration methods. For each test, the analysis will be performed 3X to demonstrate reproducibility and deviation. If the particles perform exceptionally during these described tests, then this formulation will be utilized in the next steps for animal clinical trials for treatment of COVID-19.

6.2.2 In vitro and in vivo determination of the antiviral effects of flavopiridol on SARS-COV-2

The inhalable particles containing flavopiridol described in Chapter V will undergo in vitro and in vivo testing of the antiviral effects of flavopiridol on SARS-CoV-2 infection. It is expected that flavopiridol will reduce SARS-CoV-2 viral load in both in vitro and in vivo experiments. Materials will be transferred to Dr. Lark. L Coffey’s Biosafety Level 3 lab at the UC Davis School of Veterinary Medicine, where the in vitro and in vivo testing will occur.

6.2.3 Testing of the anti-inflammatory effects of flavopiridol in vivo

The inhalable particles containing flavopiridol described in Chapter V, will undergo in vivo testing of the anti-inflammatory effects using an animal model. It is expected that flavopiridol will reduce the inflammation response in the animal model. Material will be transferred to Dr. Dominik R. Haudenschild’s lab at UC Davis School of Medicine, where the in vivo testing will occur.

6.2.4 Testing of the anti-fibrotic effects of flavopiridol in vivo.

The inhalable particles containing flavopiridol described in Chapter V, will undergo in vivo testing of the anti-fibrotic effects of flavopiridol. It is expected that flavopiridol will present anti-fibrotic effects, in vivo. Materials will be transferred to Dr. Reen Wu’s lab at UC Davis School of Medicine, where the in vivo testing will occur.

CHAPTER VII

Appendix

7.1 SOP for the synthesis of 15 μm PLGA Microparticles from Chapter III

7.1.1 Purpose

This standard operating procedure outlines requirements to be considered by an authorized user of the flow focusing microfluidic device, used in the generation of 15 μm PLGA microparticles.

7.1.2 Personnel

A. Authorized Personnel: The Microfluidic Flow Focusing Device may be operated only by authorized personnel who are fully cognizant of all safety issues involved in the operation of this equipment. To become an authorized user, one must:

1. Read and fully understand "Sharps Safety Guidelines" (Safety Net #3) \
2. Receive training on using the Photron Ax-100 high speed camera by an authorized user
3. Receive training on Buchi R300 rotational evaporator by an authorized user
4. Receive training on Scanning Electron Microscopy (SEM) in Room 11
5. Receive training on Microfluidic Flow Focusing Device by an authorized user
6. Receive training on Chen Lab Lyophilizer
7. Read and fully understand all SOP's
8. Sign the authorized user sheet to affirm that the above steps have been completed.

B. Unauthorized personnel: All visitors during microfluidic synthesis must be briefed on proper safety protocol and must wear appropriate PPE located on the premises.

7.1.3 Hazards

A. Physical Hazards: Physical hazards may be present due to the handling of sharps for synthesis. For sharps safety guidelines read Safety Net #3

B. Chemical Hazards: chemical hazards are present in the microfluidic synthesis, through the use of the following chemicals

   i. Dichloromethane (DCM)
   ii. Polyvinyl alcohol (PVA)
   iii. Ethanol (200 proof) (EtOH)
   iv. Isopropyl alcohol (IPA)
   v. Acetone
   vi. Sodium dodecyl sulfate (SDS)
   vii. Liquid Nitrogen

C. Electrical Hazards: Electrical shock or electrocution could result from direct contact with electronics in the microfluidic flow focusing set-up

7.1.4 Hazards Control

A. Proper PPE Requirements for Microfluidic Synthesis

   1.) Laboratory Coat
   2.) Safety Glasses
   3.) Nitrile Gloves
   4.) Long Pants

5.) Close-toed Shoes

B. Physical Hazards: when inserting needle into PTFE tubing, care must be taken to avoid being stabbed by the sharp. Using tweezers to clasp onto the tubing and guide into the needle enough to form a seal.

C. Chemical Hazards: The use of dichloromethane outside of fume hood should not exceed > 1 mL. Solution preparation should be performed in the fume hood to avoid inhalation of toxic vapors.

D. Electrical Hazards: No components should be opened up and assume all internal components are hazardous.

7.1.5 Preliminary Protocol

A. Obtain a Flow-Focusing Microfluidic Device as shown below in Figure 7.1.

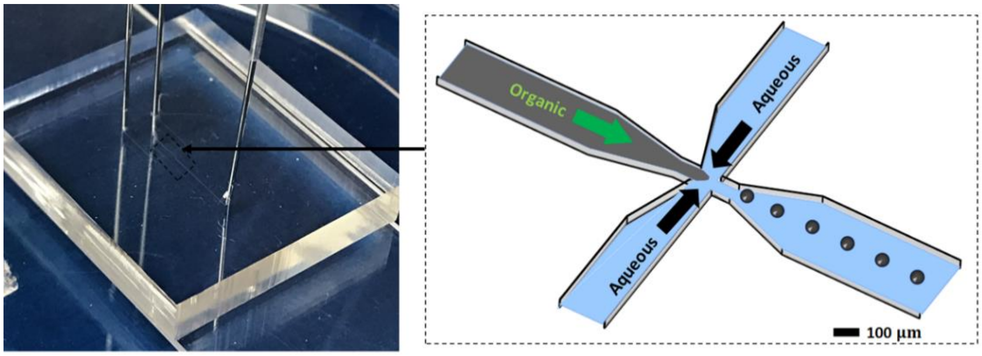

Figure 7.1. PDMS based Flow-Focusing Microfluidic Device with flow path schematic

B. Cleaning a used Flow-Focusing Microfluidic Device

a. Place the microfluidic device in a zip lock plastic bag containing solution with 1ml of 5% Sodium dodecyl sulfate (SDS) and 49ml DI H_2O and sonicate for 15min

b. Transfer the microfluidic chips to a zip lock plastic bag containing a solution with 25 ml acetone and sonicate for 15 min
c. Transfer the microfluidic chips to zip lock plastic bag containing 25ml (Isopropyl alcohol) IPA and sonicate for 15 min
d. Transfer the microfluidic chips to zip lock plastic bag containing 25ml 200 proof Ethanol sonicate for 15 min
e. Repeat step “a” to “d” twice
f. Wipe the outside surface of the microfluidic chips

C. Hydrophilic Coating of Microfluidic Channels using PVA treatment

Microfluidic Device channel’s must be hydrophilic to prevent organic solvent wetting to obtain droplet formation.

a. Plasma clean the microfluidic chips for 5min
b. Prepare 12 ml 1% polyvinyl alcohol (PVA) (98% hydrolyzed) (MW ~ 31 kDa) in a plastic syringe
c. Inject 1% PVA to middle channel, and let it sit for 10min to 15min
d. Dry the channels with N_2 gas and wipe the surface of the chip with Kim wipe
e. Put the microfluidic devices in oven (110°C) to dry for 15 to 20 mins
f. Repeat step “c” to “e” 3 times
g. Look at the microfluidic device channel through microscope to see if newly formed outer layer is visible.

D. Organic (10 mg/mL PLGA) phase preparation

10mg PLGA (polylactic-co-glycolic acid) (50:50) MW ~ 40 kDa was dissolved overnight in 1 mL dichloromethane in a sealed glass vial.

E. Aqueous (1% PVA) phase preparation
   1. Obtain 4 g of polyvinyl alcohol (PVA) (98% hydrolyzed) (MW ~ 31 kDa)
   2. Place 100 ml Milli-Q H_2O and a magnetic stir bar in 500 mL Erlenmeyer Flask
   3. Heat the water to 80 °C and mix at 500 rpm
   4. Slowly add the 4g PVA to the Erlenmeyer Flask until all solid is dispersed
   5. Allow the solution to sit overnight under heating and mixing
   6. Due to evaporation of water, add additional solvent till 100 mL original level is met
   7. Dilute the 4 % PVA solution with additional 300 ml Milli-Q H_2O to obtain a 1% PVA solution.

7.1.6 Microfluidic Flow Focusing Synthesis of 15 μm PLGA microparticles

1. The organic (PLGA) solution was transferred into a 1 mL Hamilton gas-tight syringe equipped with a 29-gauge Luer lock needle and equipped on a syringe pump (New Era Pump System, NE-300).
2. The aqueous 1% PVA solution was transferred into two 10 ml gas-tight syringes equipped with 29-gauge Luer lock needles and equipped on a separate dual-syringe pump (Princeton)
3. The two aqueous syringes were attached via PTFE tubing (30 gauge) and prefilled with aqueous solution.

4. Obtain a microfluidic flow focusing device on Chemistry Annex 0480
5. Place microfluidic flow focusing device onto an inverted microscope, equipped with a high-speed camera (Photron AX-100) as shown in Figure 7.2.

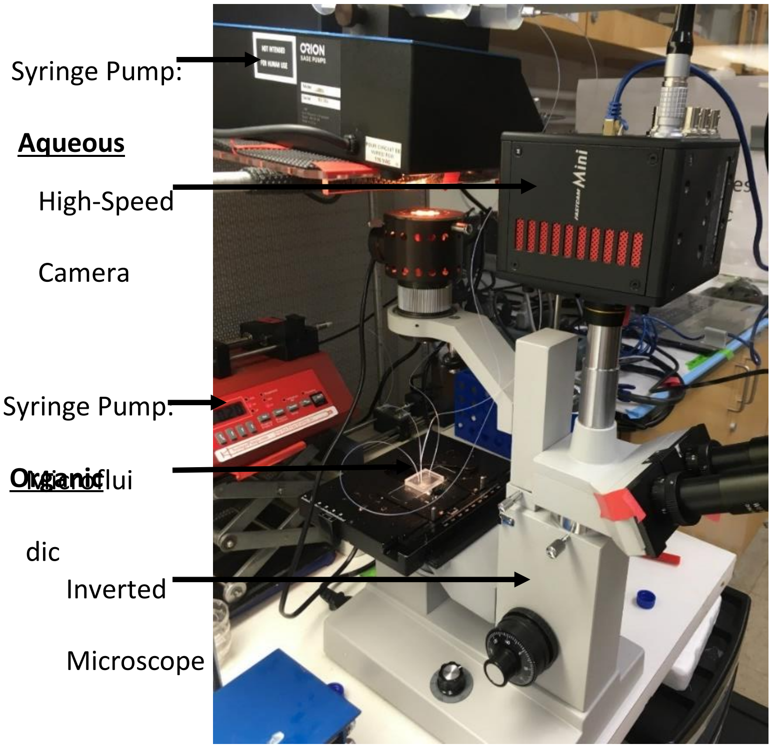

Figure 7.2. Home-built Flow Focusing Microfluidic Device for Uniform PLGA droplet formation

6. Turn on microscope light source to maximum and turn on high speed camera.
7. Insert tubing using tweezers into the two aqueous channel inlets as shown in Figure 7.3.
8. The organic syringe was similarly attached via PTFE tubing (30 gauge) and filled with organic solution.
9. Insert tubing into the organic channel inlet as shown in Figure 7.3.

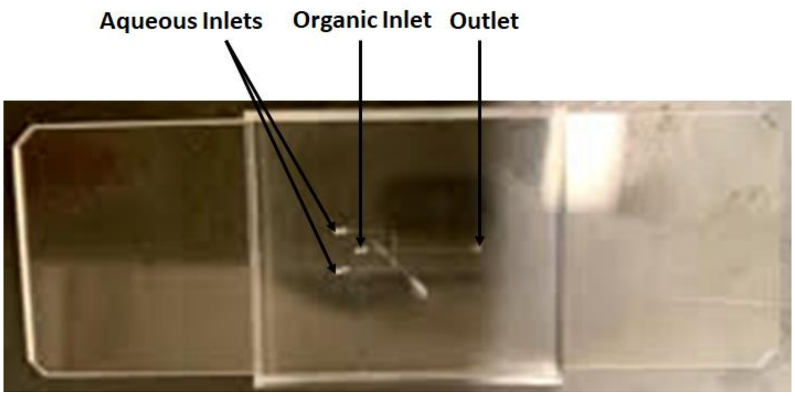

Figure 7.3. Inlet and outlet locations on PDMS-based Flow Focusing Microfluidic Device

10. PTFE tubing was inserted into the outlet of the microfluidic device and the open tubing was immersed in a round bottom flask (100 mL) containing 1 % w/v PVA (5 mL)
11. Set the organic phase flow rate to 0.2 ml/hr and the aqueous phase to 6 ml/hr
12. Using Photron's "PFV" software on the computer, configure settings to visualize orifice region. (See High-Speed Camera SOP for more information)
13. Press start on both syringe pumps
14. Droplet formation should be visible when the microchannels are filled with respective solution
15. If droplet formation is uniform with no visible solvent wetting, synthesis can continue as started
16. Droplet diameter can be measured using "PFV" software using width of channels as scale bar.
17. Uniform microdroplets should be visible in the range of 74 – 78 μm
18. If droplets are larger or smaller than range above, check for clogs near orifice region or leaks in device/syringes.

19. If droplet diameter range is attained, continue running experiment. (Be sure to not touch tubing during experiment, this will cause fluctuations in droplet size, causing polydispersity)

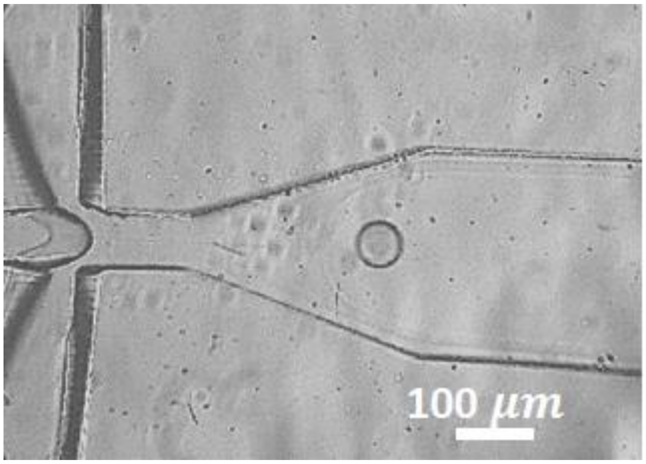

Figure 7.4. 76 μm PLGA droplet formation in Flow Focusing Microfluidic device, imaged in situ using high speed camera

20. Run experiment for at least 1.5 hours to obtain at least 3 mg of microparticles
21. After 1.5 hours, all tubing is removed from the microfluidic device and syringe pumps are turned off.
22. Turn off the high-speed camera and microscope
23. 1% PVA is flushed through microfluidic channels using plastic syringe to remove non-collected materials and is placed in a waste container and the device is stored for future use.
24. Used tubing is thrown away and syringe needles are placed in the sharp’s container.
25. Mount the collection flask on a rotational evaporator (Buchi R300) in room 25.

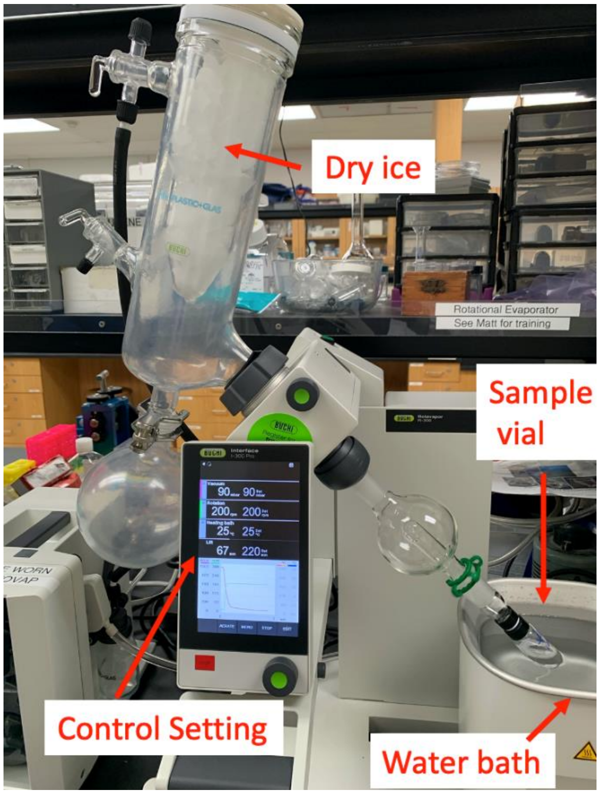

Figure 7.5. Mounting Sample Vial on the Buchi R300 for removal of dichloromethane from PLGA droplets

26. Dichloromethane is removed from the collection flask by setting Rotavapor settings to (Pressure = 90 mbar, rotation = 200 rpm, and heating bath = 25 °C). (Use Rotational Evaporator SOP for training)
27. Following evaporation, transfer the product to 15 mL conical tubes with equal volume
28. Place vials into a centrifuge at 1500 rpm for 5 mins
29. Carefully decant the supernatant into a waste container and add 10 mL of fresh Milli Q H_2O and quickly agitate microparticle pellet using a vortex.
30. Repeat “step 25 - 26” to two more times

31. Following washing, transfer particles in < 5 mL of water into a weighed glass scintillation vial and use a rubber band to cover the vial with a Kim wipe.
32. Quickly freeze the dispersed microparticles in liquid nitrogen and lyophilize to dryness using the Chen Lab Lyophilizer (Use Lyophilization SOP for training)
33. If particles are dry, weigh the vial to determine the microparticle yield and store the capped vial in -20 $°C$ freezer.

7.1.7 Determination of PLGA microparticle average diameter and dispersity using Scanning Electron Microscopy (SEM)

1. Obtain < 1 mg of synthesized PLGA microparticles and disperse in 30 μL of Milli Q water
2. Drop cast 5-10 μL of dispersed microparticles onto a 1 cm^2 Piranha cleaned silicon wafer
3. Allow sample to air dry in the Laminar Flow Hood in Room 25
4. Attach sample to an SEM stub using carbon tape
5. Place sample in the gold sputter (Ted Pella) in room 11 and sputter coat 10 nm of gold on the sample.
6. Place the sample in the SEM in room 11 and image the sample using V_{acc} = 2 kV (Get trained using SEM in Room 11)
7. Take images, where there are at least 100 particles.
8. Load the images on image J software and calculate the average diameter and dispersity using the coefficient of variation (CV) below.

$$CV = \left(\frac{\sigma}{d}\right) x\ 100 \tag{1}$$

9. Using the figure 6, shown below of the microparticle batch synthesized above, the CV was 2.9 % and the average diameter was 15.1 μm

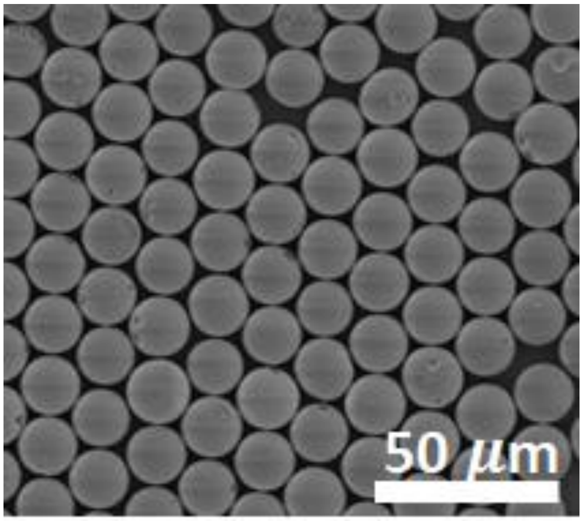

Figure 7.6. 15.1 μm PLGA microparticles synthesized using flow focusing microfluidics

7.2 Design of Microfluidic Flow Focusing Device in AutoCAD 2019

The Microfluidic flow focusing device was designed in AutoCAD 2019, and as shown below in Figure 7.7 is the 3D visual representation of the device. The zoom-in schematic as shown in Figure 7.8, with dimension drawn for the orifice region where droplets are generated.

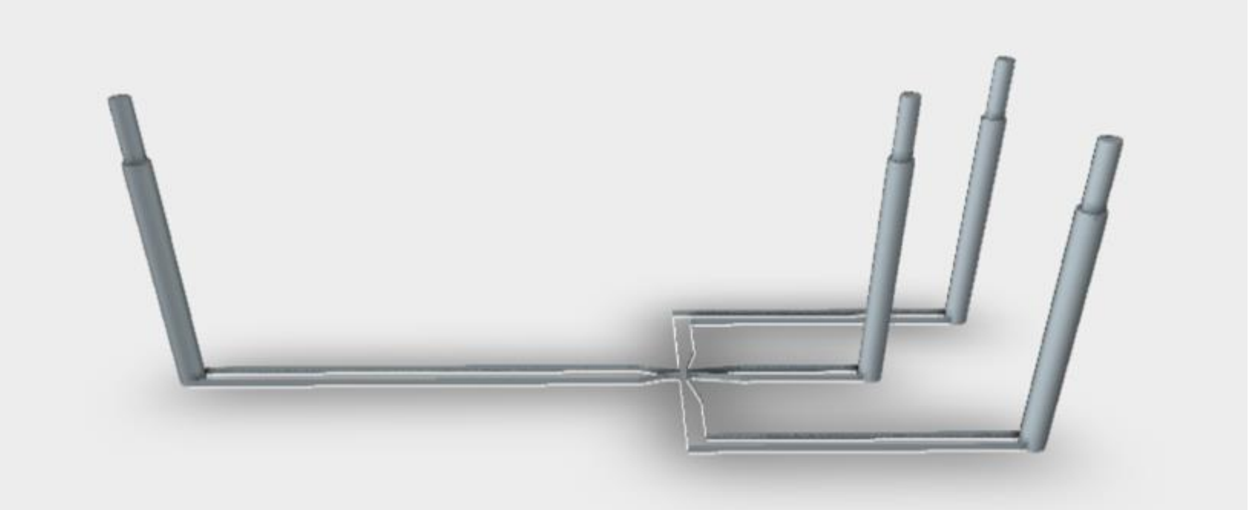

Figure 7.7. 3D visualization of AutoCAD created microfluidic flow focusing device used in Chapter III

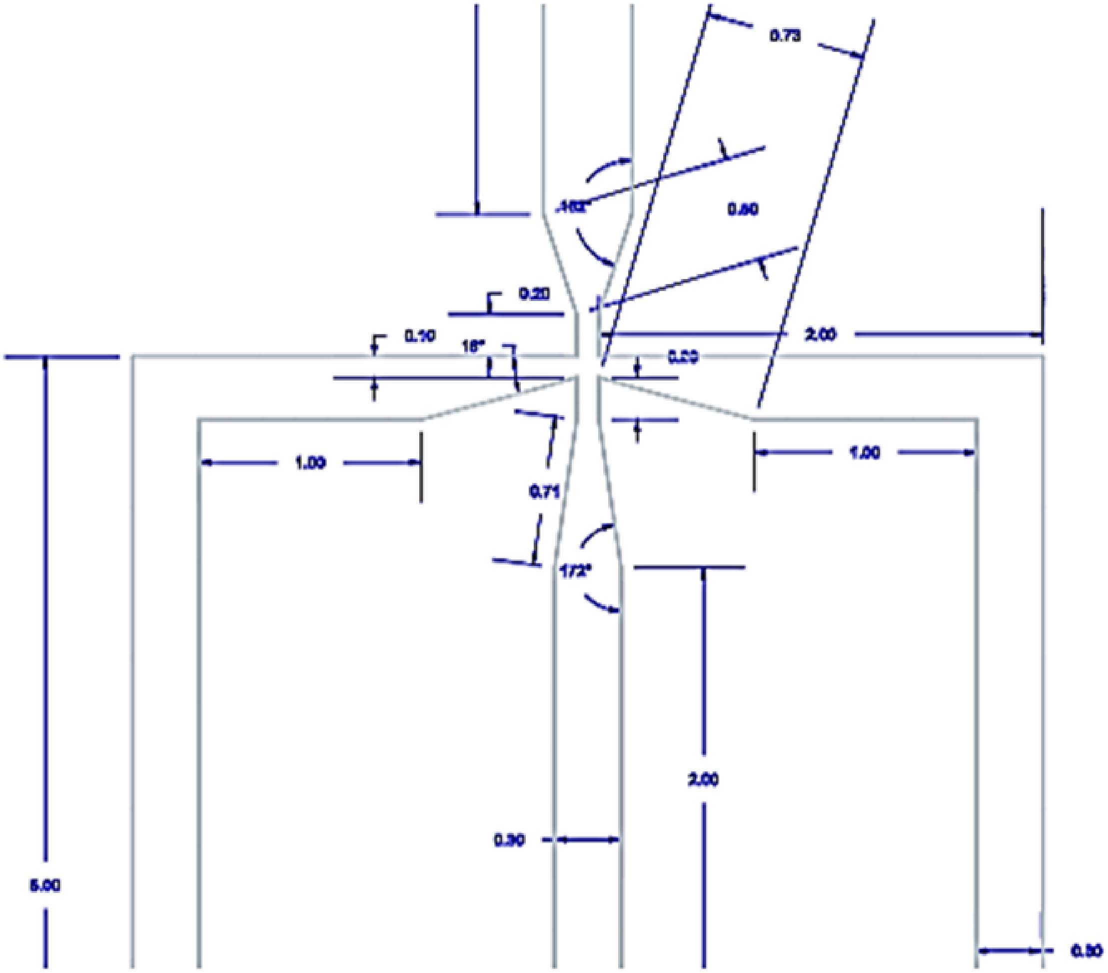

Figure 7.8. 2D schematic of the orifice region of the microfluidic flow focusing device

7.3 Non-linear least squares fitting of drug release profiles using MATLAB R2019

7.3.1 Two-term model involving burst and degradation release

The first code involved two-term burst and degradation model, and the general form is seen below:

```
%[xData, yData] = prepareCurveData( x, y );

% Set up fittype and options.
ft = fittype( '(a*((1-exp(-b*x))+((1-a)*exp(c*(x-d))/(1+exp(c*(x-d)))))*100', 'independent', 'x', 'dependent', 'y' );
opts = fitoptions( 'Method', 'NonlinearLeastSquares' );
opts.Display = 'Off';
opts.Lower = [0 0 0 0];
opts.StartPoint = [0 0 0 0];
opts.Upper = [1 Inf Inf];

% Fit model to data.
[fitresult, gof] = fit( x, y, ft, opts );

% Plot fit with data.
figure( 'Name', '15-DMC' );
h = plot( fitresult, x, y );
legend( h, 'y vs. x', '15-DMC', 'Location', 'NorthEast', 'Interpreter', 'none' );
% Label axes
xlabel( 'x', 'Interpreter', 'none' );
ylabel( 'y', 'Interpreter', 'none' );
grid on
```

7.3.2 Three-term model involving burst, degradation, and Fickian diffusion

The second code involved 3-term burst, degradation, and diffusion model, and the general form is seen below:

```
%radp = 0.00151;
disk = 0.0002;
%for i = 1:1:length(x)
    %Loop to evaluate each term in the series;
    %series(k) = Zeros(1, nTerms);
    %for k = 1:1:nterms
        %n = k-1;
       % series(k) = (1/n^2)*exp(-p(1)*n^2*pi^2*x(i)/R^2);
   %end
    %y(i) = 1-6/pi^2*sum(series);
```

```
for n = [1,10000000]
    fun = @(p,x32DMClate) (p(1)*(1-exp(-p(2)*x32DMClate))+p(3)*(exp(p(4)*(x32DMClate-p(5)))./(1+exp(p(4)*(x32DMClate-p(5)))))+(1-p(1)-p(3))*(1-(8./pi.^2)*sum((1./(2*n+1).^2)*exp(-pi.^2*(2*n+1).^2*p(6)*x32DMClate./2*disk.^2))))*100;

end
fun2 = @(p)fun(p,x32DMClate)-y32DMClate;
%make some initial guesses
x0 = [0.01,0.01,0.5,0.3,14,1E-7];
lb = [0,0,0,0,3,1E-18];
ub = [0.3,inf,0.7,inf,31,1E-6];
%options = optimoptions('lsqcurvefit','Algorithm','levenberg-marquardt');
%use lsqcurvefit machine learning algorithm to find optimal parameters for
%this data set
%p_opt = lsqcurvefit(fun, x0, x32DMClate, y32DMClate, lb, ub);

[xlsqnonlin,errorlsqnonlin] = lsqnonlin(fun2,x0,lb,ub);
x32DMClate, fun([xlsqnonlin,errorlsqnonlin], x32DMClate);
y32DMClate;
%print the optimized equation
%p_opt
%plot the data with the predicted relationship
figure;
scatter(x32DMClate,y32DMClate);
hold on;
plot(x32DMClate, fun([xlsqnonlin,errorlsqnonlin], x32DMClate), '-k');
hold off;
title("BRD Model");
legend("Experiment","Fitting");
xlabel("time(days)");
ylabel("% released");

SStot = sum((y32DMClate-mean(y32DMClate)).^2);
SSres = sum((y32DMClate(:)-fun([xlsqnonlin,errorlsqnonlin], x32DMClate)).^2);
Rsq = 1-SSres/SStot;
```

REFERENCES

(1) Jain, K. K. An Overview of Drug Delivery Systems. In *Drug Delivery Systems*; Jain, K. K., Ed.; Springer New York: New York, NY, 2020; pp 1-54.

(2) Tiwari, G.; Tiwari, R.; Sriwastawa, B.; Bhati, L.; Pandey, S.; Pandey, P.; Bannerjee, S. K. Drug delivery systems: An updated review. *Int J Pharm Investig* **2012,** *2* (1), 2-11, DOI: 10.4103/2230-973X.96920.

(3) Vargason, A. M.; Anselmo, A. C.; Mitragotri, S. The evolution of commercial drug delivery technologies. *Nature Biomedical Engineering* **2021,** *5* (9), 951-967, DOI: 10.1038/s41551-021-00698-w.

(4) Wen, H.; Jung, H.; Li, X. Drug Delivery Approaches in Addressing Clinical Pharmacology-Related Issues: Opportunities and Challenges. *AAPS J* **2015,** *17* (6), 1327-1340, DOI: 10.1208/s12248-015-9814-9.

(5) Diniz, M. A.; Tighiouart, M.; Rogatko, A. Comparison between continuous and discrete doses for model based designs in cancer dose finding. *PLOS ONE* **2019,** *14* (1), e0210139, DOI: 10.1371/journal.pone.0210139.

(6) Chen, R.; Wang, T.; Song, J.; Pu, D.; He, D.; Li, J.; Yang, J.; Li, K.; Zhong, C.; Zhang, J. Antiviral Drug Delivery System for Enhanced Bioactivity, Better Metabolism and Pharmacokinetic Characteristics. *Int J Nanomedicine* **2021,** *16*, 4959-4984, DOI: 10.2147/IJN.S315705.

(7) Sharma, S.; Sudhakara, P.; Singh, J.; Ilyas, R.; Asyraf, M.; Razman, M. Critical review of biodegradable and bioactive polymer composites for bone tissue engineering and drug delivery applications. *Polymers (Basel)* **2021,** *13* (16), 2623.

(8) Ali, A.; Ahmed, S. A review on chitosan and its nanocomposites in drug delivery. *International journal of biological macromolecules* **2018,** *109*, 273-286.

(9) Nance, E.; Pun, S. H.; Saigal, R.; Sellers, D. L. Drug delivery to the central nervous system. *Nature Reviews Materials* **2021**, DOI: 10.1038/s41578-021-00394-w.

(10) Preston, K. B.; Randolph, T. W. Stability of lyophilized and spray dried vaccine formulations. *Advanced Drug Delivery Reviews* **2021**.

(11) Sultana, S.; Alzahrani, N.; Alzahrani, R.; Alshamrani, W.; Aloufi, W.; Ali, A.; Najib, S.; Siddiqui, N. A. Stability issues and approaches to stabilised nanoparticles based drug delivery system. *Journal of drug targeting* **2020,** *28* (5), 468-486.

(12) Jana, P.; Shyam, M.; Singh, S.; Jayaprakash, V.; Dev, A. Biodegradable polymers in drug delivery and oral vaccination. *European Polymer Journal* **2021,** *142*, 110155.

(13) Senapati, S.; Mahanta, A. K.; Kumar, S.; Maiti, P. Controlled drug delivery vehicles for cancer treatment and their performance. *Signal Transduction and Targeted Therapy* **2018,** *3* (1), 7, DOI: 10.1038/s41392-017-0004-3.

(14) Alkilani, A. Z.; McCrudden, M. T. C.; Donnelly, R. F. Transdermal Drug Delivery: Innovative Pharmaceutical Developments Based on Disruption of the Barrier Properties of the stratum corneum. *Pharmaceutics* **2015,** *7* (4), 438-470, DOI: 10.3390/pharmaceutics7040438.

(15) Alqahtani, M. S.; Kazi, M.; Alsenaidy, M. A.; Ahmad, M. Z. Advances in Oral Drug Delivery. *Front Pharmacol* **2021,** *12* (62), DOI: 10.3389/fphar.2021.618411.

(16) Kang-Mieler, J. J.; Rudeen, K. M.; Liu, W.; Mieler, W. F. Advances in ocular drug delivery systems. *Eye* **2020,** *34* (8), 1371-1379, DOI: 10.1038/s41433-020-0809-0.

(17) Laffleur, F.; Bauer, B. Progress in nasal drug delivery systems. *Int J Pharm* **2021,** *607*, 120994.

(18) Gulati, N.; Gupta, H. Parenteral drug delivery: a review. *Recent patents on drug delivery & formulation* **2011,** *5* (2), 133-145.

(19) Yıldız-Peköz, A.; Ehrhardt, C., Advances in Pulmonary Drug Delivery. Multidisciplinary Digital Publishing Institute: 2020; Vol. 12, p 911.

(20) Thomas, A. C.; Hubbard-Turner, T.; Wikstrom, E. A.; Palmieri-Smith, R. M. Epidemiology of Posttraumatic Osteoarthritis. *J Athl Train* **2017,** *52* (6), 491-496, DOI: 10.4085/1062-6050-51.5.08.

(21) Khella, C. M.; Horvath, J. M.; Asgarian, R.; Rolauffs, B.; Hart, M. L. Anti-Inflammatory Therapeutic Approaches to Prevent or Delay Post-Traumatic Osteoarthritis (PTOA) of the Knee Joint with a Focus on Sustained Delivery Approaches. *Int J Mol Sci* **2021,** *22* (15), DOI: 10.3390/ijms22158005.

(22) Beigel, J. H.; Tomashek, K. M.; Dodd, L. E.; Mehta, A. K.; Zingman, B. S.; Kalil, A. C.; Hohmann, E.; Chu, H. Y.; Luetkemeyer, A.; Kline, S.; Lopez de Castilla, D.; Finberg, R. W.; Dierberg, K.; Tapson, V.; Hsieh, L.; Patterson, T. F.; Paredes, R.; Sweeney, D. A.; Short, W. R.; Touloumi, G.; Lye, D. C.; Ohmagari, N.; Oh, M.-d.; Ruiz-Palacios, G. M.; Benfield, T.; Fätkenheuer, G.; Kortepeter, M. G.; Atmar, R. L.; Creech, C. B.; Lundgren, J.; Babiker, A. G.; Pett, S.; Neaton, J. D.; Burgess, T. H.; Bonnett, T.; Green, M.; Makowski, M.; Osinusi, A.; Nayak, S.; Lane, H. C. Remdesivir for the Treatment of Covid-19 — Final Report. *New England Journal of Medicine* **2020,** *383* (19), 1813-1826, DOI: 10.1056/NEJMoa2007764.

(23) Pascarella, G.; Strumia, A.; Piliego, C.; Bruno, F.; Del Buono, R.; Costa, F.; Scarlata, S.; Agrò, F. E. COVID-19 diagnosis and management: a comprehensive review. *Journal of internal medicine* **2020,** *288* (2), 192-206.

(24) Skevaki, C.; Karsonova, A.; Karaulov, A.; Fomina, D.; Xie, M.; Chinthrajah, S.; Nadeau, K. C.; Renz, H. SARS-CoV-2 infection and COVID-19 in asthmatics: a complex relationship. *Nature Reviews Immunology* **2021,** *21* (4), 202-203, DOI: 10.1038/s41577-021-00516-z.

(25) Iwasaki, M.; Saito, J.; Zhao, H.; Sakamoto, A.; Hirota, K.; Ma, D. Inflammation Triggered by SARS-CoV-2 and ACE2 Augment Drives Multiple Organ Failure of Severe COVID-19: Molecular Mechanisms and Implications. *Inflammation* **2021,** *44* (1), 13-34, DOI: 10.1007/s10753-020-01337-3.

(26) Testa, G.; Giardina, S. M.; Culmone, A.; Vescio, A.; Turchetta, M.; Cannavò, S.; Pavone, V. Intra-Articular Injections in Knee Osteoarthritis: A Review of Literature. *Journal of Functional Morphology and Kinesiology* **2021,** *6* (1), DOI: 10.3390/jfmk6010015.

(27) Zhang, Y.; Yu, T.; Peng, L.; Sun, Q.; Wei, Y.; Han, B. Advancements in Hydrogel-Based Drug Sustained Release Systems for Bone Tissue Engineering. *Front Pharmacol* **2020,** *11* (622), DOI: 10.3389/fphar.2020.00622.

(28) Yavuz, B.; Chambre, L.; Kaplan, D. L. Extended release formulations using silk proteins for controlled delivery of therapeutics. *Expert Opin Drug Deliv* **2019,** *16* (7), 741-756, DOI: 10.1080/17425247.2019.1635116.

(29) Casalini, T.; Rossi, F.; Castrovinci, A.; Perale, G. A Perspective on Polylactic Acid-Based Polymers Use for Nanoparticles Synthesis and Applications. *Frontiers in Bioengineering and Biotechnology* **2019,** *7* (259), DOI: 10.3389/fbioe.2019.00259.

(30) Makadia, H. K.; Siegel, S. J. Poly Lactic-co-Glycolic Acid (PLGA) as Biodegradable Controlled Drug Delivery Carrier. *Polymers (Basel)* **2011,** *3* (3), 1377-1397, DOI: 10.3390/polym3031377.

(31) Blasi, P. Poly(lactic acid)/poly(lactic-co-glycolic acid)-based microparticles: an overview. *Journal of Pharmaceutical Investigation* **2019,** *49* (4), 337-346, DOI: 10.1007/s40005-019-00453-z.

(32) Kamali, H.; Khodaverdi, E.; Kaffash, E.; Saffari, A. S.; Shiadeh, S. N. R.; Nokhodchi, A.; Hadizadeh, F. Optimization and in Vitro Evaluation of Injectable Sustained-Release of Levothyroxine Using PLGA-PEG-PLGA. *Journal of Pharmaceutical Innovation* **2020**, DOI: 10.1007/s12247-020-09480-y.

(33) Zolnik, B. S.; Burgess, D. J. Evaluation of in vivo–in vitro release of dexamethasone from PLGA microspheres. *Journal of Controlled Release* **2008,** *127* (2), 137-145, DOI: https://doi.org/10.1016/j.jconrel.2008.01.004.

(34) Hung, L.-H.; Teh, S.-Y.; Jester, J.; Lee, A. P. PLGA micro/nanosphere synthesis by droplet microfluidic solvent evaporation and extraction approaches. *Lab on a Chip* **2010,** *10* (14), 1820-1825, DOI: 10.1039/C002866E.

(35) Panyam, J.; Labhasetwar, V. Biodegradable nanoparticles for drug and gene delivery to cells and tissue. *Advanced Drug Delivery Reviews* **2003,** *55* (3), 329-347, DOI: https://doi.org/10.1016/S0169-409X(02)00228-4.

(36) Kumari, A.; Yadav, S. K.; Yadav, S. C. Biodegradable polymeric nanoparticles based drug delivery systems. *Colloids and Surfaces B: Biointerfaces* **2010,** *75* (1), 1-18, DOI: https://doi.org/10.1016/j.colsurfb.2009.09.001.

(37) Liu, G.; Li, Y.; Yang, S.; Zhao, Y. a.; Lu, T.; Jia, W.; Ji, X.; Luo, Y. DOPA-IGF-1 Coated HA/PLGA Microspheres Promoting Proliferation and Osteoclastic Differentiation of Rabbit Bone Mesenchymal Stem Cells. *Chemical Research in Chinese Universities* **2019,** *35* (3), 514-520, DOI: 10.1007/s40242-019-9007-7.

(38) Cai, Q.; Qiao, C.; Ning, J.; Ding, X.; Wang, H.; Zhou, Y. A Polysaccharide-based Hydrogel and PLGA Microspheres for Sustained P24 Peptide Delivery: An In vitro and In vivo Study Based on Osteogenic Capability. *Chemical Research in Chinese Universities* **2019,** *35* (5), 908-915, DOI: 10.1007/s40242-019-9177-3.

(39) Kim, T.; See, C. W.; Li, X.; Zhu, D. Orthopedic implants and devices for bone fractures and defects: Past, present and perspective. *Engineered Regeneration* **2020,** *1*, 6-18, DOI: https://doi.org/10.1016/j.engreg.2020.05.003.

(40) Bolandparvaz, A.; Yik, J. H.; Lewis, J.; Haudenschild, D. R. Sustained intra-articular delivery of cyclin-dependent kinase 9 inhibitors protects against proteolytic activity in an ACL rupture rat model of PTOA. *Osteoarthritis and Cartilage* **2018,** *26*, S303-S304, DOI: 10.1016/j.joca.2018.02.610.

(41) Ren, H.; Han, M.; Zhou, J.; Zheng, Z.-F.; Lu, P.; Wang, J.-J.; Wang, J.-Q.; Mao, Q.-J.; Gao, J.-Q.; Ouyang, H. W. Repair of spinal cord injury by inhibition of astrocyte growth and inflammatory factor synthesis through local delivery of flavopiridol in PLGA nanoparticles. *Biomaterials* **2014,** *35* (24), 6585-6594, DOI: https://doi.org/10.1016/j.biomaterials.2014.04.042.

(42) Xu, Q.; Hashimoto, M.; Dang, T. T.; Hoare, T.; Kohane, D. S.; Whitesides, G. M.; Langer, R.; Anderson, D. G. Preparation of Monodisperse Biodegradable Polymer Microparticles Using a Microfluidic Flow-Focusing Device for Controlled Drug Delivery. *Small* **2009,** *5* (13), 1575-1581, DOI: 10.1002/smll.200801855.

(43) Vasiliauskas, R.; Liu, D.; Cito, S.; Zhang, H.; Shahbazi, M.-A.; Sikanen, T.; Mazutis, L.; Santos, H. A. Simple Microfluidic Approach to Fabricate Monodisperse Hollow Microparticles for Multidrug Delivery. *ACS Applied Materials & Interfaces* **2015,** *7* (27), 14822-14832, DOI: 10.1021/acsami.5b04824.

(44) Zhao, Y.; Shum, H. C.; Chen, H.; Adams, L. L. A.; Gu, Z.; Weitz, D. A. Microfluidic Generation of Multifunctional Quantum Dot Barcode Particles. *Journal of the American Chemical Society* **2011,** *133* (23), 8790-8793, DOI: 10.1021/ja200729w.

(45) Wang, H.; Liu, Y.; Chen, Z.; Sun, L.; Zhao, Y. Anisotropic structural color particles from colloidal phase separation. *Science Advances* **2020,** *6* (2), eaay1438, DOI: 10.1126/sciadv.aay1438.

(46) Chen, H.; Bian, F.; Sun, L.; Zhang, D.; Shang, L.; Zhao, Y. Hierarchically Molecular Imprinted Porous Particles for Biomimetic Kidney Cleaning. *Advanced Materials* **2020,** *32* (52), 2005394, DOI: https://doi.org/10.1002/adma.202005394.

(47) Zhang, H.; Chen, G.; Yu, Y.; Guo, J.; Tan, Q.; Zhao, Y. Microfluidic Printing of Slippery Textiles for Medical Drainage around Wounds. *Advanced Science* **2020,** *7* (16), 2000789, DOI: https://doi.org/10.1002/advs.202000789.

(48) Liu, D.; Zhang, H.; Fontana, F.; Hirvonen, J. T.; Santos, H. A. Microfluidic-assisted fabrication of carriers for controlled drug delivery. *Lab on a Chip* **2017,** *17* (11), 1856-1883, DOI: 10.1039/C7LC00242D.

(49) Xu, J.; Zhang, S.; Machado, A.; Lecommandoux, S.; Sandre, O.; Gu, F.; Colin, A. Controllable Microfluidic Production of Drug-Loaded PLGA Nanoparticles Using Partially Water-Miscible Mixed Solvent Microdroplets as a Precursor. *Scientific Reports* **2017,** *7* (1), 4794, DOI: 10.1038/s41598-017-05184-5.

(50) Kim, H.-G.; Kim, K.-M.; Kim, Y. H.; Lee, S. H.; Kim, G. M. Preparation of Monodisperse ENX-Loaded PLGA Microspheres Using a Microfluidic Flow-Focusing Device. *Journal of Biobased Materials and Bioenergy* **2013,** *7* (1), 108-114, DOI: 10.1166/jbmb.2013.1263.

(51) Schlosser, P. M.; Bale, A. S.; Gibbons, C. F.; Wilkins, A.; Cooper, G. S. Human health effects of dichloromethane: key findings and scientific issues. *Environ Health Perspect* **2015,** *123* (2), 114-119, DOI: 10.1289/ehp.1308030.

(52) Kim, H.; Kim, S.; Sah, H. Solvent hydrolysis rate determines critical quality attributes of PLGA microspheres prepared using non-volatile green solvent. *Journal of Biomaterials Science, Polymer Edition* **2018,** *29* (1), 35-56, DOI: 10.1080/09205063.2017.1398993.

(53) Agency, E. P., Methylene Chloride: Regulation of Paint and Coating Removal for Consumer Use Under TSCA Section 6(a). In *Part 751*, Agency, E. P., Ed. Federal Register: 2019; p 17.

(54) Viewpoint: Chemistry for a Sustainable Future. *Environmental Science & Technology* **2007,** *41* (14), 4840-4846, DOI: 10.1021/es0725798.

(55) Fredenberg, S.; Wahlgren, M.; Reslow, M.; Axelsson, A. The mechanisms of drug release in poly(lactic-co-glycolic acid)-based drug delivery systems—A review. *Int J Pharm* **2011,** *415* (1), 34-52, DOI: https://doi.org/10.1016/j.ijpharm.2011.05.049.

(56) Casalini, T.; Rossi, F.; Lazzari, S.; Perale, G.; Masi, M. Mathematical Modeling of PLGA Microparticles: From Polymer Degradation to Drug Release. *Molecular Pharmaceutics* **2014,** *11* (11), 4036-4048, DOI: 10.1021/mp500078u.

(57) Ford Versypt, A. N.; Pack, D. W.; Braatz, R. D. Mathematical modeling of drug delivery from autocatalytically degradable PLGA microspheres — A review. *Journal of Controlled Release* **2013,** *165* (1), 29-37, DOI: https://doi.org/10.1016/j.jconrel.2012.10.015.

(58) Gentile, P.; Chiono, V.; Carmagnola, I.; Hatton, P. V. An overview of poly(lactic-co-glycolic) acid (PLGA)-based biomaterials for bone tissue engineering. *Int J Mol Sci* **2014,** *15* (3), 3640-3659, DOI: 10.3390/ijms15033640.

(59) Han, F. Y.; Thurecht, K. J.; Whittaker, A. K.; Smith, M. T. Bioerodable PLGA-Based Microparticles for Producing Sustained-Release Drug Formulations and Strategies for Improving Drug Loading. *Front Pharmacol* **2016,** *7*, 185-185, DOI: 10.3389/fphar.2016.00185.

(60) Lucero-Acuña, A.; Guzmán, R. Nanoparticle encapsulation and controlled release of a hydrophobic kinase inhibitor: Three stage mathematical modeling and parametric analysis. *Int J Pharm* **2015,** *494* (1), 249-257, DOI: https://doi.org/10.1016/j.ijpharm.2015.07.049.

(61) Chen, W.; Palazzo, A.; Hennink, W. E.; Kok, R. J. Effect of Particle Size on Drug Loading and Release Kinetics of Gefitinib-Loaded PLGA Microspheres. *Molecular Pharmaceutics* **2017,** *14* (2), 459-467, DOI: 10.1021/acs.molpharmaceut.6b00896.

(62) Yoo, J.; Won, Y.-Y. Phenomenology of the Initial Burst Release of Drugs from PLGA Microparticles. *ACS Biomaterials Science & Engineering* **2020,** *6* (11), 6053-6062, DOI: 10.1021/acsbiomaterials.0c01228.

(63) Phelps, M. A.; Lin, T. S.; Johnson, A. J.; Hurh, E.; Rozewski, D. M.; Farley, K. L.; Wu, D.; Blum, K. A.; Fischer, B.; Mitchell, S. M.; Moran, M. E.; Brooker-McEldowney, M.; Heerema, N. A.; Jarjoura, D.; Schaaf, L. J.; Byrd, J. C.; Grever, M. R.; Dalton, J. T. Clinical response and pharmacokinetics from a phase 1 study of an active dosing schedule of flavopiridol in relapsed chronic lymphocytic leukemia. *Blood* **2009,** *113* (12), 2637-2645, DOI: 10.1182/blood-2008-07-168583.

(64) Yik, J. H. N.; Hu, Z. a.; Kumari, R.; Christiansen, B. A.; Haudenschild, D. R. Cyclin-dependent kinase 9 inhibition protects cartilage from the catabolic effects of proinflammatory cytokines. *Arthritis Rheumatol* **2014,** *66* (6), 1537-1546, DOI: 10.1002/art.38378.

(65) Hu, Z.; Yik, J. H. N.; Cissell, D. D.; Michelier, P. V.; Athanasiou, K. A.; Haudenschild, D. R. Inhibition of CDK9 prevents mechanical injury-induced inflammation, apoptosis and matrix degradation in cartilage explants. *Eur Cell Mater* **2016,** *30*, 200-209.

(66) Haudenschild, D. R.; Carlson, A. K.; Zignego, D. L.; Yik, J. H. N.; Hilmer, J. K.; June, R. K. Inhibition of Early Response Genes Prevents Changes in Global Joint Metabolomic Profiles in Mouse Post-Traumatic Osteoarthritis. *bioRxiv* **2018**, 379370, DOI: 10.1101/379370.

(67) Owen, M. J.; Yik, J. H. N.; Ye, C. W.; Netto, B.; Haudenschild, D. R.; Liu, G. Y. A Green Approach to Producing Polymer Microparticles for Local Sustained Release of Flavopiridol. *CHEMICAL RESEARCH IN CHINESE UNIVERSITIES* **2021,** *37* (5), 1116-1124, DOI: 10.1007/s40242-021-1262-8.

(68) Fukui, T.; Yik, J. H. N.; Doyran, B.; Davis, J.; Haudenschild, A. K.; Adamopoulos, I. E.; Han, L.; Haudenschild, D. R. Bromodomain-containing-protein-4 and cyclin-dependent-kinase-9 inhibitors interact synergistically in vitro and combined treatment reduces post-traumatic osteoarthritis severity in mice. *Osteoarthritis and Cartilage* **2021,** *29* (1), 68-77, DOI: https://doi.org/10.1016/j.joca.2020.07.012.

(69) Malumbres, M.; Pevarello, P.; Barbacid, M.; Bischoff, J. R. CDK inhibitors in cancer therapy: what is next? *Trends in Pharmacological Sciences* **2008,** *29* (1), 16-21, DOI: https://doi.org/10.1016/j.tips.2007.10.012.

(70) Byrd, J. C.; Lin, T. S.; Dalton, J. T.; Wu, D.; Phelps, M. A.; Fischer, B.; Moran, M.; Blum, K. A.; Rovin, B.; Brooker-McEldowney, M.; Broering, S.; Schaaf, L. J.; Johnson, A. J.; Lucas, D. M.; Heerema, N. A.; Lozanski, G.; Young, D. C.; Suarez, J.-R.; Colevas, A. D.; Grever, M. R. Flavopiridol administered using a pharmacologically derived schedule is associated with marked

clinical efficacy in refractory, genetically high-risk chronic lymphocytic leukemia. *Blood* **2006,** *109* (2), 399-404, DOI: 10.1182/blood-2006-05-020735.

(71) Chao, S.-H.; Fujinaga, K.; Marion, J. E.; Taube, R.; Sausville, E. A.; Senderowicz, A. M.; Peterlin, B. M.; Price, D. H. Flavopiridol Inhibits P-TEFb and Blocks HIV-1 Replication*. *Journal of Biological Chemistry* **2000,** *275* (37), 28345-28348, DOI: https://doi.org/10.1074/jbc.C000446200.

(72) Chao, S.-H.; Price, D. H. Flavopiridol Inactivates P-TEFb and Blocks Most RNA Polymerase II Transcription in Vivo. *Journal of Biological Chemistry* **2001,** *276* (34), 31793-31799.

(73) Perwitasari, O.; Yan, X.; O'Donnell, J.; Johnson, S.; Tripp, R. A. Repurposing Kinase Inhibitors as Antiviral Agents to Control Influenza A Virus Replication. *Assay Drug Dev Technol* **2015,** *13* (10), 638-649, DOI: 10.1089/adt.2015.0003.drrr.

(74) Shapiro, G. I.; Koestner, D. A.; Matranga, C. B.; Rollins, B. J. Flavopiridol Induces Cell Cycle Arrest and p53-independent Apoptosis in Non-Small Cell Lung Cancer Cell Lines. *Clinical Cancer Research* **1999,** *5* (10), 2925.

(75) Hon, K. L.; Leung, K. K. Y.; Leung, A. K.; Qian, S. Y.; Chan, V. P.; Ip, P.; Wong, I. C. Coronavirus disease 2019 (COVID-19): latest developments in potential treatments. *Drugs Context* **2020,** *9*, 2020-4-15, DOI: 10.7573/dic.2020-4-15.

(76) Gargouri, M.; Alzwi, A.; Abobaker, A. Cyclin dependent kinase inhibitors as a new potential therapeutic option in management of COVID-19. *Med Hypotheses* **2021,** *146*, 110380-110380, DOI: 10.1016/j.mehy.2020.110380.

(77) Zhang, C.; Zhang, Y. Q.; Qin, Y. H.; Zhang, Q. C.; Liu, Q.; Shang, D. Z.; Lu, H. J.; Li, X.; Zhou, C. Z.; Huang, F. M.; Jin, N. Y.; Jiang, C. Y. Ifenprodil and Flavopiridol Identified by Genomewide RNA Interference Screening as Effective Drugs To Ameliorate Murine Acute Lung

Injury after Influenza A H5N1 Virus Infection. *MSYSTEMS* **2019,** *4* (6), DOI: 10.1128/mSystems.00431-19.

(78) Levy, M. L.; Carroll, W.; Izquierdo Alonso, J. L.; Keller, C.; Lavorini, F.; Lehtimäki, L. Understanding Dry Powder Inhalers: Key Technical and Patient Preference Attributes. *Adv Ther* **2019,** *36* (10), 2547-2557, DOI: 10.1007/s12325-019-01066-6.

(79) Bosquillon, C.; Lombry, C.; Préat, V.; Vanbever, R. Influence of formulation excipients and physical characteristics of inhalation dry powders on their aerosolization performance. *Journal of Controlled Release* **2001,** *70* (3), 329-339, DOI: https://doi.org/10.1016/S0168-3659(00)00362-X.

(80) Minne, A.; Boireau, H.; Horta, M. J.; Vanbever, R. Optimization of the aerosolization properties of an inhalation dry powder based on selection of excipients. *European Journal of Pharmaceutics and Biopharmaceutics* **2008,** *70* (3), 839-844, DOI: https://doi.org/10.1016/j.ejpb.2008.06.013.

(81) Alhajj, N.; O'Reilly, N. J.; Cathcart, H. Designing enhanced spray dried particles for inhalation: A review of the impact of excipients and processing parameters on particle properties. *Powder Technology* **2021,** *384*, 313-331, DOI: https://doi.org/10.1016/j.powtec.2021.02.031.

(82) Eedara, B. B.; Alabsi, W.; Encinas-Basurto, D.; Polt, R.; Mansour, H. M. Spray-Dried Inhalable Powder Formulations of Therapeutic Proteins and Peptides. *AAPS PharmSciTech* **2021,** *22* (5), 185, DOI: 10.1208/s12249-021-02043-5.

(83) Chang, R. Y. K.; Chow, M. Y. T.; Khanal, D.; Chen, D. H.; Chan, H. K. Dry powder pharmaceutical biologics for inhalation therapy. *ADVANCED DRUG DELIVERY REVIEWS* **2021,** *172*, 64-79, DOI: 10.1016/j.addr.2021.02.017.

(84) Convery, N.; Gadegaard, N. 30 years of microfluidics. *Micro and Nano Engineering* **2019,** *2*, 76-91, DOI: https://doi.org/10.1016/j.mne.2019.01.003.

(85) Wyatt Shields Iv, C.; Reyes, C. D.; López, G. P. Microfluidic cell sorting: a review of the advances in the separation of cells from debulking to rare cell isolation. *Lab on a Chip* **2015,** *15* (5), 1230-1249, DOI: 10.1039/C4LC01246A.

(86) Kim, D.-Y.; Jin, S. H.; Jeong, S.-G.; Lee, B.; Kang, K.-K.; Lee, C.-S. Microfluidic preparation of monodisperse polymeric microspheres coated with silica nanoparticles. *Scientific Reports* **2018,** *8* (1), 8525, DOI: 10.1038/s41598-018-26829-z.

(87) Egorov, E.; Pieters, C.; Korach-Rechtman, H.; Shklover, J.; Schroeder, A. Robotics, microfluidics, nanotechnology and AI in the synthesis and evaluation of liposomes and polymeric drug delivery systems. *Drug Delivery and Translational Research* **2021,** *11* (2), 345-352, DOI: 10.1007/s13346-021-00929-2.

(88) Omidi, M.; Almeida, L.; Tayebi, L. Microfluidic-assisted fabrication of reverse micelle/PLGA hybrid microspheres for sustained vascular endothelial growth factor delivery. *Biotechnology and Applied Biochemistry* **2021,** *68* (3), 616-625, DOI: https://doi.org/10.1002/bab.1971.

(89) Han, F. Y.; Xu, W.; Kumar, V.; Cui, C. S.; Li, X.; Jiang, X.; Woodruff, T. M.; Whittaker, A. K.; Smith, M. T. Optimisation of a Microfluidic Method for the Delivery of a Small Peptide. *Pharmaceutics* **2021,** *13* (9), DOI: 10.3390/pharmaceutics13091505.

(90) McDonald, J. C.; Duffy, D. C.; Anderson, J. R.; Chiu, D. T.; Wu, H.; Schueller, O. J. A.; Whitesides, G. M. Fabrication of microfluidic systems in poly(dimethylsiloxane). *ELECTROPHORESIS* **2000,** *21* (1), 27-40, DOI: 10.1002/(SICI)1522-2683(20000101)21:1<27::AID-ELPS27>3.0.CO;2-C.

(91) Trantidou, T.; Elani, Y.; Parsons, E.; Ces, O. Hydrophilic surface modification of PDMS for droplet microfluidics using a simple, quick, and robust method via PVA deposition. *Microsyst Nanoeng* **2017,** *3*, 16091, DOI: Artn 16091

10.1038/Micronano.2016.91.

(92) Malamatari, M.; Charisi, A.; Malamataris, S.; Kachrimanis, K.; Nikolakakis, I. Spray Drying for the Preparation of Nanoparticle-Based Drug Formulations as Dry Powders for Inhalation. *PROCESSES* **2020,** *8* (7), DOI: 10.3390/pr8070788.

(93) Alhajj, N.; O'Reilly, N. J.; Cathcart, H. Leucine as an excipient in spray dried powder for inhalation. *DRUG DISCOVERY TODAY* **2021,** *26* (10), 2384-2396, DOI: 10.1016/j.drudis.2021.04.009.

(94) Eedara, B. B.; Alabsi, W.; Encinas-Basurto, D.; Polt, R.; Mansour, H. M. Spray-Dried Inhalable Powder Formulations of Therapeutic Proteins and Peptides. *AAPS PHARMSCITECH* **2021,** *22* (5), DOI: 10.1208/s12249-021-02043-5.

(95) Parumasivam, T.; Chang, R. Y. K.; Abdelghany, S.; Ye, T. T.; Britton, W. J.; Chan, H. K. Dry powder inhalable formulations for anti-tubercular therapy. *ADVANCED DRUG DELIVERY REVIEWS* **2016,** *102*, 83-101, DOI: 10.1016/j.addr.2016.05.011.

(96) Chow, A. H. L.; Tong, H. H. Y.; Chattopadhyay, P.; Shekunov, B. Y. Particle engineering for pulmonary drug delivery. *PHARMACEUTICAL RESEARCH* **2007,** *24* (3), 411-437, DOI: 10.1007/s11095-006-9174-3.

(97) Paudel, A.; Worku, Z. A.; Guns, J. M. S.; Guns, S.; Van den Mooter, G. Manufacturing of solid dispersions of poorly water soluble drugs by spray drying: Formulation and process considerations. *Int J Pharm* **2013,** *453* (1), 253-284, DOI: 10.1016/j.ijpharm.2012.07.015.

(98) Singh, A.; Van den Mooter, G. Spray drying formulation of amorphous solid dispersions. *ADVANCED DRUG DELIVERY REVIEWS* **2016,** *100*, 27-50, DOI: 10.1016/j.addr.2015.12.010.

(99) Wang, Z.; Ordoubadi, M.; Wang, H.; Vehring, R. Morphology and formation of crystalline leucine microparticles from a co-solvent system using multi-orifice monodisperse spray drying. *AEROSOL SCIENCE AND TECHNOLOGY* **2021,** *55* (8), 901-919, DOI: 10.1080/02786826.2021.1904129.

(100) Perkampus, H.-H. *UV-VIS Spectroscopy and its Applications*, Springer Science & Business Media: 2013.

(101) Bielan, Z.; Kowalska, E.; Dudziak, S.; Wang, K. L.; Ohtani, B.; Zielinska-Jurek, A. Mono- and bimetallic (Pt/Cu) titanium(IV) oxide core-shell photocatalysts with UV/Vis light activity and magnetic separability. *CATALYSIS TODAY* **2021,** *361*, 198-209, DOI: 10.1016/j.cattod.2020.05.034.

(102) Rammah, Y. S.; El-Agawany, F. I.; Mahmoud, K. A.; El-Mallawany, R.; Ilik, E.; Kilic, G. FTIR, UV-Vis-NIR spectroscopy, and gamma rays shielding competence of novel ZnO-doped vanadium borophosphate glasses. *JOURNAL OF MATERIALS SCIENCE-MATERIALS IN ELECTRONICS* **2020,** *31* (12), 9099-9113, DOI: 10.1007/s10854-020-03440-5.

(103) Zhang, C. X.; Liu, C.; Hu, Q. H.; Cai, Z. N.; Su, W. J.; Xia, C. Z.; Zhu, Y. Z.; Wang, S. W.; Liu, J. G. Satellite UV-Vis spectroscopy: implications for air quality trends and their driving forces in China during 2005-2017. *LIGHT-SCIENCE & APPLICATIONS* **2019,** *8*, DOI: 10.1038/s41377-019-0210-6.

(104) Zou, Q. L.; Lu, Y. C. Solvent-Dictated Lithium Sulfur Redox Reactions: An Operando UV-vis Spectroscopic Study. *JOURNAL OF PHYSICAL CHEMISTRY LETTERS* **2016,** *7* (8), 1518-1525, DOI: 10.1021/acs.jpclett.6b00228.

(105) L.C. Passos, M.; M.F.S. Saraiva, M. L. Detection in UV-visible spectrophotometry: Detectors, detection systems, and detection strategies. *Measurement* **2019,** *135*, 896-904, DOI: https://doi.org/10.1016/j.measurement.2018.12.045.

(106) Harris, D. C. *Quantitaive Chemical Analysis*, 5 ed.; W. H. Freeman and Company: New York, NY, 1999.

(107) Mester, L.; Govyadinov, A. A.; Chen, S.; Goikoetxea, M.; Hillenbrand, R. Subsurface chemical nanoidentification by nano-FTIR spectroscopy. *Nature Communications* **2020,** *11* (1), 3359, DOI: 10.1038/s41467-020-17034-6.

(108) Pluchery, O.; Costantini, J.-M. Infrared spectroscopy characterization of 3C–SiC epitaxial layers on silicon. *Journal of Physics D: Applied Physics* **2012,** *45* (49), 495101, DOI: 10.1088/0022-3727/45/49/495101.

(109) Erfan, M.; Sabry, Y. M.; Mortada, B.; Sharaf, K.; Khalil, D. In *Mid infrared MEMS FTIR spectrometer*, MOEMS and Miniaturized Systems XV, International Society for Optics and Photonics: 2016; p 97600K.

(110) Kazarian, S. G.; Chan, K. L. A. Applications of ATR-FTIR spectroscopic imaging to biomedical samples. *Biochimica et Biophysica Acta (BBA) - Biomembranes* **2006,** *1758* (7), 858-867, DOI: https://doi.org/10.1016/j.bbamem.2006.02.011.

(111) Vernon-Parry, K. Scanning electron microscopy: an introduction. *III-Vs Review* **2000,** *13* (4), 40-44.

(112) Goldstein, J. I.; Newbury, D. E.; Michael, J. R.; Ritchie, N. W.; Scott, J. H. J.; Joy, D. C. *Scanning electron microscopy and X-ray microanalysis*, Springer: 2017.

(113) Newbury*, D. E.; Ritchie, N. W. Is scanning electron microscopy/energy dispersive X-ray spectrometry (SEM/EDS) quantitative? *Scanning* **2013,** *35* (3), 141-168.

(114) Binnig, G.; Quate, C. F.; Gerber, C. Atomic force microscope. *Physical review letters* **1986,** *56* (9), 930.

(115) Rugar, D.; Hansma, P. Atomic force microscopy. *Physics today* **1990,** *43* (10), 23-30.

(116) Wadu-Mesthrige, K.; Amro, N. A.; Liu, G. Y. Immobilization of proteins on self-assembled monolayers. *Scanning* **2000,** *22* (6), 380-388.

(117) Wadu-Mesthrige, K.; Amro, N. A.; Garno, J. C.; Xu, S.; Liu, G.-y. Fabrication of nanometer-sized protein patterns using atomic force microscopy and selective immobilization. *Biophysical Journal* **2001,** *80* (4), 1891-1899.

(118) Lulevich, V.; Zink, T.; Chen, H.-Y.; Liu, F.-T.; Liu, G.-y. Cell mechanics using atomic force microscopy-based single-cell compression. *Langmuir* **2006,** *22* (19), 8151-8155.

(119) Tran, V.; Karsai, A.; Fong, M. C.; Cai, W.; Fraley, J. G.; Yik, J. H.; Klineberg, E.; Haudenschild, D. R.; Liu, G.-y. Direct Visualization of the Binding of Transforming Growth Factor Beta 1 with Cartilage Oligomeric Matrix Protein via High-Resolution Atomic Force Microscopy. *The Journal of Physical Chemistry B* **2020,** *124* (43), 9497-9504.

(120) Malachowski, T.; Hassel, A. Engineering nanoparticles to overcome immunological barriers for enhanced drug delivery. *Engineered Regeneration* **2020,** *1*, 35-50, DOI: https://doi.org/10.1016/j.engreg.2020.06.001.

(121) Yang, X.; Zhao, X.; Phelps, M. A.; Piao, L.; Rozewski, D. M.; Liu, Q.; Lee, L. J.; Marcucci, G.; Grever, M. R.; Byrd, J. C.; Dalton, J. T.; Lee, R. J. A novel liposomal formulation of flavopiridol. *Int J Pharm* **2009,** *365* (1-2), 170-174, DOI: 10.1016/j.ijpharm.2008.08.008.

(122) Bugai, A.; Quaresma, A. J. C.; Friedel, C. C.; Lenasi, T.; Düster, R.; Sibley, C. R.; Fujinaga, K.; Kukanja, P.; Hennig, T.; Blasius, M.; Geyer, M.; Ule, J.; Dölken, L.; Barborič, M. P-TEFb

Activation by RBM7 Shapes a Pro-survival Transcriptional Response to Genotoxic Stress. *Molecular Cell* **2019,** *74* (2), 254-267.e10, DOI: https://doi.org/10.1016/j.molcel.2019.01.033.

(123) Morales, F.; Giordano, A. Overview of CDK9 as a target in cancer research. *Cell Cycle* **2016,** *15* (4), 519-527, DOI: 10.1080/15384101.2016.1138186.

(124) Alder, C. M.; Hayler, J. D.; Henderson, R. K.; Redman, A. M.; Shukla, L.; Shuster, L. E.; Sneddon, H. F. Updating and further expanding GSK's solvent sustainability guide. *Green Chemistry* **2016,** *18* (13), 3879-3890, DOI: 10.1039/C6GC00611F.

(125) Tundo, P.; Selva, M. The Chemistry of Dimethyl Carbonate. *Accounts of Chemical Research* **2002,** *35* (9), 706-716, DOI: 10.1021/ar010076f.

(126) Hines, D. J.; Kaplan, D. L. Poly(lactic-co-glycolic) acid-controlled-release systems: experimental and modeling insights. *Crit Rev Ther Drug Carrier Syst* **2013,** *30* (3), 257-276, DOI: 10.1615/critrevtherdrugcarriersyst.2013006475.

(127) Sanabria-Ríos, D. J.; Rivera-Torres, Y.; Rosario, J.; Ríos, C.; Gutierrez, R.; Carballeira, N. M.; Vélez, C.; Zayas, B.; Álvarez-Colón, F.; Ortiz-Soto, G.; Serrano, V.; Altieri-Rivera, J.; Ríos-Olivares, E.; Rodríguez, J. W. Synthesis of novel C5-curcuminoid-fatty acid conjugates and mechanistic investigation of their anticancer activity. *Bioorganic & Medicinal Chemistry Letters* **2015,** *25* (10), 2174-2180, DOI: https://doi.org/10.1016/j.bmcl.2015.03.065.

(128) Albisa, A.; Piacentini, E.; Arruebo, M.; Sebastian, V.; Giorno, L. Sustainable Production of Drug-Loaded Particles by Membrane Emulsification. *ACS Sustainable Chemistry & Engineering* **2018,** *6* (5), 6663-6674, DOI: 10.1021/acssuschemeng.8b00401.

(129) Pinheiro, C. T.; Quina, M. J.; Gando-Ferreira, L. M. New Methodology of Solvent Selection for the Regeneration of Waste Lubricant Oil Using Greenness Criteria. *ACS Sustainable Chemistry & Engineering* **2018,** *6* (5), 6820-6828, DOI: 10.1021/acssuschemeng.8b00646.

(130) Zhai, S.; Senderowicz, A. M.; Sausville, E. A.; Figg, W. D. Flavopiridol, a Novel Cyclin-Dependent Kinase Inhibitor, in Clinical Development. *Annals of Pharmacotherapy* **2002,** *36* (5), 905-911, DOI: 10.1345/aph.1A162.

(131) FDA https://www.fda.gov/regulatory-information/search-fda-guidance-documents/supac-mr-modified-release-solid-oral-dosage-forms-scale-and-postapproval-changes-chemistry.

(132) Blewis, M. E.; Lao, B. J.; Jadin, K. D.; McCarty, W. J.; Bugbee, W. D.; Firestein, G. S.; Sah, R. L. Semi-permeable membrane retention of synovial fluid lubricants hyaluronan and proteoglycan 4 for a biomimetic bioreactor. *Biotechnol Bioeng* **2010,** *106* (1), 149-160, DOI: 10.1002/bit.22645.

(133) Sheikh, Z.; Brooks, P. J.; Barzilay, O.; Fine, N.; Glogauer, M. Macrophages, Foreign Body Giant Cells and Their Response to Implantable Biomaterials. *Materials (Basel)* **2015,** *8* (9), 5671-5701, DOI: 10.3390/ma8095269.

(134) Gustafson, H. H.; Holt-Casper, D.; Grainger, D. W.; Ghandehari, H. Nanoparticle Uptake: The Phagocyte Problem. *Nano Today* **2015,** *10* (4), 487-510, DOI: 10.1016/j.nantod.2015.06.006.

(135) Conaghan, P. G.; Cohen, S. B.; Berenbaum, F.; Lufkin, J.; Johnson, J. R.; Bodick, N. Brief Report: A Phase IIb Trial of a Novel Extended-Release Microsphere Formulation of Triamcinolone Acetonide for Intraarticular Injection in Knee Osteoarthritis. *Arthritis Rheumatol* **2018,** *70* (2), 204-211, DOI: 10.1002/art.40364.

(136) Kumar, A.; Bendele, A. M.; Blanks, R. C.; Bodick, N. Sustained efficacy of a single intra-articular dose of FX006 in a rat model of repeated localized knee arthritis. *Osteoarthritis and Cartilage* **2015,** *23* (1), 151-160, DOI: https://doi.org/10.1016/j.joca.2014.09.019.

(137) Evaluation, N. I. o. T. a., Biodegradation and bioaccumulation of the existing chemical substances under the Chemical Substances Control Law. National Institute of Technology and Evaluation: 2002.

(138) Makadia, H. K.; Siegel, S. J. Poly Lactic-co-Glycolic Acid (PLGA) as Biodegradable Controlled Drug Delivery Carrier. *Polymers* **2011,** *3* (3), DOI: 10.3390/polym3031377.

(139) Han, F. Y.; Thurecht, K. J.; Whittaker, A. K.; Smith, M. T. Bioerodable PLGA-Based Microparticles for Producing Sustained-Release Drug Formulations and Strategies for Improving Drug Loading. *Frontiers in Pharmacology* **2016,** *7* (185), DOI: 10.3389/fphar.2016.00185.

(140) Park, K.; Skidmore, S.; Hadar, J.; Garner, J.; Park, H.; Otte, A.; Soh, B. K.; Yoon, G.; Yu, D.; Yun, Y.; Lee, B. K.; Jiang, X.; Wang, Y. Injectable, long-acting PLGA formulations: Analyzing PLGA and understanding microparticle formation. *Journal of Controlled Release* **2019,** *304*, 125-134, DOI: https://doi.org/10.1016/j.jconrel.2019.05.003.

(141) Gaignaux, A.; Réeff, J.; Siepmann, F.; Siepmann, J.; De Vriese, C.; Goole, J.; Amighi, K. Development and evaluation of sustained-release clonidine-loaded PLGA microparticles. *Int J Pharm* **2012,** *437* (1), 20-28, DOI: https://doi.org/10.1016/j.ijpharm.2012.08.006.

(142) Qi, F.; Wu, J.; Li, H.; Ma, G. Recent research and development of PLGA/PLA microspheres/nanoparticles: A review in scientific and industrial aspects. *Frontiers of Chemical Science and Engineering* **2019,** *13* (1), 14-27, DOI: 10.1007/s11705-018-1729-4.

(143) Mitchell, M. J.; Billingsley, M. M.; Haley, R. M.; Wechsler, M. E.; Peppas, N. A.; Langer, R. Engineering precision nanoparticles for drug delivery. *Nature Reviews Drug Discovery* **2021,** *20* (2), 101-124, DOI: 10.1038/s41573-020-0090-8.

(144) Batycky, R. P.; Hanes, J.; Langer, R.; Edwards, D. A. A Theoretical Model of Erosion and Macromolecular Drug Release from Biodegrading Microspheres. *Journal of Pharmaceutical Sciences* **1997,** *86* (12), 1464-1477, DOI: https://doi.org/10.1021/js9604117.

(145) Tamani, F.; Hamoudi, M. C.; Danede, F.; Willart, J.-F.; Siepmann, F.; Siepmann, J. Towards a better understanding of the release mechanisms of caffeine from PLGA microparticles. *Journal of Applied Polymer Science* **2020,** *137* (25), 48710, DOI: https://doi.org/10.1002/app.48710.

(146) Lao, L. L.; Venkatraman, S. S.; Peppas, N. A. A novel model and experimental analysis of hydrophilic and hydrophobic agent release from biodegradable polymers. *Journal of Biomedical Materials Research Part A* **2009,** *90A* (4), 1054-1065, DOI: https://doi.org/10.1002/jbm.a.32171.

(147) Park, H.; Ha, D.-H.; Ha, E.-S.; Kim, J.-S.; Kim, M.-S.; Hwang, S.-J. Effect of Stabilizers on Encapsulation Efficiency and Release Behavior of Exenatide-Loaded PLGA Microsphere Prepared by the W/O/W Solvent Evaporation Method. *Pharmaceutics* **2019,** *11* (12), DOI: 10.3390/pharmaceutics11120627.

(148) Lucero-Acuña, A.; Gutiérrez-Valenzuela, C. A.; Esquivel, R.; Guzmán-Zamudio, R. Mathematical modeling and parametrical analysis of the temperature dependency of control drug release from biodegradable nanoparticles. *RSC Advances* **2019,** *9* (16), 8728-8739, DOI: 10.1039/C9RA00821G.

(149) Fitzgerald, J. F.; Corrigan, O. I. Mechanisms Governing Drug Release from Poly-α-Hydroxy Aliphatic Esters. In *Polymeric Delivery Systems*; American Chemical Society: 1993; Chapter 23, pp 311-326.

(150) Amini-Fazl, M. S.; Mobedi, H. Investigation of mathematical models based on diffusion control release for Paclitaxel from in-situ forming PLGA microspheres containing HSA

microparticles. *Materials Technology* **2020,** *35* (1), 50-59, DOI: 10.1080/10667857.2019.1651549.

(151) Crank, J. *The Mathematics of Diffusion*, Oxford University Press: London and New York, 1975.

(152) Hu, Z. a.; Chen, Y.; Song, L.; Yik, J. H. N.; Haudenschild, D. R.; Fan, S. Flavopiridol Protects Bone Tissue by Attenuating RANKL Induced Osteoclast Formation. *Front Pharmacol* **2018,** *9* (174), DOI: 10.3389/fphar.2018.00174.

(153) Haudenschild, D. R.; Carlson, A. K.; Zignego, D. L.; Yik, J. H. N.; Hilmer, J. K.; June, R. K. Inhibition of early response genes prevents changes in global joint metabolomic profiles in mouse post-traumatic osteoarthritis. *Osteoarthritis and Cartilage* **2019,** *27* (3), 504-512, DOI: https://doi.org/10.1016/j.joca.2018.11.006.

(154) Tan, A. R.; Swain, S. M. Review of flavopiridol, a cyclin-dependent kinase inhibitor, as breast cancer therapy. *Seminars in Oncology* **2002,** *29* (3, Supplement 11), 77-85, DOI: https://doi.org/10.1016/S0093-7754(02)70130-9.

(155) Stadler, W. M.; Vogelzang, N. J.; Amato, R.; Sosman, J.; Taber, D.; Liebowitz, D.; Vokes, E. E. Flavopiridol, A Novel Cyclin-Dependent Kinase Inhibitor, in Metastatic Renal Cancer: A University of Chicago Phase II Consortium Study. *Journal of Clinical Oncology* **2000,** *18* (2), 371-371, DOI: 10.1200/JCO.2000.18.2.371.

(156) Owen, M. J.; Yik, J. H. N.; Ye, C.; Netto, B.; Haudenschild, D. R.; Liu, G.-y. A Green Approach to Producing Polymer Microparticles for Local Sustained Release of Flavopiridol. *Chemical Research in Chinese Universities* **2021,** *37* (5), 1116-1124, DOI: 10.1007/s40242-021-1262-8.

(157) Trantidou, T.; Elani, Y.; Parsons, E.; Ces, O. Hydrophilic surface modification of PDMS for droplet microfluidics using a simple, quick, and robust method via PVA deposition. *Microsystems & Nanoengineering* **2017,** *3* (1), 16091, DOI: 10.1038/micronano.2016.91.

(158) Xu, Q.; Hashimoto, M.; Dang, T. T.; Hoare, T.; Kohane, D. S.; Whitesides, G. M.; Langer, R.; Anderson, D. G. Preparation of monodisperse biodegradable polymer microparticles using a microfluidic flow-focusing device for controlled drug delivery. *Small* **2009,** *5* (13), 1575-1581, DOI: 10.1002/smll.200801855.

(159) Spiess, A.-N.; Neumeyer, N. An evaluation of R2 as an inadequate measure for nonlinear models in pharmacological and biochemical research: a Monte Carlo approach. *BMC Pharmacology* **2010,** *10* (1), 6, DOI: 10.1186/1471-2210-10-6.

(160) Piñeiro, G.; Perelman, S.; Guerschman, J. P.; Paruelo, J. M. How to evaluate models: Observed vs. predicted or predicted vs. observed? *Ecological Modelling* **2008,** *216* (3), 316-322, DOI: https://doi.org/10.1016/j.ecolmodel.2008.05.006.

(161) Patrick Walters, W. WHAT ARE OUR MODELS REALLY TELLING US? A PRACTICAL TUTORIAL ON AVOIDING COMMON MISTAKES WHEN BUILDING PREDICTIVE MODELS. In *Chemoinformatics for Drug Discovery*; 2013; pp 1-31.

(162) Gu, B.; Sun, X.; Papadimitrakopoulos, F.; Burgess, D. J. Seeing is believing, PLGA microsphere degradation revealed in PLGA microsphere/PVA hydrogel composites. *J Control Release* **2016,** *228*, 170-178, DOI: 10.1016/j.jconrel.2016.03.011.

(163) Anamaria Teodora Coêlho Rios Silva, B. C. O. C., Maria Elisa Scarpelli,Ribeiro e Silva, Roberto Fernando Souza Freitas,; Sousa, R. G. Synthesis, Characterization, and Study of PLGA Copolymer in Vitro Degradation. *Journal of Biomaterials and Nanobiotechnology* **2015,** *6*, 8-19.

(164) van Apeldoorn, A. A.; van Manen, H.-J.; Bezemer, J. M.; de Bruijn, J. D.; van Blitterswijk, C. A.; Otto, C. Raman Imaging of PLGA Microsphere Degradation Inside Macrophages. *Journal of the American Chemical Society* **2004,** *126* (41), 13226-13227, DOI: 10.1021/ja0459936.

(165) Verano Naranjo, L.; Cejudo Bastante, C.; Casas Cardoso, L.; Mantell Serrano, C.; Martínez de la Ossa Fernández, E. J. Supercritical Impregnation of Ketoprofen into Polylactic Acid for Biomedical Application: Analysis and Modeling of the Release Kinetic. *Polymers* **2021,** *13* (12), 1982, DOI: 10.3390/polym13121982.

(166) Mylonaki, I.; Allémann, E.; Delie, F.; Jordan, O. Imaging the porous structure in the core of degrading PLGA microparticles: The effect of molecular weight. *Journal of Controlled Release* **2018,** *286*, 231-239, DOI: https://doi.org/10.1016/j.jconrel.2018.07.044.

(167) Klose, D.; Siepmann, F.; Elkharraz, K.; Krenzlin, S.; Siepmann, J. How porosity and size affect the drug release mechanisms from PLGA-based microparticles. *Int J Pharm* **2006,** *314* (2), 198-206, DOI: https://doi.org/10.1016/j.ijpharm.2005.07.031.

(168) Yu, M.; Yao, Q.; Zhang, Y.; Chen, H.; He, H.; Zhang, Y.; Yin, T.; Tang, X.; Xu, H. Core/shell PLGA microspheres with controllable in vivo release profile via rational core phase design. *Artificial Cells, Nanomedicine, and Biotechnology* **2018,** *46* (sup1), 1070-1079, DOI: 10.1080/21691401.2018.1443940.

(169) Shao, Q.; Feng, Y.; Wang, W.; Wang, M.; Li, B.; El Tahchi, M.; Yin, Y. Drug carrier for sustained release of withaferin A for pancreatic cancer treatment. *Journal of Materials Science* **2020,** *55* (4), 1702-1714, DOI: 10.1007/s10853-019-04139-7.

(170) Rapier, C. E.; Shea, K. J.; Lee, A. P. Investigating PLGA microparticle swelling behavior reveals an interplay of expansive intermolecular forces. *Scientific Reports* **2021,** *11* (1), 14512, DOI: 10.1038/s41598-021-93785-6.

(171) Yong, Y.; Lou, X.; Li, S.; Yang, C.; Yin, X. Direct simulation of the influence of the pore structure on the diffusion process in porous media. *Computers & Mathematics with Applications* **2014,** *67* (2), 412-423, DOI: https://doi.org/10.1016/j.camwa.2013.08.032.

(172) Eedara, B. B.; Rangnekar, B.; Doyle, C.; Cavallaro, A.; Das, S. C. The influence of surface active L-leucine and 1,2-dipalmitoyl-sn-glycero-3-phosphatidylcholine (DPPC) in the improvement of aerosolization of pyrazinamide and moxifloxacin co-spray dried powders. *Int J Pharm* **2018,** *542* (1-2), 72-81, DOI: 10.1016/j.ijpharm.2018.03.005.

(173) Daman, Z.; Gilani, K.; Rouholamini Najafabadi, A.; Eftekhari, H. R.; Barghi, M. A. Formulation of inhalable lipid-based salbutamol sulfate microparticles by spray drying technique. *Daru* **2014,** *22* (1), 50-50, DOI: 10.1186/2008-2231-22-50.

(174) Son, Y.-J.; McConville, J. T. Development of a standardized dissolution test method for inhaled pharmaceutical formulations. *Int J Pharm* **2009,** *382* (1), 15-22, DOI: https://doi.org/10.1016/j.ijpharm.2009.07.034.

(175) Raman, C.; Berkland, C.; Kim, K.; Pack, D. W. Modeling small-molecule release from PLG microspheres: effects of polymer degradation and nonuniform drug distribution. *Journal of Controlled Release* **2005,** *103* (1), 149-158, DOI: https://doi.org/10.1016/j.jconrel.2004.11.012.

(176) Huynh-Ba, K. *Handbook of stability testing in pharmaceutical development: regulations, methodologies, and best practices*, Springer: 2009.

(177) Bajaj, S.; Singla, D.; Sakhuja, N. Stability testing of pharmaceutical products. *Journal of applied pharmaceutical science* **2012,** *2* (3), 129-138.

(178) Hooton, J. C.; Jones, M. D.; Price, R. Predicting the behavior of novel sugar carriers for dry powder inhaler formulations via the use of a cohesive–adhesive force balance approach. *Journal of Pharmaceutical Sciences* **2006,** *95* (6), 1288-1297, DOI: https://doi.org/10.1002/jps.20618.

(179) Wauthoz, N.; Amighi, K. Phospholipids in pulmonary drug delivery. *European Journal of Lipid Science and Technology* **2014,** *116* (9), 1114-1128, DOI: https://doi.org/10.1002/ejlt.201300368.

(180) Li, J.; Wang, X.; Zhang, T.; Wang, C.; Huang, Z.; Luo, X.; Deng, Y. A review on phospholipids and their main applications in drug delivery systems. *Asian Journal of Pharmaceutical Sciences* **2015,** *10* (2), 81-98, DOI: https://doi.org/10.1016/j.ajps.2014.09.004.

(181) Weers, J.; Tarara, T. The PulmoSphere™ platform for pulmonary drug delivery. *Therapeutic Delivery* **2014,** *5* (3), 277-295, DOI: 10.4155/tde.14.3.

(182) Steckel, H.; Bolzen, N. Alternative sugars as potential carriers for dry powder inhalations. *International Journal of Pharmaceutics* **2004,** *270* (1), 297-306, DOI: https://doi.org/10.1016/j.ijpharm.2003.10.039.

(183) Kwon, Y.-B.; Kang, J.-H.; Han, C.-S.; Kim, D.-W.; Park, C.-W. The Effect of Particle Size and Surface Roughness of Spray-Dried Bosentan Microparticles on Aerodynamic Performance for Dry Powder Inhalation. *Pharmaceutics* **2020,** *12* (8), DOI: 10.3390/pharmaceutics12080765.

(184) Elversson, J.; Millqvist-Fureby, A. Particle Size and Density in Spray Drying—Effects of Carbohydrate Properties. *Journal of Pharmaceutical Sciences* **2005,** *94* (9), 2049-2060, DOI: https://doi.org/10.1002/jps.20418.

(185) Liang, W.; Pan, H. W.; Vllasaliu, D.; Lam, J. K. W. Pulmonary Delivery of Biological Drugs. *Pharmaceutics* **2020,** *12* (11), DOI: 10.3390/pharmaceutics12111025.

(186) Fröhlich, E.; Mercuri, A.; Wu, S.; Salar-Behzadi, S. Measurements of Deposition, Lung Surface Area and Lung Fluid for Simulation of Inhaled Compounds. *Frontiers in Pharmacology* **2016,** *7* (181), DOI: 10.3389/fphar.2016.00181.

(187) Berkenfeld, K.; Lamprecht, A.; McConville, J. T. Devices for dry powder drug delivery to the lung. *AAPS PharmSciTech* **2015,** *16* (3), 479-490, DOI: 10.1208/s12249-015-0317-x.

(188) Chrystyn, H. Methods to identify drug deposition in the lungs following inhalation. *Br J Clin Pharmacol* **2001,** *51* (4), 289-299, DOI: 10.1046/j.1365-2125.2001.01304.x.

(189) Mady, M. M.; Elshemey, W. M. Interaction of dipalmitoyl phosphatidylcholine (DPPC) liposomes and insulin. *Molecular Physics* **2011,** *109* (12), 1593-1598, DOI: 10.1080/00268976.2011.575408.

(190) Pleil, J. D.; Ariel Geer Wallace, M.; Davis, M. D.; Matty, C. M. The physics of human breathing: flow, timing, volume, and pressure parameters for normal, on-demand, and ventilator respiration. *Journal of Breath Research* **2021,** *15* (4), 042002, DOI: 10.1088/1752-7163/ac2589.

(191) Chaurasiya, B.; Zhao, Y.-Y. Dry Powder for Pulmonary Delivery: A Comprehensive Review. *Pharmaceutics* **2021,** *13* (1), DOI: 10.3390/pharmaceutics13010031.

(192) La Zara, D.; Sun, F.; Zhang, F.; Franek, F.; Balogh Sivars, K.; Horndahl, J.; Bates, S.; Brännström, M.; Ewing, P.; Quayle, M. J.; Petersson, G.; Folestad, S.; van Ommen, J. R. Controlled Pulmonary Delivery of Carrier-Free Budesonide Dry Powder by Atomic Layer Deposition. *ACS Nano* **2021,** *15* (4), 6684-6698, DOI: 10.1021/acsnano.0c10040.

(193) Mangal, S.; Nie, H.; Xu, R.; Guo, R.; Cavallaro, A.; Zemlyanov, D.; Zhou, Q. T. Physico-Chemical Properties, Aerosolization and Dissolution of Co-Spray Dried Azithromycin Particles with L-Leucine for Inhalation. *Pharm Res* **2018,** *35* (2), 28-28, DOI: 10.1007/s11095-017-2334-9.